Universitat Politècnica de Catalunya

Departament de Física Aplicada

Nocturnal Coastal fronts in the Mediterranean basin

Memòria presentada per

Jordi Mazón Bueso

per optar al grau de Doctor en Ciències.

Director:

David Pino González

Castelldefels, Febrer del 2015

Contents

Preface

Many times at early morning in the last 8 years, traveling near the coastline around the Llobregat Delta (15 km southwest of Barcelona city), I have usually observed offshore cloud bands approximately parallel to the coastline, while the rest of the sky remaines clear. These bands of clouds were around 15–30 km long, and located around 50 km offshore. These clouds are more commonly observed at early morning. Stratus and stratocumulus are the most common observed clouds associated to the bands. In some cases cumulus clouds produce weak showers.

Some examples of these cloud bands are shown in Fig. 1. Figure 1a shows a cloud band observed from the Fabra Observatory (425 masl) on 26 April 2014. Figure 1b shows a band of stratocumulus at the coast of the Llobregat Delta on 24 November 2010. Stratocumulus cloud band is shown in Fig. 1c observed from the Fabra Observatory on 10 March 2014. Sometimes, cumulus clouds have been also observed within these bands, specially offshore on the straight line of the Llobregat river mouth. This is the case shown in Fig. 1d, where cumulus clouds were located on the west side of the cloud band observed on 24 November 2010.

Figure 1: Several offshore cloud bands observed near the Llobregat Delta: (a) Stratus cloud band observed on 26 April 2014 near the Observatory Frabra at 0800 UTC, courtesy of Alfons Puertas (a); (b) Stratocumulus clouds associated to a cloud band observed on 24 November 2010 from the LLobregat Delta coastline; (c) Stratocumulus band observed from the Observatory Fabra on 10 March 2014, courtesy of Alfons Puertas; (d) Cumulus cloud band observed on 24 November 2010 offshore along the mouth of the Llobregat Delta.

After sunrise these cloud bands reduce both its depth and horizontal dimensions, and commonly disappear before midday.

Additionally, at early night, especially during late summer and autumn, showers occur over the Llobregat Delta. They are usually short in time and not associated with large unstability or synoptic fronts. These showers cover a relatively small area, sometimes affecting only the area of the Llobregat Delta.

Chapter 1

Introduction

1.1 Nocturnal coastal fronts

Precipitation occurring from the beginning of the night over the coastline until early morning offshore has been studied by several authors, mainly at the tropical regions (Kousky and Vemon, 1980; Frye and Chen, 2001; Ohsawa et al., 2003; Mapes et al., 2003a,b; Lau and Yi-Leng, 1999; Wu et al., 2008). These authors explain the occurrence of precipitation as follows. From late afternoon throughout the night, inland air cools faster than the air located at the coastline and over the sea. Consequently, this cooler and denser air begins to drain toward the coast by descending from mountain ranges, following rivers and dry streams, forming a density current [a] driven by drainage winds [b]. These density currents form a coastal front when interacting with the warmer sea–air (Schoenberg, 1984a; Neumann, 1951; Meyer, 1971).

Figure 1.1 shows a flow diagram of this process of formation, from drainage winds to coastal fronts and the associated cloud and rain bands that may appear.

---

[a] According to the glossary of the American Meteorology Society (AMS, Glickman (2000)) a density current is the intrusion of a denser fluid beneath a lighter due mainly to the hydrostatic forces arising from gravity and the density differences.

[b] Drainage wind is a generic term defined by the American Meteorology Society as cold-air-runoff winds that are produced when air in contact with terrain surfaces is cooled and flows downslope and/or downvalley (Glickman, 2000). This is the most generic term referring to the cold thermal winds, which includes the katabatic, downvalley, gravity winds and land breezes

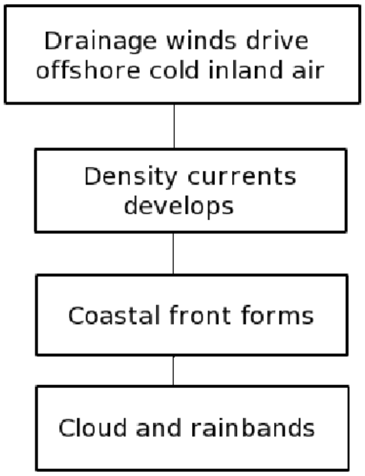

Figure 1.1: Schematic flow of the cloud and rain bands formation due to drainage winds.

1.1.1 Density current theory

The theory of density currents was developed by Benjamin (1968), based on previous studies (e.g. Kármán, 1940; Prandtl, 1952; Keulegan, 1958; Clarke, 1961). Benjamin (1968) found that the speed of a density current depends on the depth of the cold air mass and the potential temperature of the warm and cold air masses. According to this author, the density current velocity, C, reads:

$$C = V_w + k_B \sqrt{\frac{gH(\theta_w - \theta_c)}{\theta_w}} \ , \tag{1.1}$$

where g is the gravity acceleration, k_B is a dimensionless parameter close to 1 that depends on the depth of the warm air mass, H is the depth of the cold air mass, θ_w and θ_c are the potential temperature of the warm and cold air masses, respectively, and V_w is the speed of the warm air mass (positive when moving away from the cold air).

Laboratory experiments of density currents were developed in the late 1970's by John E. Simpson, confirming the theoretical predictions. In one of their most iconic papers (Simpson and Britter, 1980). They related laboratory experiments with coastal front formation. The depth of the cold air mass associated to a density current moving offshore, H, was estimated as:

$$H = \frac{\theta_{v,w}(U + 0.7V)^2}{gk_S^2(\theta_{v,w} - \theta_{v,c})} \ , \tag{1.2}$$

where $\theta_{v,w}$ and $\theta_{v,c}$ are, respectively, the 2–m virtual potential temperature of the warm and cold air masses, U and V are, respectively, the projections perpendicular to the front of the 2–m wind speed of the cold and warm air masses, and k_S is an internal Froude number, which is defined as the ratio of a characteristic velocity to a gravitational wave velocity. Simpson and Britter (1980) found $k_S = 0.62$ in laboratory experiments. Wakimoto and Atkins (1994), by studying land breezes in Florida, found $k_S = 1.07$.

It is important to remark that coastal fronts associated to density currents are a special type of front not associated with any cyclogenesis. Figure 1.2 shows an schematic representation of a density current which form a coastal front.

At the convergence zone between the two air masses, at the coastal front head, the ascending warm air condensates and forms stratiform clouds if the air reaches its Lifting Condensation Level (LCL). In some cases, convective clouds appear if the corresponding Level of Free Convection (LFC) is reached. In both cases the depth of the colder inland air mass (coastal–front depth, H) plays an important role in helping the wetter and warmer maritime air mass to reach LCL or LFC (Schoenberg, 1984b; Miglietta and Rotunno, 2010). No clouds will form if $H <$ LCL.

Once the coastal front is formed, the wind speed of the warm (V_w) and cold (V_c) air masses control the intensity and position of the possible precipitation. Several authors (Meyer, 1971; Schoenberg, 1984b; Heiblum et al., 2011) showed that the intensity of the prevailing wind, blowing towards the coast, and the land–sea temperature difference determine the position and rate of the precipitation. Specifically, V_c increases with the potential temperature difference between the cold and warm air masses. Consequently, if large land–sea temperature difference exists, the precipitation moves offshore, while large values of V_w moves it onshore (Mapes et al., 2003a). As it is expected, V_c is also influenced by roughness length over land (Malda et al., 2007).

1.1.2 Theoretical parameters applied to coastal fronts

Orography may contribute to heavy precipitation events in an unstable atmosphere (Lin et al., 2001; Reeves and Rotunno, 2008; Rotunno and Ferretti, 2001; Miglietta and Buzzi, 2001; Jiang et al., 2003; Davolio et al., 2006). To simplify the complexity existing in these events, by using 3D simulations Miglietta and Rotunno (2010) defined some parameters to explain the intensity and location of convective rainfall over an idealized mountain. They defined the trigger convection parameter h/LFC, where h is the mountain height. Values greater than 1 of this parameter suggest that convective cells appear over the mountain, while smaller values indicate that convection is inhibited. Another proposed parameter that measures the deceleration induced on the upstream flow by the stable layer existing aloft is $N\mathrm{LFC}/U$, where U is the horizontal wind speed of the flow blowing perpendicular to the mountain, and N is the the Brunt-Väisälä frequency:

$$N = \sqrt{\frac{d\theta}{dz}\frac{g}{\theta}}\ , \tag{1.3}$$

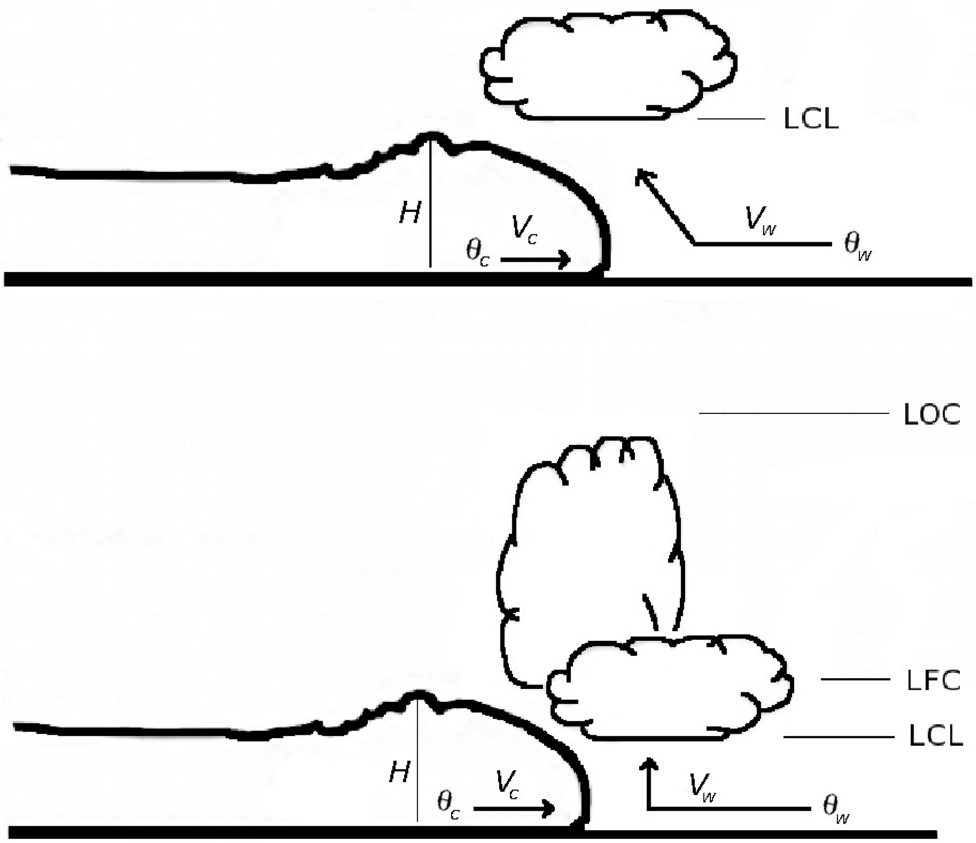

Figure 1.2: Scheme of a density current forming a front. See the text for the explanation of each variable. For simplification, we assume that the air masses are moving in parallel, opposite directions.

Moreover, Durran and Klemp (1987) defined the parameter Nh/U and found that the air flows easily over the mountain ridge with little blockage and minor vertical acceleration on the lee side of the ridge for $Nh/U \approx 0.25$. For $Nh/U \approx 5$, the flow is entirely blocked by the mountain and the air is forced upwards with large vertical accelerations. Finally, Wang et al. (2000) predicted, from modeling studies, that cloud bands form at the flow separation line between warm and cold air masses if $B = U/N >$ LFC.

As a first approach, it can be assumed that the cold air mass associated with a coastal front acts as a mountain range that lifts the prevailing warmer flow. Then, the triggering parameter h/LFC, proposed by Miglietta and Rotunno (2010), can be rewritten as H/LFC. It is important to note that while h and the LFC defined by Miglietta and Rotunno (2010) are related to a single air mass in our case H is the height of the cold air mass, and the LFC belongs to the warm, moist and unstable maritime air mass. In the same way, the blockage parameter defined in Durran and Klemp (1987) is redefined as NH/U, where U is the relative perpendicular wind speed of the two air masses.

1.2 Nocturnal offshore precipitation associated to coastal fronts around the world

Several researchers have investigated nocturnal precipitation associated to coastal fronts. This section aims to show the most iconic and relevant investigations concerning to this type of phenomenon.

The most studied area concerning to nocturnal precipitation are the tropical regions. Houze et al. (1981) used radar data to study the effect of the wind cycle and the associated rainfall in Borneo. The land breeze started at about midnight in this area, enhancing convection and rainfall offshore. By using radar reflectivity images, Yu and Jou (2004) detected and studied the formation of thunderstorms off the southeast coast of Taiwan, and the speed of the cold front drainage. Mori et al. (2004) described the formation of convective systems generated by offshore winds off the coast of Sumatra that, during the night, moved away from the coast at speeds of around 10 km h^{-1}.

Using automatic weather stations, several authors have studied nocturnal precipitation near the coastline. Camberlin and Planchon (1997) found that during the summer nights on the north coast of Kenya, due to differences in the strength of the land breeze, there was an increase of precipitation near the coast with respect to the southern areas. Kousky and Vemon (1980) detected nocturnal maximum rainfall between January and May at the mouth of the Amazon River, which was caused by the interaction of a cold air mass with warmer air located near the coast. Murakami (1983) described how, during the winter months between November and February, fronts caused by drainage winds on the southeast coast of Kunisaki Peninsula (Japan) produced an increase in rainfall when compared to other nearby areas. Lau and Yi-Leng (1999) used surface data and radio sounding to describe the nocturnal rainfall produced after midnight and until early morning in certain regions in Hawaii. They attributed it to the formation of a front.

Other authors have studied offshore convection using satellite images in addition to surface data. Frye and Chen (2001) examined the evolution of intense drainage winds (up to 11 m s^{-1}) that generated coastal fronts producing showers at night on the island of Hawaii on 7 and 8 of August 1990. The extension of these fronts is less than 10 km. Ohsawa et al. (2003) used precipitation data and images from the Japanese Geostationary Meteorological Satellite (GMS–5) over Bangladesh, Thailand, Vietnam and Malaysia to study coastal fronts. They found that areas with the highest rainfall at night and at early morning were located downwind of mountains, valleys and basins, and in coastal areas. According to these authors, this type of precipitation was probably associated with local winds and land and mountain breezes.

Mesoscale numerical models have been also used to study nocturnal precipitation near the coast. Mapes et al. (2003a,b) described and modeled the rain pattern in one of the rainiest areas of the planet: the coast along the western part of the Isthmus of Panama and the coast of Colombia. They used the fifth version of the Pennsylvania State University–NCAR Mesoscale Model (MM5, Grell et al. (1995); Dudhia (1993)) to show that between August and September the diurnal cycle of precipitation over land had a maximum during the afternoon, caused by convective systems. Moreover, there was a nocturnal maximum of precipitation over the valleys of the Andes and Lake Maracaibo, and on the Pacific coast during the night and early morning. This nocturnal maximum propagated offshore as the day progresses. Warner et al. (2003) modeled the observed precipitation on the coast of Colombia. During the afternoon, convection occurred inland, but when the land breeze started in late afternoon the rainfall moved offshore. However, these authors concluded that the land breeze was not enough to propagate the precipitation line, suggesting that gravity waves were the main cause for the propagation offshore during the night. Wu et al. (2008) studied nocturnal rainfall offshore in western Kalimantan Island, in Borneo by using surface meteorological observations, satellite observations of convection and precipitation, and MM5 numerical mesoscale model. They related large regularity in nocturnal precipitation, which occurred over the coastline at early night and move offshore as the night advances. They demonstrated that the interaction between land breeze with a prevailing warm sea–air was the cause of this precipitation. Wapler and Lane (2012) studied the nocturnal offshore convection near Darwin (Australia) using the WRF model. They found that the interaction between land breeze and synoptic flow was the cause of convection and precipitation in this area.

1.2.1 Nocturnal offshore precipitation associated to coastal fronts over the Mediterranean basin

Despite the above references dealing with nocturnal rainbands, there are only few studies focusing on nocturnal precipitation caused by coastal fronts on the Mediterranean basin. Probably the most iconic investigation about nocturnal coastal fronts in this basin was made by Neumann (1951). This author proposed the interaction between a prevailing synoptic wind and a land breeze to explain the observed offshore convection in south Israel. Goldreich et al. (2004) described local nocturnal precipitation from November to September in South Israel produced by coastal fronts near the coastline, formed by land breeze interacting with a synoptic flow. This precipitation represented a significant contribution to the total amount of rainfall in this area during the dry years. Also in this area, Heiblum et al. (2011) suggested that the concave shape of the coastline has an important role in enhancing the convergence of the land breeze and synoptic winds near the coastline.

In the western Mediterranean basin, Callado and Pascual (2002) detected nocturnal convection at the mouths of three rivers that flow into the northeastern coast of the Iberian Peninsula. These authors described qualitatively this type of precipitation and argued that it was formed by surface nocturnal convergence associated to coastal fronts.

Due to this lack of investigation about coastal fronts over the Mediterranean basin, this Thesis is focussed on this region, in order to improve the knowledge about nocturnal coastal fronts in the whole basin.

1.2.2 Meteorological scales of nocturnal coastal fronts

The nocturnal precipitation caused by the above explained mechanism, has been referenced at different spatial and temporal scales: from small rain cells to long rainbands, that last from few to several hours. Orlanski (1975) proposed a classification of meteorological scales based on three basic scales: micro, meso and macro, containing eight horizontal space and time subdivisions. The mesoscale is the intermediate scale between the macroscale (more than 1000 km and timescale of the order of several days) and the microscale (spatial scales of several meters and timescale on the order of a minute), in which the nocturnal coastal fronts are included.

Markowski and Richardson (2010) adapted the scales proposed by Orlanski (1975) and defined the ratio H/L as the relationship between the characteristic vertical (H) and horizontal (L) scales of the atmospheric phenomenon. If the characteristic horizontal scale of an event is much larger than the vertical scale ($H/L \ll 1$), it can be considered as an hydrostatic phenomenon; on the contrary, if the horizontal scale is smaller or similar than the vertical scale ($H/L \geq 1$), the event is non–hydrostatic.

These classifications are used in order to include the coastal fronts investigated on the Mediterranean basin within the correct meteorological scale.

1.3 An statistical analysis of the nocturnal precipitation on the Llobregat Delta

To remark the importance of the coastal fronts in the precipitation recorded in a coastal area, in this section the recorded precipitation during the last three decades in the Llobregat delta (LLD) is analyzed. Figure 1.3 shows the location of the LLD within the Mediterranean basin. This region is surrounded by the Mediterranean sea at the south and the east, the Barcelona city and Collserola mountain range by the northeast, and at the west and northwest by the Garraf mountain range.

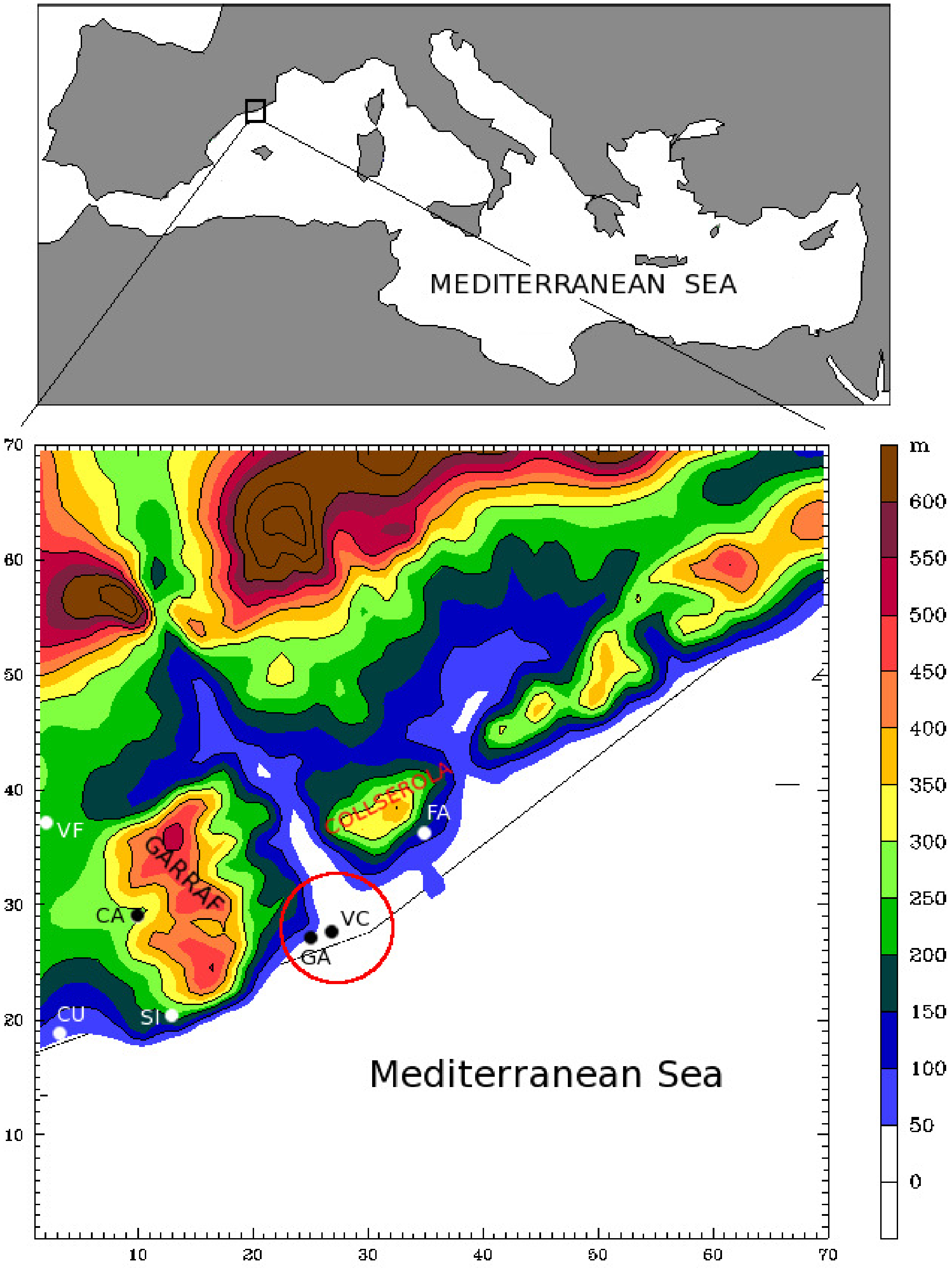

Figure 1.3: (Top) Geographical location of the Llobregat Delta on the Mediterranean Sea and (bottom) orography of the Llobregat Delta, where the position of the rain gauges used for the precipitation analysis on the Llobregat delta is indicated (dots). The red circle indicates the Llobregat delta region. The scale of the axis is in km.

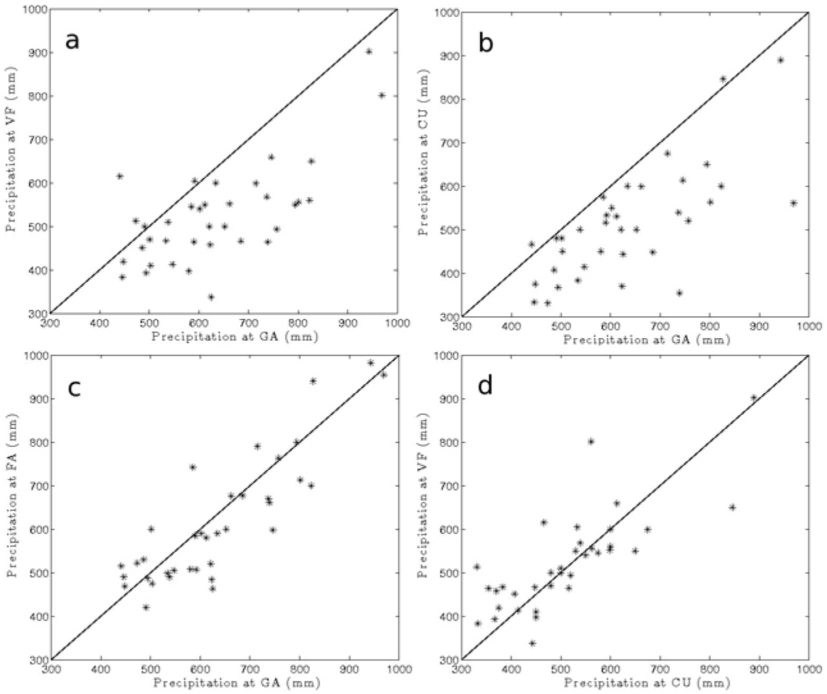

Figure 1.4: Cross comparison of the annual recorded precipitation during the period 1978–2013 between (a) Vilafranca (VF) and Gavà (GA), (b) Cubelles (CU) and Gavà (GA), (c) Fabra (FA) and Gavà (GA), and (d) Cubelles (CU) and Vilafranca (VF). All are stations of the Spanish Weather Agency.

In order to evaluate the importance of this nocturnal precipitation we use official rain–gauges of the Spanish Weather Agency (AEMET) and the Catalan Weather Service (METEOCAT). Two temporal series were analyzed: monthly rainfall from 1978 to 2013, and a second series, shorter but including more observations, from 1996 to 2013. The results of this last series have no climatic validity as defined by the Word Meteorological Organization, but it helps to endorse the tendency indicated by the first data series, with climatic validity. Figure 1.3 shows the location of the rain–gauges used in this analysis.

Figure 1.4 shows the comparison of the annual precipitation recorded at an station located at the LLD with the observations obtained at some surrounding stations during the period 1978-2013. A significant unequal spatial distribution of the precipitation pattern is observed at the LLD. While the average annual precipitation is 630 mm at GA (a representative station of the LLD), the rain gauges located outside the LLD recorded significant lower values: VI (25 km away from the LLD) 590 mm, SI (15 km south) 510 mm.

Moreover, the average number of rainy days (days with more than 0.1 mm of accumulated precipitation) during the considered period was 83 at GA, but 73, 51 and 70 days at VF, CU, and SI, respectively.

Focusing on the seasonal precipitation in the considered stations, the typical regime of coastal Mediterranean climate is observed. It exists a pluviometric maximum in autumn, a secondary one in spring, and two minimums during winter and summer. The precipitation during each season and the main atmospheric mechanisms that generate it are well known. Summer precipitation (from June to August) is almost homogeneous around the LLD. The main causes for the precipitation during this season are storms, and although the precipitation is normally well localized, over the years it affects the LLD and its surrounding areas in a similar way. Spring precipitation (from March to April) is caused, generally, by the passing of large–scale fronts associated with low pressures areas that moves eastwards. The more north and inland these systems are located, the more active they are. During this time of the year, it is in Vilafranca station, located in an inland area (indicated as VF in Fig. 1.3), where the precipitation presents a maximum with respect to the other rain gauges. Regarding the autumn season (from September to November), the precipitation is larger at the LLD than at the surrounding areas. Figure 1.5 shows the comparison between the total amount precipitation during autumn from 1978 to 2013 at GA (located at the LLD) and at some of the surrounding rain gauges: VF, CU, SI and FA (see Fig. 1.3). Significant differences can be observed in the spatial distribution of the precipitation. The total amount of precipitation recorded at the inland and southwest stations shows quite similar values, significantly lower than the recorded values in the station located at the LLD.

During winter (from December to February), slightly higher amounts of precipitation are observed at the LLD in relation to the observatories located in the surrounding areas.

Daily precipitation at another automatic meteorological station located in the LLD (VC in Fig. 1.3) is analyzed for all months, in order to study when the precipitation occurs during the day. No significant nocturnal precipitation is observed during spring, summer and winter months. However, focusing on autumn, a significant contribution of nocturnal precipitation is observed. Figure 1.6 shows the average monthly precipitation during the period 1993–2013 between the 22:00 and 07:00 LT (cyan bars) and during the whole day (blue bars). It must be noted that nocturnal precipitation during September represents nearly all the precipitation occurring in this month in every year studied. Regarding the variation within the day, between 22:00 and 07:00 LT, 58 mm out of 68 mm had fallen, representing 85% of the total precipitation during this month. During October 75%, and November around 77% of precipitation occurred from 22:00 until 07:00 LT. During the months of August, December and January, this percentage decreased considerably.

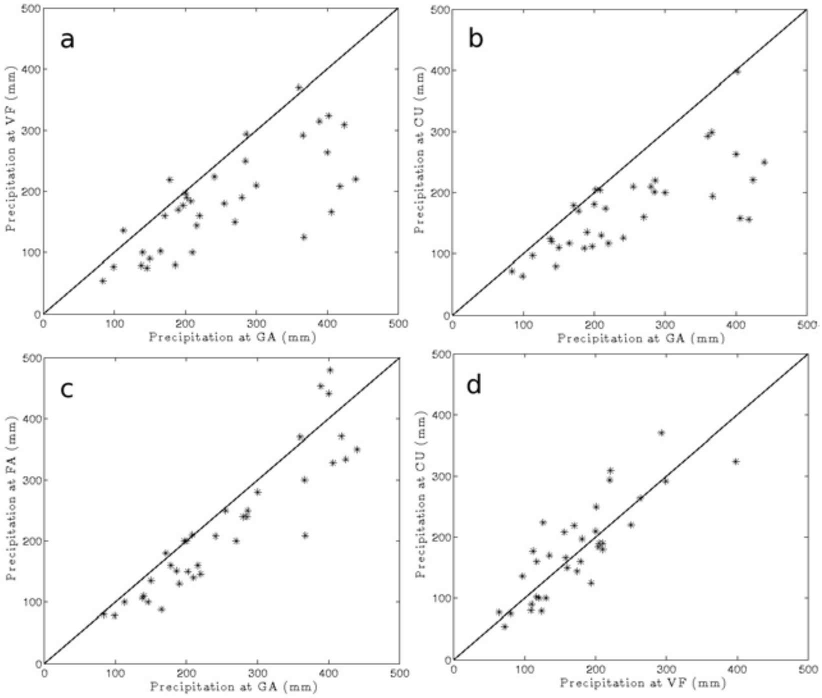

Figure 1.5: Cross comparison of the recorded precipitation during the autumn between (a) Vilafranca (VF) and Gavà (GA), (b) Cubelles (CU) and Gavà (GA), (c) Fabra (FA) and Gavà (GA), and (d) Cubelles (CU) and Vilafranca (VF) weather stations of the Spanish Weather Agency during the period 1978–2013.

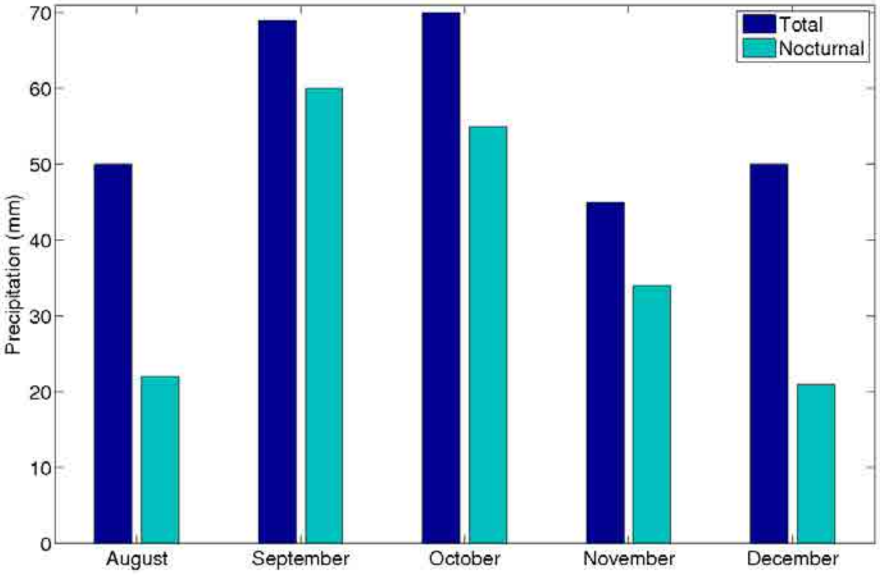

Figure 1.6: Average monthly precipitation (blue bars) and between 22:00 and 07:00 LT (cyan bars) from August until December in the period 1993–2013 recorded at Viladecans weather station of the Catalan Weather Service (VC in Fig. 1.3).

In summary, the higher amount of the annual precipitation recorded on the LLD with respect the surrounding areas can be attributed to an increase of the amount of precipitation during autumn; and within this season during nighttime.

Moreover, it is important to notice that on the basement of the Delta a large natural water reservoir exists; an important aquifer that has been of large importance in the development of a natural wet area (one of them is catalogued as Natural Space), as well as the economics of the region. This aquifer is formed by two different structures: the upper aquifer and the deeper one, separated by a sedimentary layer. Applying several hydrological models, the Consorci d'Usuaris d'Aigües del Delta del Llobregat (http://www.cuadll.org/) estimated that precipitation over the LLD is responsible 20% of the total amount of water that recharge this aquifer, mainly the upper one. The extraction of water from this upper aquifer contribute on the development of an irrigated agriculture over the Llobregat Delta, in contrast with the dry crops that dominate the surrounding areas. Furthermore, several important industries were located historically over the Delta because the availability for water for several industrial processes.

Considering the difference between the rainfall over the LLD and the southern stations, for instance SI and CU (see Fig. 1.3), with around less 100 mm in average respecte to the LLD), it can be estimated that over the LLD there is around 15% of the yearly precipitation caused by nocturnal precipitation during the autumn. Moreover, this precipitation falls over crops and infiltrate though the aquifer. Taking into account the extension of the Parc Agrari del Delta del Llobregat, with around 2938 Ha, it can be estimated that around $3{\cdot}10^8$ l is the amount of excess of precipitated water over the LLD respect to the surrounding areas due to the nocturnal precipitation.

1.4 Methodology

Different tools can be used to investigate precipitation: rain gauges, reflectivity radar and satellite images, numerical models. However, focussing on the events that this Thesis aims to investigate, two difficulties exist. The analyzed precipitation mainly occurs over the sea where there are not rain gauges. Additionally, this nocturnal precipitation can be weak, affecting a relatively small area.

Reflectivity radar and satellite images have been the main tools to detect and analyze the nocturnal offshore precipitation near the coastline in tropical regions, where large rainbands are enough long to be detected by satellite images. Focussing on the Mediterranean basin, the nocturnal precipitation is normally weaker and affecting a smaller area than at the tropical region, having less horizontal extension than those recorded in tropical regions, being more difficult they detection. However, some bands are enough long to be recorded by some satellites. Moreover, radar network ranges no more than a few hundred kilometers and many areas on the Mediterranean basin are not totally covered by radar measurements.

For these reasons, in order to study the whole Mediterranean basin, we have developed a methodology based on three stages. The first one consists in detecting the nocturnal offshore precipitation events by using the Tropical Rainfall Measurement Mission (TRMM) radar satellite database from 18:00 to 09:00 UTC (Haddad et al., 1997; Huffman et al., 2007b). Second stage uses the NCEP reanalysis database for reconstructing the main synoptic conditions related to an event. In the final stage, by using the version 3.3 of the Weather Research Forecast – Advanced Weather Research (WRF–ARW) model (Skamarock et al., 2008) we simulate, analyze and characterize some of the selected events in the two previous stages. Figure 1.7 shows a flow diagram summarizing this methodology. Next sections describe the three stages developed in this methodology.

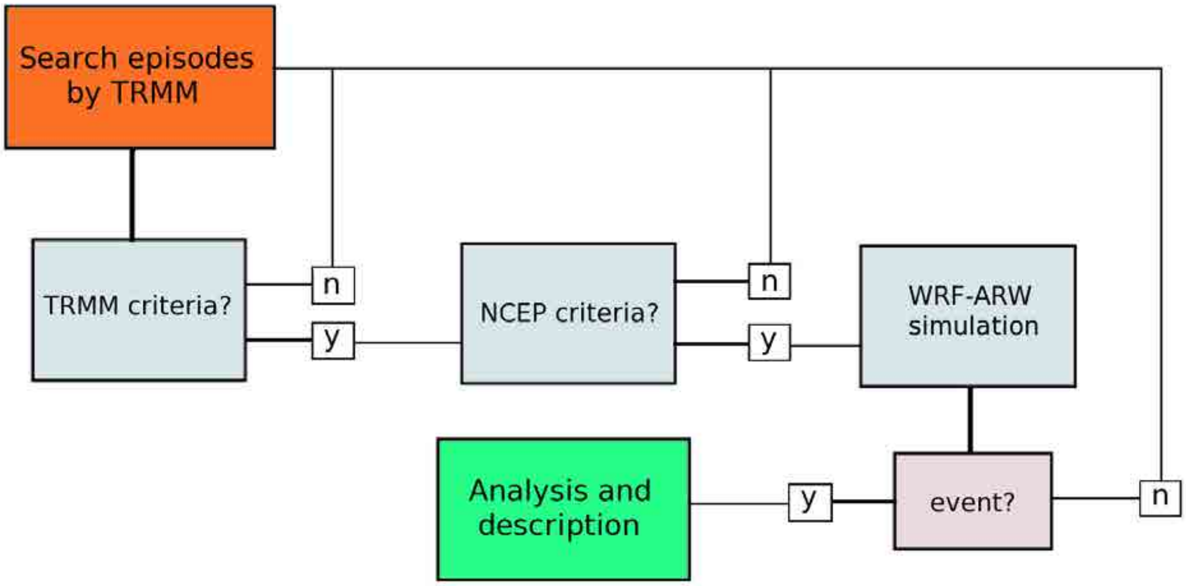

Figure 1.7: Flow scheme of the stages defined in the methodology.

1.4.1 TRMM satellite

Tropical Rainfall Measuring Mission (TRMM) is a NASA and JAXA satellite launched in 1997 designed to measure tropical rainfall for weather and climate research (Haddad et al., 1997; Huffman et al., 2007b). The satellite images cover tropical and sub-tropical regions of the Earth. This satellite is equipped with remote and passive sensing instruments, including a 13.8 GHz precipitation radar that obtains rainfall distribution over both land and oceans, and also define the layer depth of the precipitation. In addition to this radar sensing, several other instruments are carried on TRMM, such as a lightning imaging sensor, cloud and Earth Radiant Energy sensor, a Visible Infrared Radiometer, and a multichannel passive microwave radiometer that provides several information related to the precipitation, such us the rain intensity, the integrated column precipitation content, or the cloud liquid water, among some others.

The horizontal resolution at the ground is 4.7 km and the portion of Earth's surface measured during a single overpass is about 220 km^2. It is able to detect fairly light rainfall rates larger than to 0.7 mm h^{-1}, enough to detect events of weak precipitation. However, according to Sarrand et al. (2012) TRMM underestimates light rain at latitudes higher than 37°.

Version 6 of the 3B42 product provides 3-hour accumulated precipitation from an on-board radar instrument (Huffman et al., 2007a), at latitudes between $-50°$ and $50°$, and longitudes from $-180°$ to $180°$, with a spatial resolution of 0.25×0.25 km^2. This 3-hourly accumulated rainfall measured by TRMM satellite has been visualized by using the TOVAS tool (TRMM Online Visualization and Analysis System), a member of the Giovanni family (Acker and Leptoukh, 2007).

TRMM data has been analyzed from 18:00 UTC to 09:00 UTC every day, to detect possible events of nocturnal precipitation in the Mediterranean basin. To accept that the cause of the events detected by using TRMM might be due to the interaction between nocturnal drainage winds or land-breeze with a synoptic flow, the following conditions have to be fulfilled:

- The nocturnal precipitation appears near the coastline.
- The precipitation area is quasi-stationary offshore near the coastline, or it slightly moves.
- The precipitation lasts no more than 6 hours, and disappears few hours after sunrise.
- The precipitation extends no more than 500 km, and it might be grouped in clusters of several individual cells.

1.4.2 NCEP Reanalysis data

In order to analyze the synoptic atmospheric conditions, the NOAA-CR20 and NCEP reanalysis database (available on http://www.esrl.noaa.gov/psd/data/gridded/data.ncep.reanalysis.html) has been used to analyze the atmospheric conditions at 1000 hPa, 850 hPa and 500 hPa. By analyzing this data, we have been able to discard those episodes of nocturnal precipitation where the main cause is related to synoptic features such as convection associated to a dynamic low–pressure area, to some large–scale warm or cold front, or to a trough affecting the region under study.

1.4.3 WRF–ARW model

The WRF–ARW mesoscale model (Skamarock et al., 2008) is one of the most frequently used mesoscale models in atmospheric research. Many investigations related to thermal winds and precipitation are based on the WRF simulations. Wapler and Lane (2012) investigated nocturnal fronts at Darwing (Australia) by using WRF–ARW simulations; sea–breeze regimens have been studied by using WRF model by several authors (LaCasse et al., 2008;

Pérez et al., 2004; Hernández-Ceballos et al., 2013); low–level winds by Michelson and Bao (2008), Storm et al. (2008); precipitation episodes at local and regional scales by Hong and Lee (2009), Bukovsky and Karoly (2009), Segele et al. (2008). Over the Mediterranean basin cyclones and heavy precipitation have been simulated by Moscatello et al. (2008), Miglietta et al. (2013).

General description

WRF–ARW is a compressible non-hydrostatic finite difference model that includes the equations governing the atmosphere: conservation of mass, conservation of momentum, conservation of energy, conservation of water and gases. This model runs on three stages.

The first one is the pre–processing of the input data (called WRF Preprocessing System, or WPS). This module has the purpose of adapting input data to WRF for real–data simulations. WPS module defines the nested domains, computes latitude, longitude, map scale factors and Coriolis parameters at every grid point, and interpolates time–invariant terrestrial data to simulation grids (e.g., terrain height, soil type, landuse). The WPS module generates finally a file for each domain which includes all the meteorological and geographical information that WRF model will read. For this purpose, WPS included three independent programs: geogrid, ungrid and metgrid, as shows Fig. 1.8.

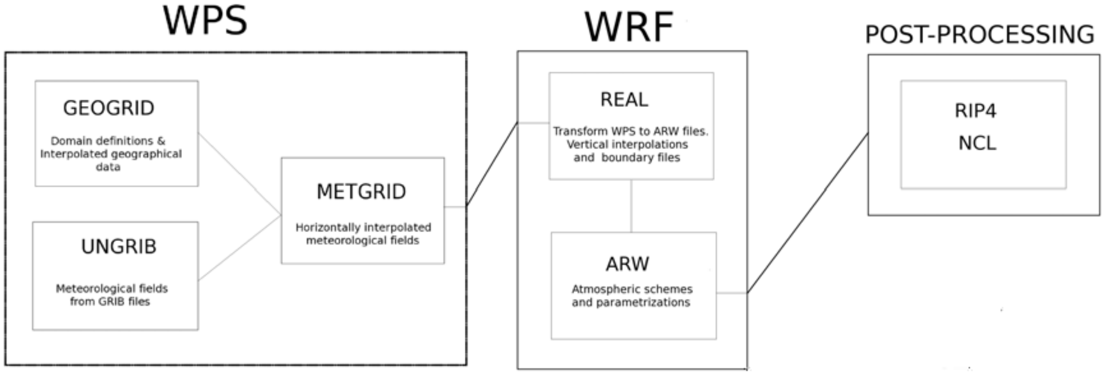

Figure 1.8: WRF–ARW modelling system flow.

Geogrid stands for GEOgraphical GRID. This program defines the map projection, geographical location and dimensions of domains, provides values for a static (time–invariant) fields at each model grip point: compute latitudes, longitudes, map scale factor and Coriolis parameters at each grid point, and horizontally interpolate static terrestrial data (e.g. topography height, landuse, soil type, vegetation fraction, monthly surface albedo).

Ungrib stands for UNdo and GRIB. Grib is a Word Meteorological Organization standard file format for storing regularly–distributed fields (Generated Regularly–distributed Information in Binary, GRIB). Ungrib program reads GRIB files and extract meteorological fields, and if necessary derives required fields from related ones (e.g. compute relative humidity from temperature, pressure and specific humidity), and write requested fields to an intermediate file format.

Geogrib and ungrib work in an independent way, generating the corresponding files to be used as input files for the last program, Metgrid, which means METeorological GRID. This program horizontally interpolates meteorological data (extracted by ungrib) and adapts this data to the domains defined by geogrid. Finally, vertical interpolation to WRF η–levels is performed in the second stage, called REAL module.

REAL program takes data from the previous module, WPS, and transforms it to be included as input in the WRF modele. This program vertically interpolates those files that metgrid program generated, and creates boundary and initial condition files.

WRF module contains many basic options concerning several atmospheric schemes, such as the boundary layer, microphysics, cumulus, physical interactions, surface fluxes, radiation, and soil, that each user can modify according to the meteorological event to be simulated.

Once the numerical simulation finishes, program RIP4 is used in this thesis for plotting and extracting the values in a certain point of different atmospheric variables. The main variables used along this thesis are: the potential, virtual potential and equivalent potential temperature, wind field, air divergence, 1–h accumulated precipitation, cloud mixing ratio and water vapor mixing ratio, lifted condensation level (LCL), level of free convection (LFC) and the convective available potential energy (CAPE).

WRF–ARW model physical parametyrizations

The following physical parameterizations have been used in this Thesis. For the PBL parameterization MRF scheme is used (Hong and Pan, 1996), RRTM scheme for longwave radiation (Mlawer et al., 1997), MM5 shortwave scheme for shortwave radiation (Dudhia, 1989), and WSM 6–class scheme (Hong et al., 2004) for the microphysics parameterization. No cumulus parameterization is used for any of the smallest domains because the horizontal resolution is lower than 3 km in all the simulations. Concerning to the vertical resolution, 42 η–vertical levels have been defined. The initial and boundary conditions were updated every six hours with information obtained from the analysis of the ECMWF reanalysis model at 0.125° of horizontal resolution. Two–ways nesting method is used in the simulations. Depending on the horizontal scale of the coastal front, three or four nested domains are defined, the smallest domain having 1, 2 or 3 km of horizontal resolution.

1.5 Observed coastal fronts in the Mediterranean basin

By applying the methodology described above, 17 coastal fronts (hereafter CFs) have been detected since 2004 (searching in a random way). Among them, 10 are presented here, covering many areas on the whole Mediterranean basin. Figure 1.9 shows the location of the simulated CFs.

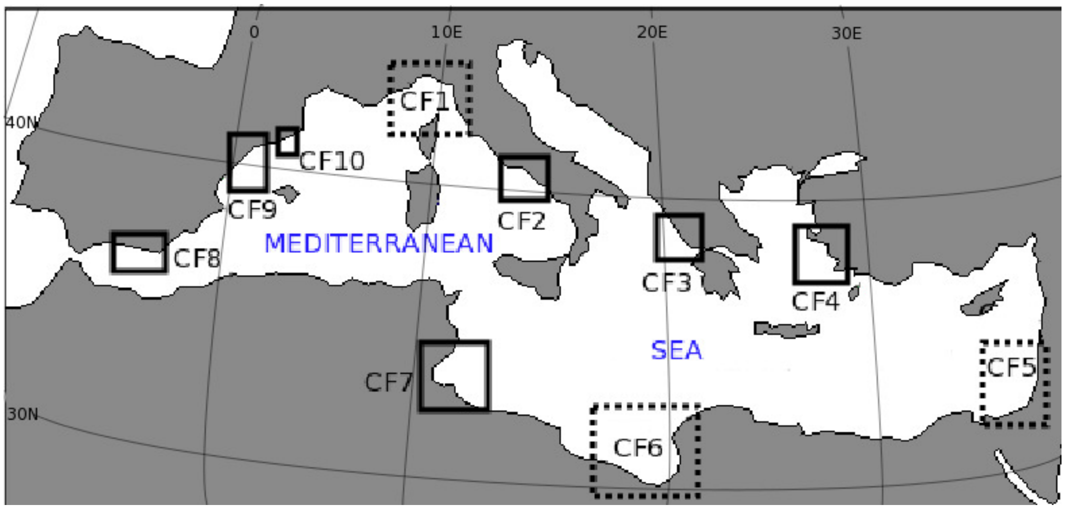

Figure 1.9: Location on the Mediterranean basin of the 10 presented coastal fronts. The dashed black squares indicate quasi–stationary coastal fronts.

Table 1.1 shows the date when the CFs occurred, the number and the horizontal resolution of the nested domains, and the geographical location of the center of the biggest domain of the numerical simulations. All the studied CFs occurred during autumn and winter. During this period the largest sea–land thermal difference occurs, and then large drainage wind speed favors the CF formation.

Event	Data	Domains (km)	Center largest domain
CF1	29 Jan 2008 (23 UTC)	18, 6, 2	44°N–9°E
CF2	28 Sept 2004 (00 UTC)	3	42°N–14.5°E
CF3	4Oct 2011 (00 UTC)	27, 9, 3, 1	39°N–21°E
CF4	3 Dec 2010 (00 UTC)	18, 6, 2	40°N–25°E
CF5	6 Jan 2011 (22 UTC)	27, 9, 3, 1	32.1°N–34.8°E
CF6	30 Jan 2008 (00 UTC)	18, 6, 2	32°N–18°E
CF7	4 Dec 2010 (00 UTC)	18, 6, 2	35.5°N–10.5°E
CF8	3 Mar 2011 (23 UTC)	18, 6, 2	38.4°N–4.25°W
CF9	6 Sept 2011 (23 UTC)	18, 6, 2	41.9°N–2.07°E
CF10	11 Oct 2011 (00 UTC)	27, 9, 3, 1	42°N–2°E

Table 1.1: Date of occurrence, resolution of the nested domains used in WRF numerical simulation and location of the larger domain.

1.6 Aim, approach and outline of the thesis

The main goal of this thesis is to study nocturnal coastal fronts in the Mediterranean basin responsible for the nocturnal offshore precipitation near the coastline filling the lack of knowledge on the Mediterranean meteorology concerning this phenomenon.

The specific objectives can be formulated as six detailed research questions that are addressed throughout the thesis:

1. Are the physical processes responsible for the precipitation associated to nocturnal coastal fronts on the Mediterranean basin the same as those found by other authors on the tropical regions?
2. What are the main factors influencing this mechanism of precipitation?
3. What is the meteorological scale in which these events occur?
4. In which synoptic atmospheric conditions do these events form?
5. Why do cloud bands sometimes develop producing showers and rainbands, and sometimes no cloud appear?
6. Would it be possible to forecast the cloud bands formed at the coastal–front by using a simple empirical index?

The rest of the thesis is divided into five main chapters with the following contents:

In **Chapter 2** we study some CF characterized by relatively large land–sea thermal gradient.

Chapter 3 focusses on the importance of the concave coastline shape in converging offshore the drainage winds.

Chapter 4 is divided in two parts related to the SST. The first one aims at showing some CF which develops in a warm sea surface temperature. In the second part, a sensibility analysis of the SST on precipitation associated to some CF has been analyzed by doing numerical experiments.

Chapter 5 focusses on the role of the coastal front depth on rain and cloud band formation over the investigated events, and proposes an index useful for forecasting cloud bands.

Chapter 6 contains the overall conclusions of this thesis.

Finaly, regarding the meteorological scales in which the CFs develop and taking into account the observation and simulation of a meso–α coastal front formed during the day over the West Mediterranean basin, in the Appendix A the West Mediterranean basin is defined as a frontogenesis region in the whole mesoscale.

The main publications and contributions to internationals meetings related with the research topics presented in this thesis are:

i) International meetings

Mazon, J. & Pino, D. 2011 The role of nocturnal Low–Level–Jet in nocturnal convection and rainfalls in the Mediterranean coast: the episode of 14th December 2010 in northeast of the Iberian Peninsula. In *EMS Annual Meeting 2011* Vol. 8, pp. 133. 12–16 September 20122, Berlin. Germany.

Mazon, J. & Pino, D. 2012 The role of large sea–land temperature, the coastline shape and the SST in the nocturnal offshore convection in the Mediterranean basin. In *EMS Annual Meeting 2012* Vol. 9, pp. 209. 10–14 September 2012, Lodz. Poland.

Mazon, J. & Pino, D. 2013 The role of the nocturnal–coastal–front height in the ocurrence of clouds and rain bands in the Mediterranean basin. In *EMS Annual Meeting 2013* Vol. 10, pp. 137. 9–13 September 2013, Reading. UK.

Mazon, J. & Pino, D. 2013 Frontogenesis in the meso–α and meso–β scales in the Mediterranean basin: from cloud arch to cloud cells. In *4th International Meeting on Meteorology and Climatology of the Mediterranean* 27 February–1 March 2013, Banyuls sur Mer. France

Mazon, J. & Pino, D. 2013 Nocturnal offshore precipitation near the coastline in the Mediterranean. In *4th International Meeting on Meteorology and Climatology of the Mediterranean* 27 February–1 March 2013, Banyuls sur Mer. France

Mazon, J. & Pino, D. 2013 The influence of the sea surface temperature on the nocturnal offshore line of precipitation near the Mediterranean coastline. In *EGU Annual assembly 2013* EGU2013–1326. 7–12 April 2013, Viena. Austria.

Mazon, J. & Pino, D. 2012 Stationary nocturnal offshore precipitation near the coastline in the Mediterranean basin. In *Plinius Conference 2012* Vol.14, pp. 47. 13–16 November 2013, Palma de Mallorca. Spain.

Mazon, J. & Pino, D. 2011 The role of drainage winds in the formation of nocturnal convective systems in the western Mediterranean basin. In *5th HyMex Workshop 2011* pp. 5. 17–19 May 2011, Maó. Spain

ii) Publications

Mazon, J. & Pino, D. 2012 The role of nocturnal Low–Level–Jet in nocturnal convection and rainfalls in the west Mediterranean coast: the episode of 14 December 2010 in the north-east of the Iberian Peninsula. *Adv. Sci. Res.* **8** pp. 27–31. doi:110.5194/asr–8–27–2012.

Mazon, J. & Pino, D. 2013*a* Nocturnal offshore precipitation near the Mediterranean coast of the Iberian Peninsula. *Meteorol. Atmos. Phys.* **120** pp. 11–28. doi:10.1007/s00703–012–0229–1.

Mazon, J. & Pino, D. 2013*b* The role of sea–land air thermal difference, shape of the coastline and sea surface temperature in the nocturnal offshore convection. *Tellus A* **65** 20027 http://dx.doi.org/10.3402/tellusa.v65i0.20027

Mazon, J. & Pino, D. 2014 Mesoscale numerical simulation of heavy nocturnal rain-bands associated with coastal fronts in the Mediterranean Basin. *Nat. Hazards Earth Syst. Sci.* **14** pp. 1185–1194. doi:10.5194/nhess–14–1185–2014.

Mazon, J. & Pino, D. 2015 Role of the nocturnal coastal–front depth on cloud and rain formation in the Mediterranean basin. *Atmos. Res.* **153** pp. 144–154. DOI: 10.1016/j.atmosres.2014.08.004

Chapter 2

Land–sea air temperature differences

2.1 Introduction

Thermal gradient between the air over the land and sea enhances drainage winds (Meyer, 1971; Schoenberg, 1984a; Khain et al., 1993; Heiblum et al., 2011). The inland cold air moves offshore driven by these drainage winds. A coastal–front forms when this cold inland air interacts with the warmer sea–air. Then, cloud bands and precipitation can appear. These authors concluded that the intensity and the position of the precipitation at the coastline are determined by the magnitude of the prevailing winds and the land–sea air temperature difference. Large prevailing wind speed shifts precipitation onshore, while large land–sea air temperature difference moves the convective area offshore. By using the MM5 mesoscale model (Dudhia, 1993), Malda et al. (2007) analyzed some of the mechanisms that favor the formation of coastal fronts in The Netherlands. They performed several numerical experiments to analyze the nocturnal front formed on the night of 13 August 2004 at the coastline of The Netherlands. An increase in SST shifted the precipitation areas offshore. Consequently, differences between inland air temperatures and SST play an important role in locating the precipitation associated with the coastal front. Mapes et al. (2003a) described the mechanism of nocturnal convection offshore the Pacific coastline in Central America, by using MM5 simulations. They determined that low inland air temperatures favor large drainage winds offshore which in turn plays an important role in the intensity of convection and the position of the line of precipitation.

Among the 10 simulated CFs (see Table 1.1 and Fig. 1.9) three are characterized by a relatively large sea–land air thermal difference, and they are shown in this chapter[a]. The

---

[a] This chapter is based on Mazon, J. and Pino, D.: The role of sea–land air thermal difference, shape of the coasline and sea surface temperature in nocturnal offshore convection. Tellus **A** 2013, 65, 20027, http://dx.doi.org/10.3402/tellusa.v65i0.20027 and Mazon, J. and Pino, D.: Nocturnal offshore precipitation

CF5 and CF8 occurred in wintertime, with around 8 and 9 K of sea–land thermal difference, respectively, and CF10 in mid-autumn, with 6 K of sea–land thermal difference. Well–defined lines of convergence longer than 100 km are simulated in CF5 and CF8, and around 30 km in CF10.

2.2 The quasi–stationary rainband associated to CF5

2.2.1 Observations

Several convective cells formed offshore near the coastline of Israel and Lebanon during the night and early morning of 6 January 2011 (Heiblum et al., 2011). These authors studied the precipitation in Israel using TRMM database and reflectivity radar images: they showed the precipitation associated to this event as an example of a stationary offshore line of precipitation due to a land–breeze front. Figure 2.1 shows the location in the Mediterranean basin where this event occurred.

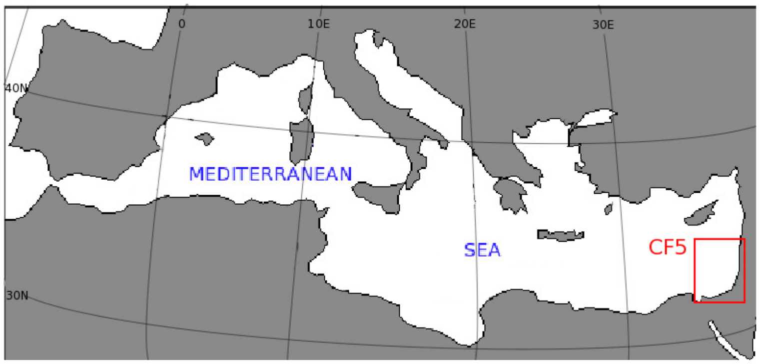

Figure 2.1: Location (red square) in the Mediterranean basin where CF5 occurred.

According to the 3-hours accumulated precipitation detected by TRMM, the precipitation appeared after 21:00 UTC on 5 January, and disappeared before 06:00 UTC on 6 January 2011. Figure 2.2a shows the 3–h accumulated precipitation at 03:00 UTC obtained by TRMM satellite with a maximum value of around 18 mm offshore at the southern coastline of Israel, and lower at the northern coastline, from 4 to 8 mm. Figure 2.2b shows the Meteosat satellite infrared image at 03:00 UTC on 6 January 2011, in which an offshore cloud band is observed in front of the Israel coastline at 03:00 UTC.

---

near the Mediterranean coast of the Iberian Peninsula. Meteorol. Atmos. Phys., 2013, 120:11–28, doi 10.1007/s00703–12–0229-1

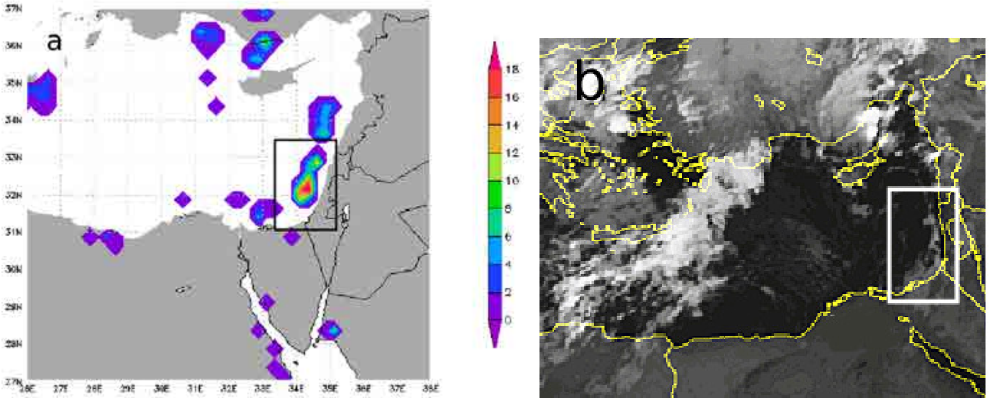

Figure 2.2: (a) 3–h accumulated precipitation estimated by TRMM and (b) IR Meteosat satellite image at 03:00 UTC on 6 January 2011. The square indicates the location of domain 3 used in the simulation.

2.2.2 Synoptic analysis

Figure 2.3a shows the NCEP reanalysis geopotential height at 500 hPa and the surface pressure at 00:00 UTC on 6 January 2011. At sea level, the pressure is 1020 hPa over the eastern Mediterranean basin. Another high-pressure area was located over the central Mediterranean Sea. A small and weak low-pressure area (1012 hPa) was located in southern Turkey during those days (not shown), inducing a easterly flow over the Israel coastline. Figure 2.3b shows the NCEP reanalysis temperature at 850 hPa. The whole Mediterranean basin is affected by a relatively weak North cold advection, with around 8°C in the easter Mediterranean area at 00:00 UTC on 5, and around 10°C at 00:00 UTC on 6 January 2011. No significant horizontal gradient of temperature was observed in the eastern Mediterranean Sea at 850 hPa.

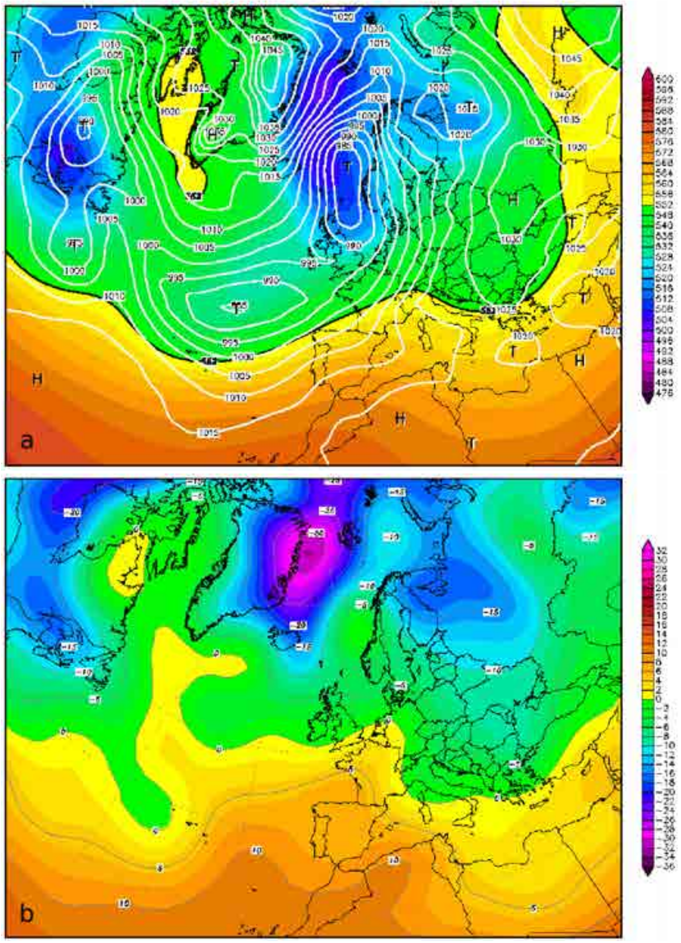

Figure 2.3: NCEP Reanalysis of (a) geopotential height at 500 hPa in decameters (color contours) and sea level pressure (white isolines) and (b) temperature field (color contours) at 850 hPa on 6 January 2011 at 00:00 UTC.

2.2.3 WRF–ARW simulation

The WRF simulation includes 4 nested domains with a horizontal grid space of 27, 9, 3 and 1 km, and 50×40, 76×64, 85×97 and 70×70 points, respectively. Figure 2.4 shows the nested domains (upper panel) and the orography at domain 3 (lower panel) which covers the whole rainband occurred on the Israel and Lebanon coastline. The simulation begins at 00:00 on 5 January and finishes at 18:00 UTC on 7 January 2011.

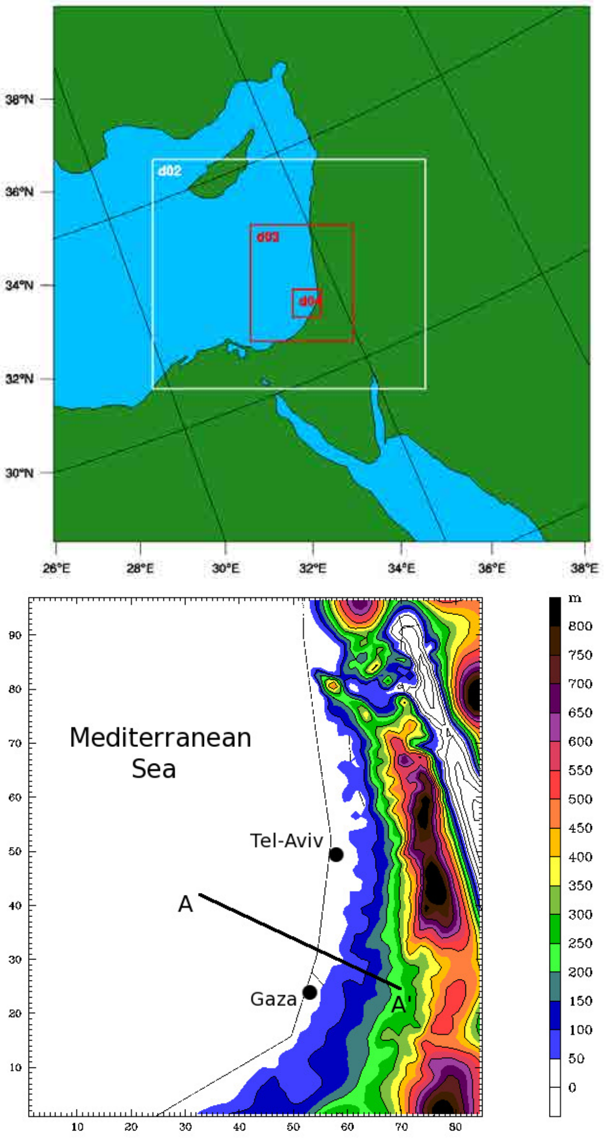

Figure 2.4: Nested domains (upper panel) and the orography at domain 3 (lower panel, 3 km horizontal resolution) defined in WRF simulation for studying CF5. The blue line AA' indicates the projection of the vertical cross section used to analyze the episode. The contour lines are drawn every 200 m.

In order to analyze the sea–land air thermal differences, Fig. 2.5 shows the simulated 2–m potential temperature (color contours) and wind field (arrows) in domain 3 at 03:00, 06:00 and 08:00 UTC on 6 January 2011. Values around 280–282 K over land, and around

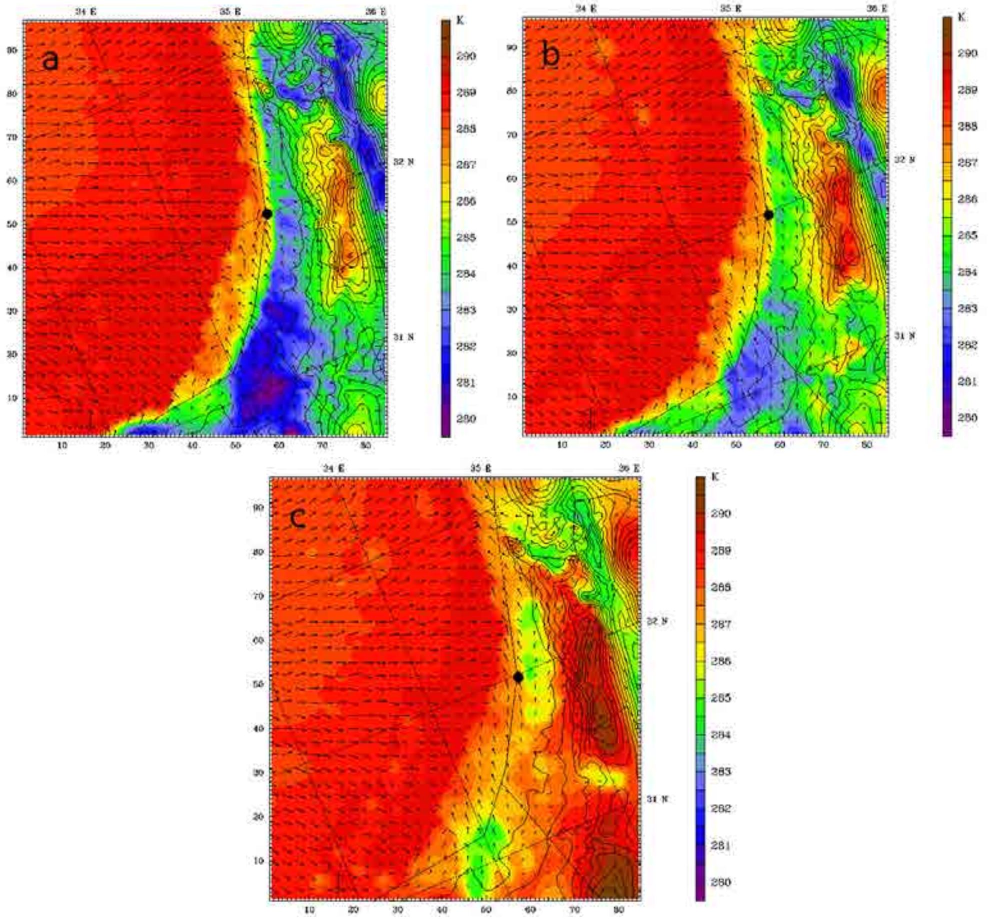

Figure 2.5: Simulated surface potential temperature (color contours) and wind field (arrows) in domain 3 at (a) 03:00 UTC, (b) 06:00 UTC and (c) 08:00 UTC on 6 January 2011. The maximum wind speed in each plot is 6.8 m s^{-1}, 7.1 m s^{-1} and 6.1 m s^{-1}. The black dot indicates the city of Tel–Aviv. The orographic contours are plotted every 300 m.

290 K over the sea are simulated at 03:00 and 06:00 UTC (Figs. 2.5a and b). This thermal difference promotes large drainage wind speed reaching to 7 m s^{-1}, a value comparable with the velocity of the simulated westerly prevailing flow. At 08:00 UTC (Fig 2.5c), the land–sea air thermal difference reduces significantly, and consequently the drainage wind speed. After sunrise the land–sea air thermal difference is largely reduced and the drainage wind vanishes.

In order to identify the coastal front associated to the cold outbreak lead by the drainage wind, Fig. 2.6 shows the simulated surface divergence (color contours) and wind field (arrows) in domain 3 at several hours during the night of 6 January 2011. Two different areas of convergence appear in the simulation. The first one is located inland as a result of the

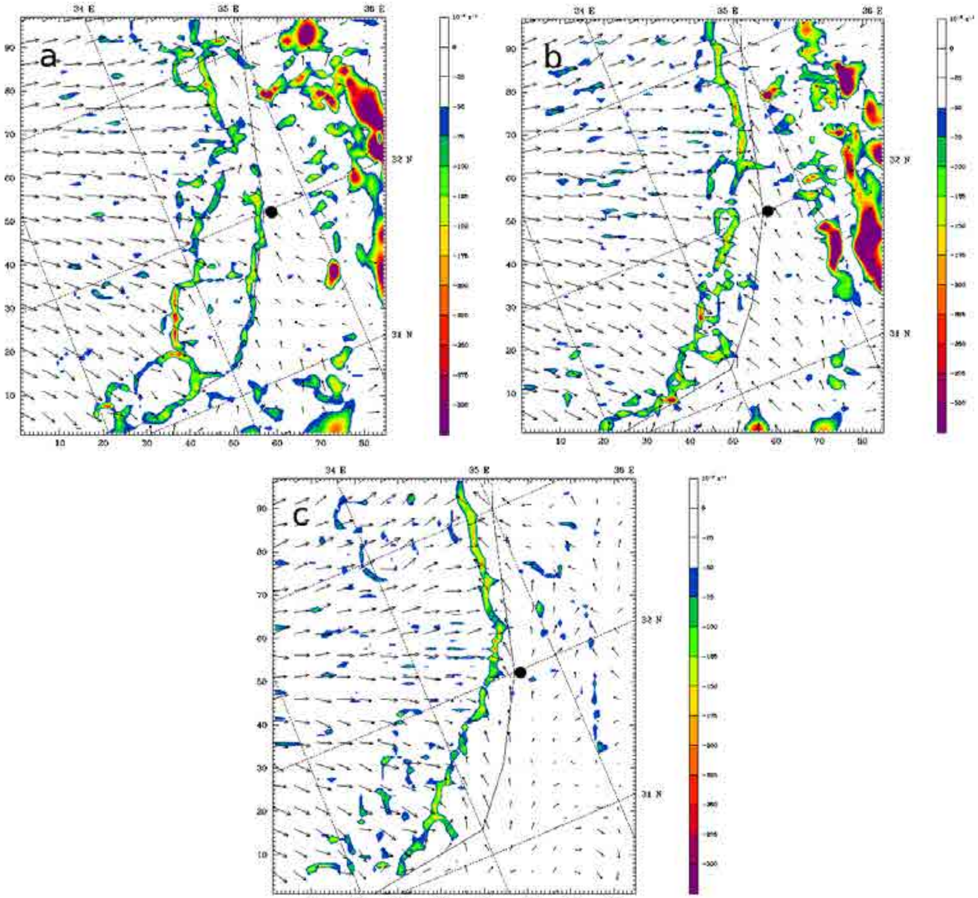

Figure 2.6: Simulated surface divergence (negative convergence, color contours) and wind field (arrows) in domain 3 at (a) 00:00 UTC, (b) 04:00 UTC and (c) 08:00 UTC on 6 January 2011. The maximum wind speed is 7.4 m s^{-1}. The black dot indicates the city of Tel–Aviv. The

orography. The second area, few kilometers offshore, is formed due to the interaction of a cold air mass driven by the drainage wind with a warmer one driven by the prevailing westerly wind. This line of convergence is quasi–stationary for several hours (from 00:00 to 08:00 UTC).

Around this line of convergence the model simulates several convective cells that produce precipitation. Figure 2.7 shows the simulated hourly accumulated precipitation pattern and the surface wind field in domain 3 at several hours. Several precipitation cells appear around the line of convergence, forming an offshore precipitation line that remains practically stationary from 00:00 to 08:00 UTC on 6 January. Afterwards, some precipitation cells are displaced onshore, producing inland precipitation near the coastline.

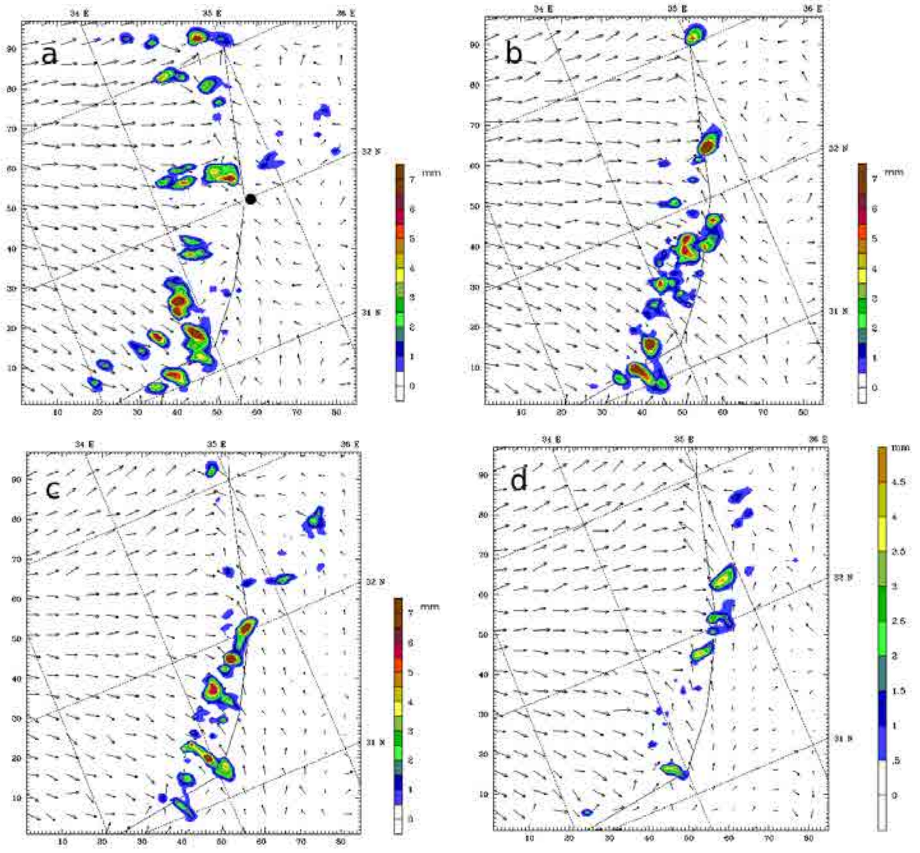

Figure 2.7: Simulated 1–h accumulated precipitation (color contours) and surface wind field (arrows) at (a) 00:00 UTC, (b) 04:00 UTC, (c) 06:00 UTC and (d) 08 UTC on 6 January 2011. The black dot indicates the city of Tel-Aviv. The maximum wind speed is 6.8 m s^{-1} (a), 6.1 m s^{-1} (b), 7.3 m s^{-1} (c) and 6 m s^{-1} (d).

In order to evaluate the depth of the cold air mass, Fig. 2.8 shows the potential temperature (color contours), the equivalent potential temperature (black contour lines) and the wind field (arrows) at the vertical cross section along the line AA' shown in Fig. 2.4 at several hours on 6 January 2011. From 00:00 UTC (Fig. 2.8a), a cold air mass remained stationary few kilometers offshore until early morning (Fig. 2.8d). At the head of the cold drained air mass associated to the coastal front, the warm and wet air mass moves upwards, transporting moisture and heat, as indicated by the equivalent potential temperature contour lines (values of around 308 to 310 K at sea level). Atmospheric instability is detected at low levels, as indicated by the decrease of the equivalent potential temperature with height, from 309 K at sea level to 304 K between 1500 and 2000 m. This instability favors the upward transport of heat and moisture from the sea surface (290 K of potential temperature and around 10 g kg^{-1} of absolute humidity). The maximum vertical wind speed occurs from 03:00 to 06:00 UTC, corresponding to the maximum cell formation (see Fig. 2.7b and 2.7c).

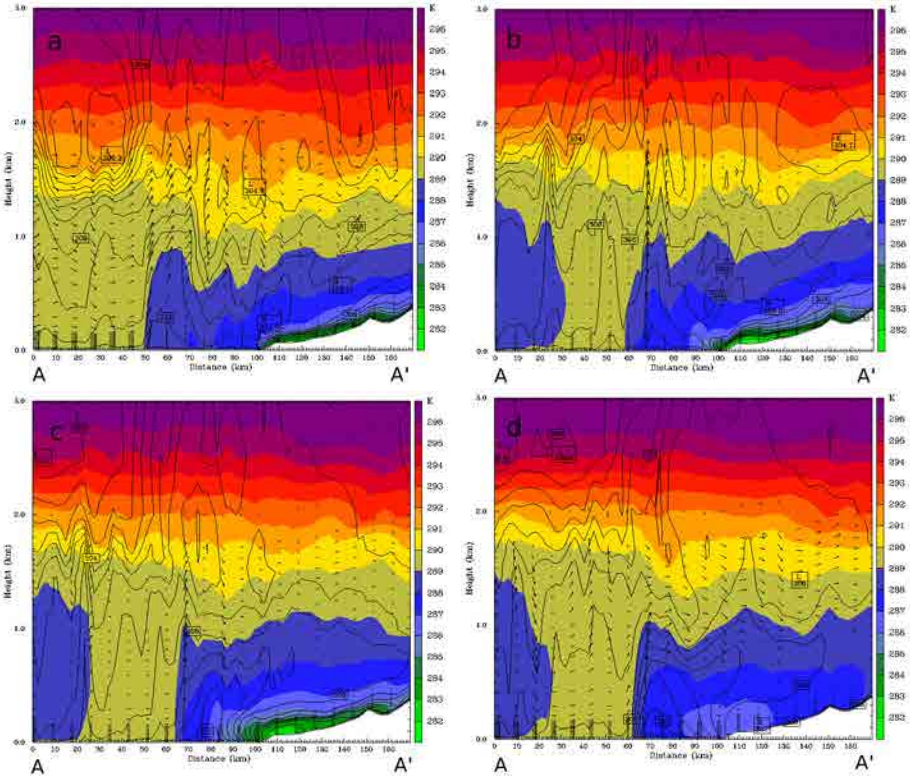

Figure 2.8: Vertical cross section along the blue line AA' shown in Fig. 2.4 of the simulated potential temperature (color contours), equivalent potential temperature (black contours lines) and wind field (arrows) at (a) 00:00 UTC, (b) 04:00 UTC, (c) 06:00 UTC and (d) 08:00 UTC on 6 January 2011.

The warm and wet air moved upward over the cold air at 1.1 m s^{-1} of vertical velocity reaching more than 3000 m. The simulated CAPE shows the maximum values from this time, reaching 867 J kg^{-1} at 07:00 UTC, which suggest that weak convection produced this precipitation. At 06:00 UTC (Fig. 2.8c) the vertical velocity decreases to 0.9 m s^{-1} and the maximum height is 2000 m. At 08:00 UTC (Fig. 2.8d) the vertical velocity decreases to 0.4 m s^{-1} and the air only reaches 1000 m.

The depth of the cold air mass increases from 500–600 m at 00:00 UTC (see Fig. 2.8a) to 1000 m at 06:00 and 08:00 UTC (Figs. 2.8c, d) due to the stationarity of the front. Along the line of precipitation, the simulated LFC is located between 600 m and 800 m from of 00:00 to 08:00 UTC.

2.3 The rainband associated to CF8

2.3.1 Observations

During the night on 4 March 2011 several precipitation cells were recorded by reflectivity radar images along the southern coast of the Iberian Peninsula. Figure 2.9 shows the location where this precipitation occurred.

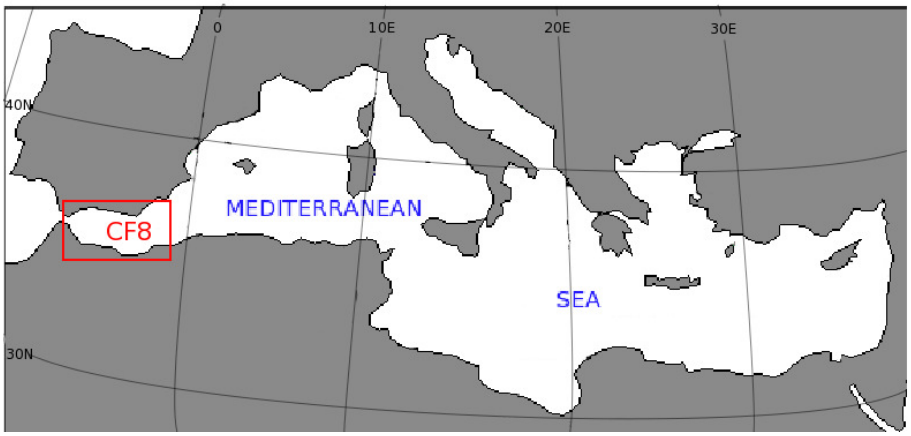

Figure 2.9: Location of the region where CF8 (red square) occurred within the Mediterranean basin.

Figure 2.10 shows radar reflectivity on 4 March 2011 at 04:00, 06:00 and 08:00 UTC. At 04:00 UTC (Fig. 2.10a), several individual precipitation cells were recorded offshore close the coastline of South Iberian Peninsula, forming a line of precipitation of around 200 km large. This line of precipitation remained for several hours approximately at the same location until 06:00 UTC (Fig. 2.10b). From 08:00 UTC (Fig. 2.10c) the precipitation occurred inland at the western part of the coastline.

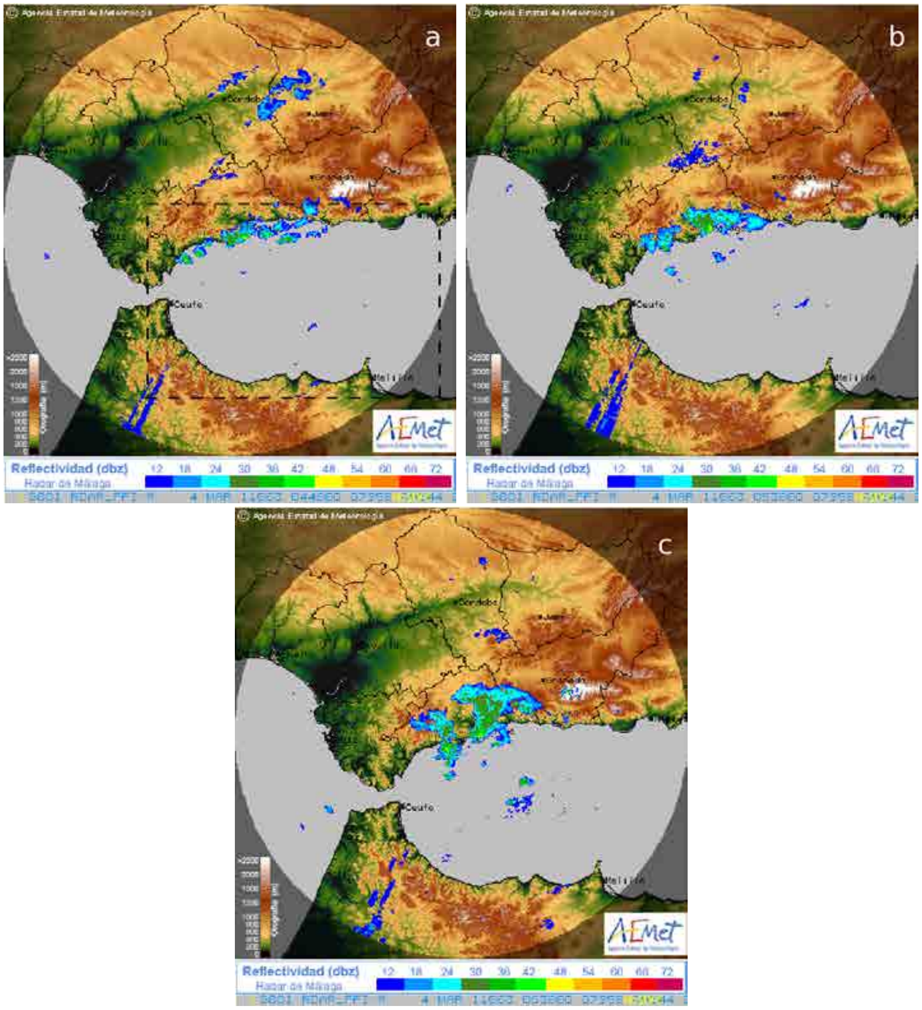

Figure 2.10: Observed radar reflectivity at 1000 m of Constant Altitude Plan Position Indicator (CAPPI images) taken by the Spanish Weather Agency at 04:00 UTC (a), 06:00 UTC (b) and 08:00 UTC (c) on 4 March 2011. The radar range covers 230 km of radium. The dashed line shown in (a) indicates the domain 3 used in simulation.

2.3.2 Synoptic analysis

From 28 February until 3 March 2011, the NCEP reanalysis shows a cold air mass at 850 hPa located over the Iberian Peninsula, elongated from the northeast to the southwest. Figure 2.11a shows the temperature field at 850 hPa on 4 March 2011 at 00:00 UTC. A cold air mass, displaced from the north circulation, is located from the north to the south along the Iberian Peninsula, with temperatures below 0°C at this height. Figure 2.11b shows the

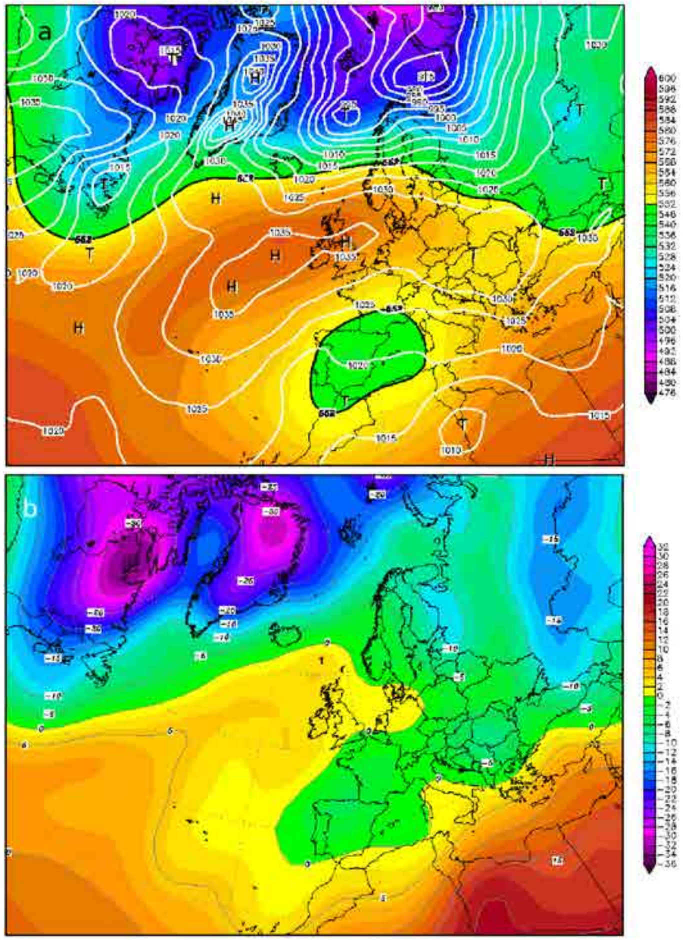

Figure 2.11: NCEP Reanalysis of (a) geopotential height in decameters at 500 hPa (color contours) and sea level pressure (white contour lines) and (b) the temperature field (color contours) at 850 hPa on 4 March 2011 at 00:00 UTC.

500 hPa and surface pressure at 00:00 UTC on 4 March 2011. Low values of geopotential height existed over the Iberian Peninsula and the western Mediterranean Sea. At sea level, no significant gradient of pressure is observed.

2.3.3 WRF–ARW simulation

Three nested domains with 70×70, 100×130 and 118×193 grid points and horizontal resolutions of 18, 6 and 2 km, respectively, are defined in the WRF–ARW simulation. Figure 2.12 shows the nested domains. The smallest one is centered in the Alboran Sea and covers the whole coastline of this sea where the rainband occurred. The simulation begins at 00:00 UTC on 2 March 2011, and runs for 56 hours.

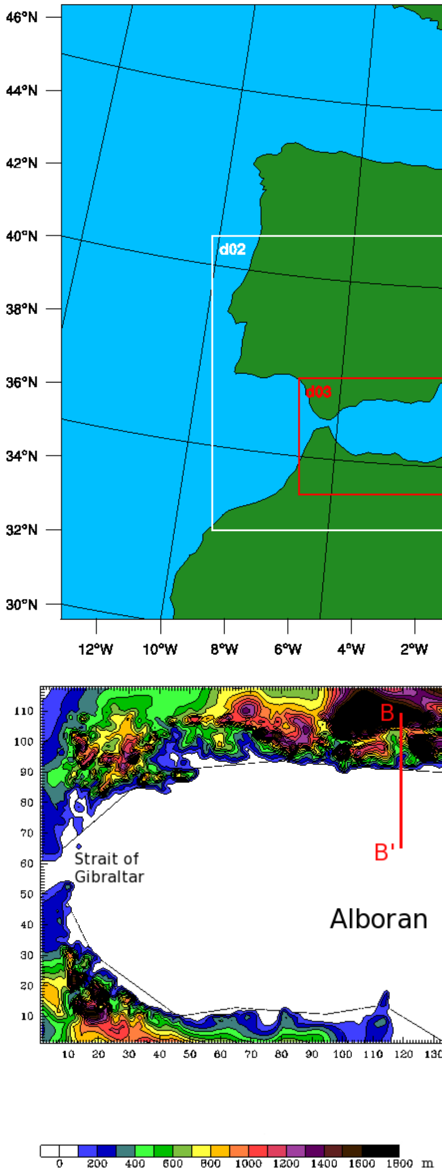

Figure 2.12: (a) Domains used in the WRF simulation and (b) orography in domain 3. The red line BB' indicates the direction for the vertical cross section for analysis done in section.

In order to study the sea–land thermal difference, Fig. 2.13 shows the surface virtual potential temperature and wind field simulated in domain 3 at 04:00, 06:00 and 08:00 UTC on 4 March 2011. The drainage winds bringing cold air to the sea can be observed in both the southern Iberian Peninsula and North African coasts. According to the WRF simulation, the virtual potential temperature of the warm and cold air masses is 288 K and 282 K, respectively. This thermal difference promotes relatively large drainage wind offshore. The velocity of the north–southerly drainage and easterly prevailing wind at 04:00 and 06:00 UTC (Figs. 2.13a and b) are around 6.5 m s^{-1} and 6.4 m s^{-1}, respectively.

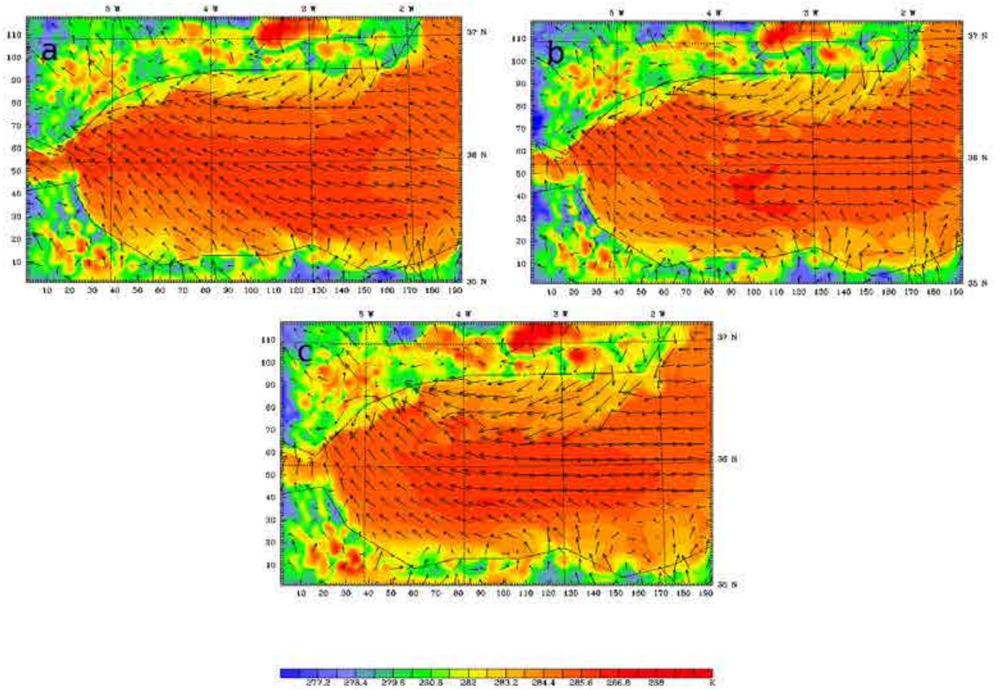

Figure 2.13: Simulated surface virtual potential temperature (color contours) and wind field (arrows) and in domain 3 on 4 March 2011 at (a) 04:00, (b) 06:00 and (c) 08:00 UTC. The maximum wind velocity is 6.5 m s^{-1} in (a), 6.4 m s^{-1} in (b) and 9.1 m s^{-1} in (c).

The drainage wind velocity from the mountain range close to the coast in the South of the Iberian Peninsula (see Fig. 2.12b) has similar wind speed at the coastline than the synoptic wind from the east, greater than 7 m s^{-1}, during several hours. The inland cold air moves offshore up to approximately 30 km lead by drainage winds, deflecting offshore to the west and moving more than 150 km parallel to the coastline. Along the path, this drained offshore air mass interacts again with the drainage winds moving down from the mountain slopes and at the mouths of rivers and streams in the most western areas.

In order to identify the coastal front formed offshore, Fig. 2.14 shows the simulated surface wind field and the divergence in domain 3. The model simulates two different convergence zones. The first one appears inland, representing areas with significant convection intensity caused by the interaction between the reliefs and the drainage and synoptic winds. Additionally, there is a convergence area offshore due to the interaction between the drainage wind and the easterly prevailing flow, where precipitation may occur.

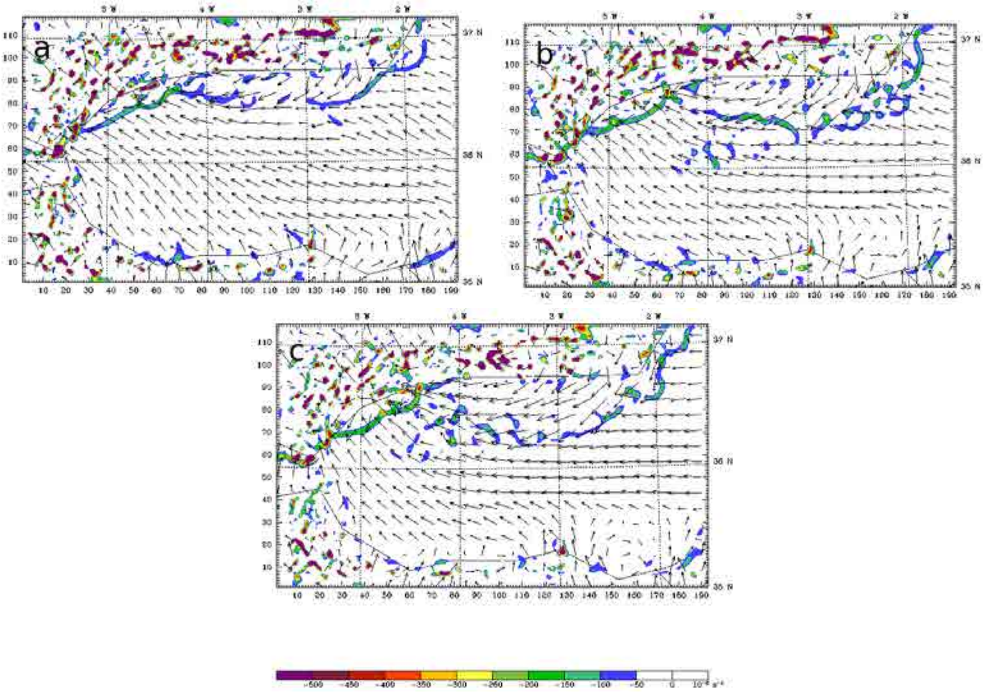

Figure 2.14: Simulated surface divergence (color contours) and wind field (arrows) and at (a) 04:00, (b) 06:00 and (c) 08:00 UTC on 4 March 2011 in domain 3. The maximum wind velocity is 6.5 m s^{-1} in (a), 6.4 m s^{-1} in (b) and 9.1 m s^{-1} in (c). The scale of the contour has been limited from 6.5 g kg^{-1} to 9 g kg^{-1}.

Figure 2.15 shows the surface specific humidity at 04:00, 06:00 and 08:00 UTC on 4 March 2011. Large values of specific humidity are simulated along the line of convergence. The convergence of air masses enhances vertical movements along the line.

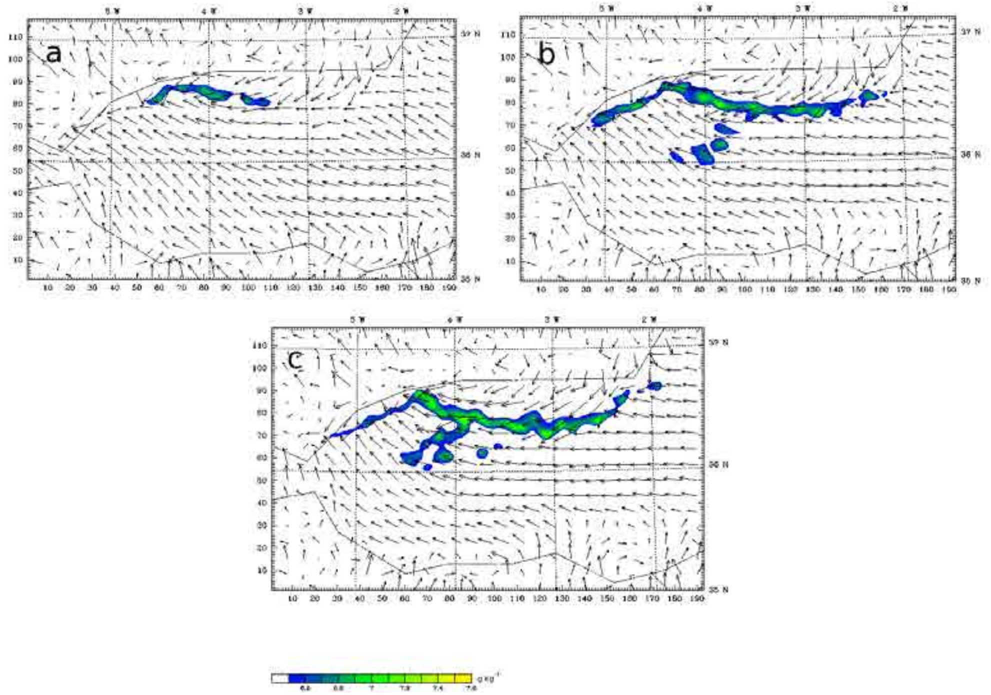

Figure 2.15: Simulated surface specific humidity (color contours) and wind field (arrows) at (a) 04:00, (b) 06:00, and (c) 08:00 UTC on 4 March 2011 in domain 3. The maximum wind velocity is 6.5 m s^{-1} in (a), 6.4 m s^{-1} in (b) and 9.1 m s^{-1} in (c)

1–h accumulated precipitation in domain 3 at 04:00, 06:00 and 08:00 UTC on 4 March 2011 is shown in Fig. 2.16. At 04:00 UTC, several individual precipitation cells are simulated at the west of the domain. The simulation reproduces the approximate precipitation detected by the radar, shown in Fig. 2.10. At 06:00 UTC, these individual cells grow and join, forming a large precipitation area. Several individual cells appear offshore, corresponding with the convergence and specific humidity bands shown in Figs. 2.14 and 2.15, respectively. The position of the simulated LFC over the coastal front head shows its minimum height around 06:00 UTC, between 600 and 700 m. At this time, the simulated CAPE shows the maximum values, around 315 J kg^{-1}. At 08:00 UTC the large precipitation area grows and more, smaller precipitation cells appear in the convergence band offshore. The large precipitation area obtained by the simulation at the extreme eastern area is not observed in the radar reflectivity, probably because this zone is off the radar coverage.

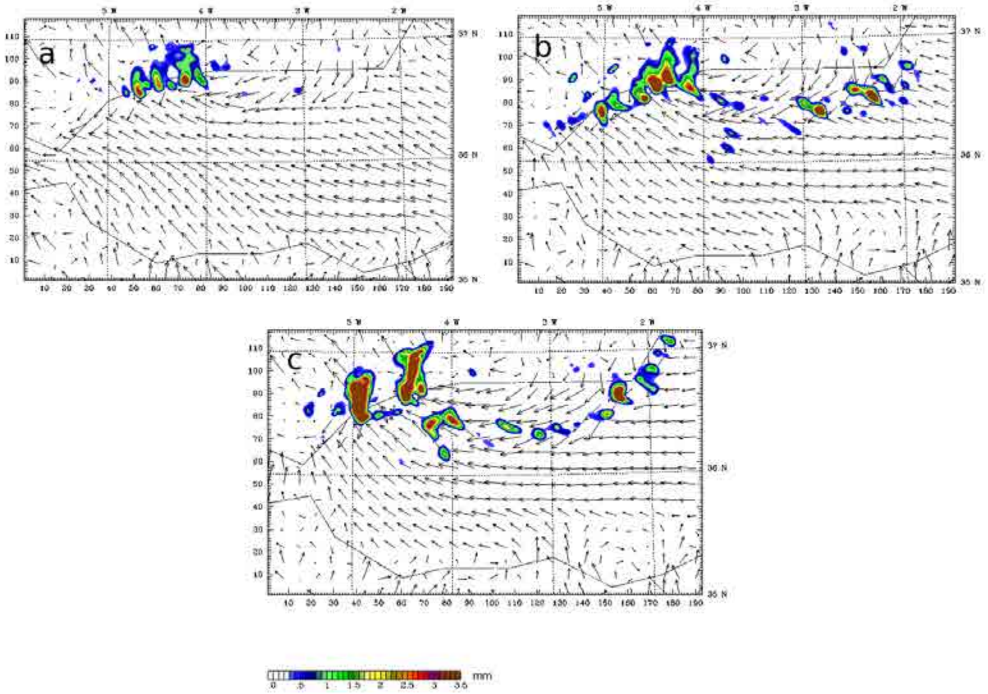

Figure 2.16: Simulated 1–h accumulated precipitation (color contours) and surface wind (arrows) in domain 3 at (a) 04:00, (b) 06:00 and (c) 08:00 UTC on 4 March 2011. The maximum wind velocity is 6.5 m s^{-1} in (a), 6.4 m s^{-1} in (b) and 9.1 m s^{-1} in (c)

2.4 Coastal front at the mouth of a river: CF10

2.4.1 Observations

The night of 13 October 2010 several precipitation cells occurred in the northeast of the Iberian Peninsula. Figure 2.17 shows the location of the area within the Mediterranean basin where this precipitation occurred.

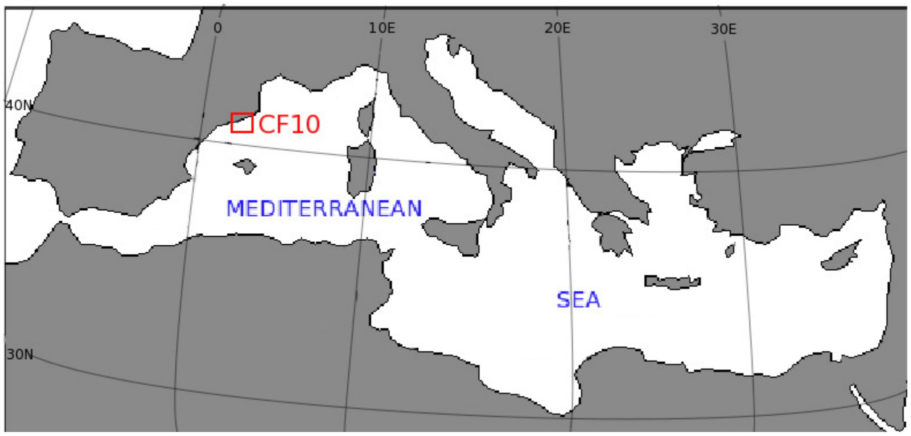

Figure 2.17: Location of CF10 (red square) in the Mediterranean basin.

Figure 2.18 shows the reflectivity radar images at 21:30 and 22:00 UTC on 13 October 2010. Three rainfall areas formed at the mouths of three rivers located in the northeast coast of the Iberian Peninsula: the Llobregat, Besos and Tordera rivers (indicate as L, B and T in Fig. 2.18a, respectively). The precipitation cells formed at 21:00 UTC, and moved offshore until 00:00 UTC.

2.4.2 Synoptic analysis

Figure 2.19a shows the geopotential height at 500 hPa and the surface pressure on 14 October 2010 at 00:00 UTC. A low-pressure area around 1005 hPa at sea–level is located over the middle Mediterranean Sea, which correspond with lower values of geopotential height at 500 hPa over this area. At sea–level, a prevailing northeasterly reaches the northeast of the Iberian Peninsula. A high pressure area was located in western Europe stretched approximately from Portugal to the west of the British Islands. At 850 hPa (Fig. 2.19b), a warm ridge from North Africa reach to southern Greece, with temperatures higher than 20°C. Over the western Mediterranean basin, a relatively cold outbreak is observed, with values around 10°C in the northeast of the Iberian peninsula.

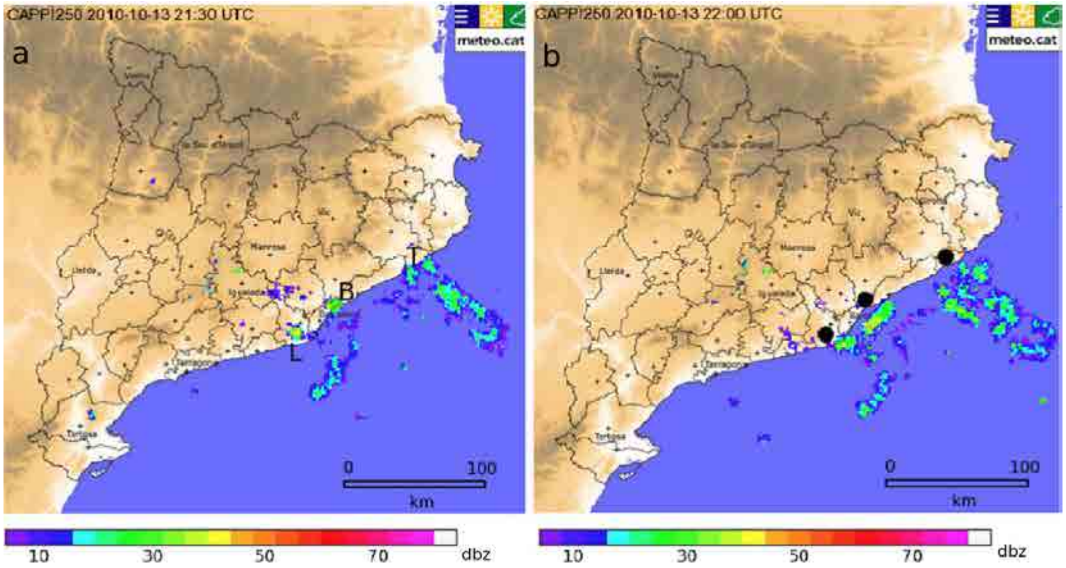

Figure 2.18: Observed radar reflectivity at 1000 m of CAPPI taken by METEOCAT at (a) 21:30 UTC and (b) 22:00 UTC on 13 October 2010. The black dots in (b) marks the mouth of the rivers Llobregat, Besos and Tordera, indicated as L, B, and T respectively in (a).

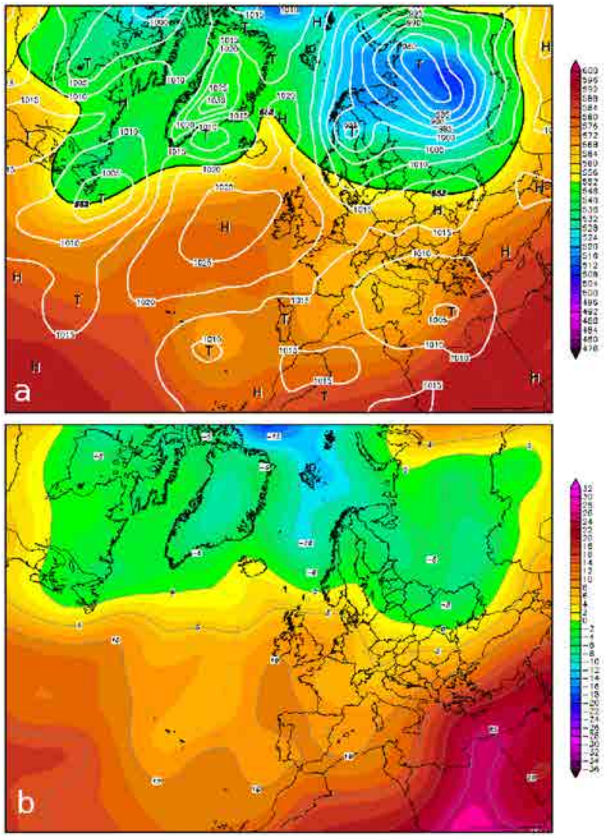

Figure 2.19: NCEP Reanalysis of (a) geopotential height in decameters at 500 hPa (color contours) and sea level pressure (white isolines) and (b) the temperature field (color contours) at 850 hPa on 14 October 2010 at 00:00 UTC.

2.4.3 WRF–ARW simulation

Figure 2.20a shows the four nested domains used in the simulation, with horizontal resolutions of 27, 9, 3 and 1 km respectively. The number of grid points defined at each domain is 50×50, 40×37, 52×52 and 70×90, respectively. The orography of the smallest domain is shown in Fig. 2.20b. It is centered at the mouth of the Llobregat river and also includes the mouth of the Besos River. The simulation begins on 11 October 2010 at 00:00 UTC, and finishes on 14 October 2010 at 18:00 UTC.

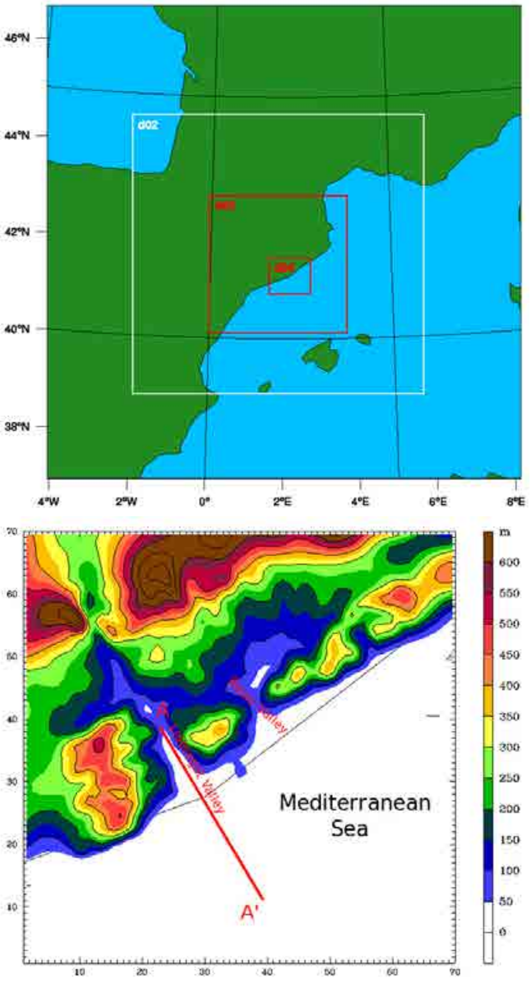

Figure 2.20: (a) Nested domains defined in the simulation. (b) Orography of domain 4. The line AA' indicates the direction for the vertical cross section for the analysis done in section.

To analyze the sea–land air thermal difference, Fig. 2.21 shows the simulated surface

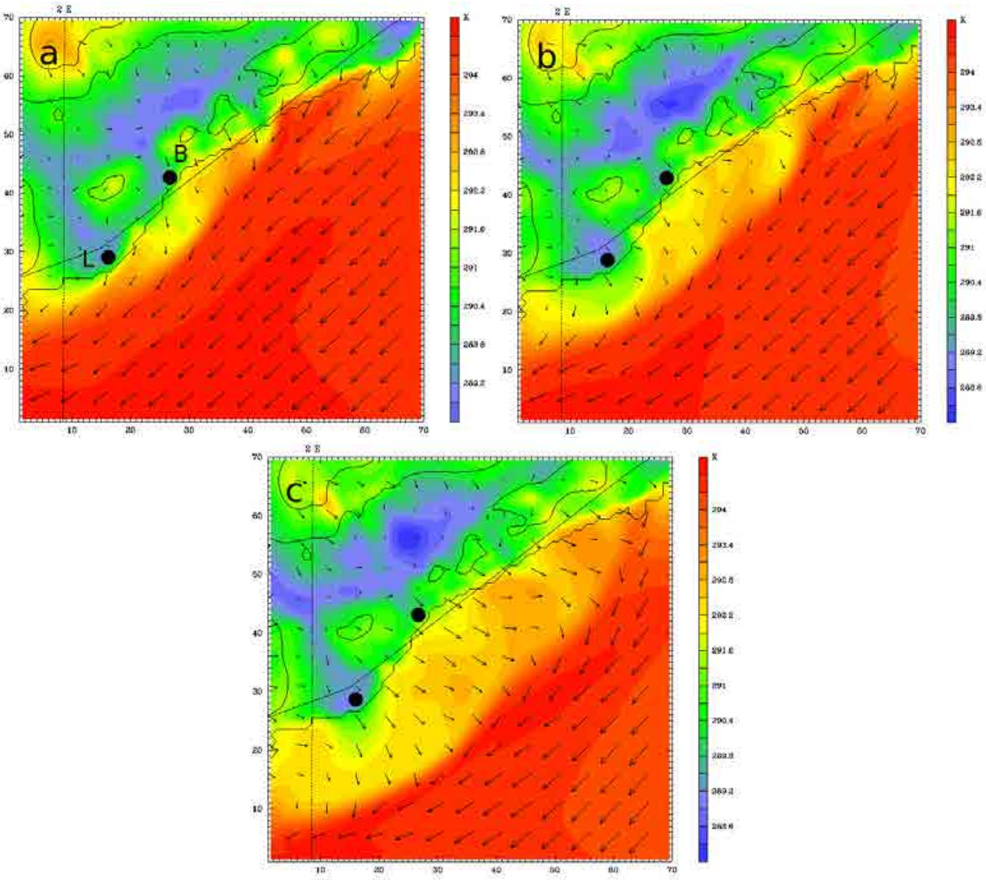

Figure 2.21: Simulated surface virtual potential temperature (color contours) and wind field (arrows) in the smallest domain at (a) 21:00 UTC and (b) 23:00 UTC on 13 October 2010, and (c) at 01:00 UTC on 14 October 2010. The maximum wind speed is 4.5 m s^{-1}, 5.2 m s^{-1} and 5.1 m s^{-1} respectively. The black dots indicate the mouth of the Llobregat and Besos rivers. The orographic contours are plotted every 500 m.

virtual potential temperature (contour color) and wind field (arrows) in the smallest domain, at 21:00 and 23:00 UTC on 13 October 2010 and at 01:00 UTC on 14 October 2010. At 21:00 UTC (Fig. 2.21a) a relatively large land–sea air thermal difference is simulated, with a temperature around 289 K inland in the mouth of the Llobregat and Besos rivers (indicated as L and B, respectively), and around 295 K over the sea. At 23:00 UTC (Fig. 2.21b), the drainage winds following the valley of both rivers drive the inland cold air mass offshore. At 01:00 UTC on 14 October 2010 (Fig. 2.21c) the cold inland air mass is located around 20 km offshore.

In order to identify the coastal front formed offshore, Fig. 2.22 shows the simulated surface divergence (color contours) and the wind field (arrows) in domain 4 at 21:00 and

23:00 UTC on 13 October 2010, and at 01:00 UTC on 14 October 2010. These areas of convergence form due to the interaction between the inland cold air mass lead offshore by drainage winds with the warmer one driven by the prevailing northeasterly. At 22:00 UTC (Fig. 2.22a) a line of convergence around 25 km long is simulated close to the coast, which at 23:00 UTC on 13 October 2010 move offshore and extend. This convergence band moves offshore quickly, increasing in convergence intensity and forming a front. At 01:00 UTC on 14 October 2010 (Fig. 2.22c) the simulated line of convergence, parallel to the coastline, shows their maximum extension, with around 85 km long located around 30 km offshore.

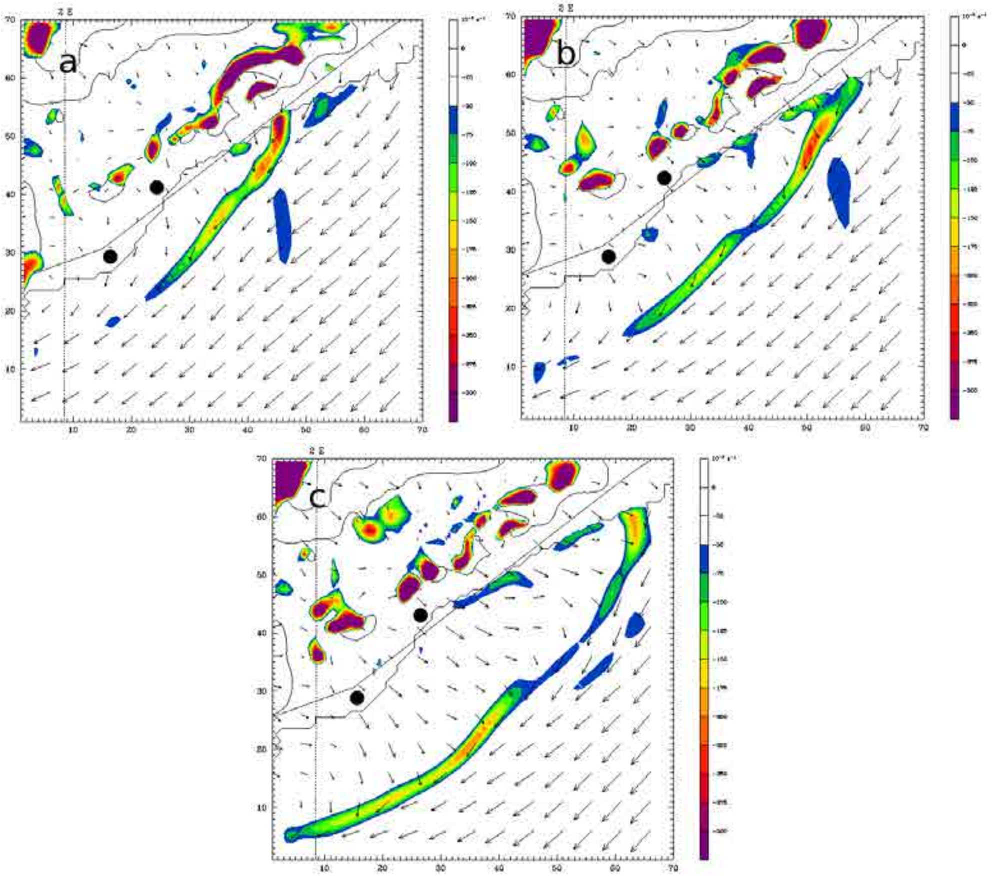

Figure 2.22: Simulated surface divergence (negative convergence, color contours) and wind field (arrows) in the smallest domain at (a) 21:00 UTC and (b) 23:00 UTC on 13 October 2010, and (c) 01:00 UTC on 14 October 2010. The orographic contours are plotted every 500 m.

WRF model does not simulate precipitation over the line of convergence during this episode. LCL and LFC are simulated around 500 and 900 m respectively, while the coastal front height is estimated around 400–500 m height. Moreover, the simulated values of CAPE are around 140 J kg^{-1} suggesting weak convection.

Figure 2.23 shows the potential temperature (color contours), the cloud mixing–ratio (black dashed lines), the equivalent potential temperature (black contour lines) and the wind field (arrows) at the vertical cross section along the line AA' shown in Fig. 2.4b at 23:00 UTC on 13 October 2010. Despite precipitation is not simulated, WRF model simulates clouds over the coastal front head as is indicated by the content of cloud mixing–ration, formed by the vertical motion of around 0.4 m s^{-1}. Over the head of coastal front, the equivalent temperature decreases, indicating weak instability.

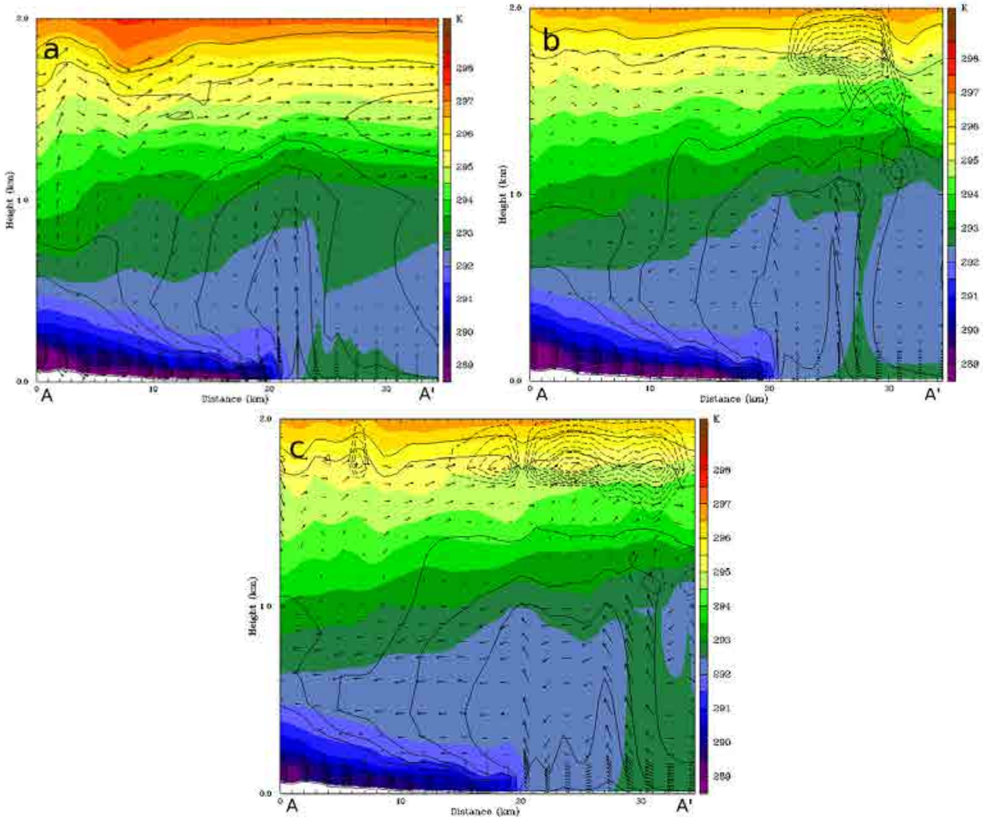

Figure 2.23: Simulated potential temperature (color contours), liquid water mixing–ratio (black dashed contour lines, maximum value 0.5 g kg^{-1}), the equivalent potential temperature (black solid contour lines) and wind field (arrows) along the line AA' shown in 2.23b at (a) 21:00, (b) 23:00 UTC on 13 October 2010 and (c) 01:00 UTC on 14 October 2010. The maximum horizontal wind speed is 4.4 m s^{-1}, and the maximum vertical wind speed is 0.4 m s^{-1}

As the night advances, the line of convergence moves offshore, as well as the clouds simulated over the cold air at the coastal front head.

2.5 Conclusions

Three coastal fronts characterized by a relatively large land–sea air thermal difference are simulated: the CF5, occurred on the eastern Mediterranean on 6 January 2011, CF8 occurred on the southwest of the Mediterranean basin (south of the Iberian Peninsula) on 3 March 2011 and CF10, on the northeast of the Iberian Peninsula on 13 October 2010. Note that these events occurred during winter (CF5 and CF8) and mid autumn (CF10), when inland air cools faster than sea–air, because the sea–surface temperature keeps relatively warm even during the night, and the inland air temperature decreases significatively.

The CF5 shows the larger land–sea air thermal difference, with around 8 K simulated at early morning on 6 January 2011; CF8 shows thermal differences around 9 K, and CF10 around 6 K. As a consequence of this thermal difference, drainage winds can develop and drive offshore the inland air mass, forming a well–marked offshore line of convergence. The simulations show a quasi–stationary line of convergence offshore in CF5 and CF8, which relatively large simulated drainage wind up to 7 m s^{-1}. Along this line of convergence, simulations show precipitation cells which form a quasi–stationary rainband.

Simulation of CF5 is in a good agreement with the cloud band recorded by Meteosat and precipitation estimated by TRMM at the time when this event occurred. The depth of the coastal front reach around 1000 m at early morning on 6 September 2011, when the simulated CAPE over the coastal front head reaches the maximum value of 867 J kg^{-1}, and the simulated LFC is at 600–800 m height at these times. Strong vertical motions are then simulated, with values around 1.1 m s^{-1}. Moisture and heat from the sea is transported vertically, and deep clouds develop with relatively heavy precipitation.

The precipitation simulated in CF8 is also in agreement with those recorded by the reflectivity radar images near the coast. However, the offshore western rainband simulated by the model does not appear in the radar images. The coastal front height reaches 700 m height at early morning, quite similar value than the simulated LFC over the coastal front head. At the coastal front head, precipitation cells form.

Referring to CF10, the model simulates a line of convergence that moves offshore quickly. However, the model does not reproduce any precipitation around the line of convergence, while the reflectivity radar images recorded weak precipitation offshore near the coastline. Weak instability is suggested from the simulated CAPE, which the maximum value is 140 J kg^{-1} over the coastal front head at early morning on 13 October 2010. At this time, the estimated coastal front height is 400 m, while the simulated LFC over the coastal front height is 900 m.

Chapter 3

The shape of the coastline

3.1 Introduction

This chapter[a] aims to analyze the role of the shape of the coastline on the offshore convergence, and coastal–front formation. Previous authors have claimed that the shape of the coastline plays an important role in enhancing onshore and offshore convergence at low levels. Concave coastlines favor the offshore convergence of nocturnal flows, while convex coastlines favor convergence onshore of sea breeze. High rainfall rates offshore during the night hours have been observed and analyzed in concave coastal areas worldwide (Neumann, 1951; Houze et al., 1981; Ohsawa et al., 2003; Yang and Slingo, 2001; Zuidema, 2003).

In order to analyze the role of the shape of the coastline, CF6 and CF1 are analyzed in this chapter. CF6 occurred in the eastern part of the Gulf of Sidra, in Libya; and CF1 occurred in the gulf of Genoa.

3.2 The quasi–stationary rainband on the gulf of Sidra: CF6

3.2.1 Observations

Figure 3.1 shows the area in the Mediterranean basin where this precipitation occurred. Precipitation over the Gulf of Sidra were recorded by TRMM satellite on the night of 30 January 2008.

---

[a] This chapter is based on Mazon, J and Pino, D: The role of sea–land air thermal difference, shape of the coastline and sea surface temperature in nocturnal offshore coinvection. Tellus **A** 2013, 65, 20027, http://dx.doi.org/10.3402/tellusa.v65i0.20027

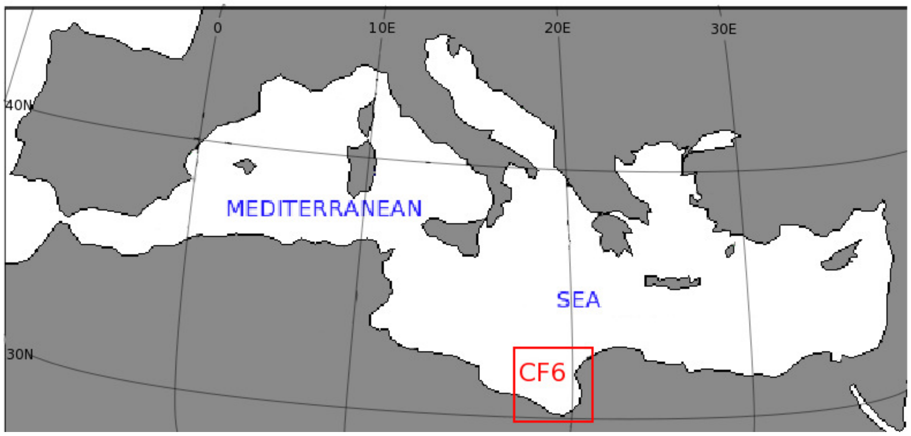

Figure 3.1: Location of the region (red square) in the Mediterranean basin where CF6 occurred.

Figure 3.2 shows the 3–h accumulated precipitation estimated by TRMM. Some precipitation cells formed along the coastline of Libya between 00:00 and 03:00 UTC (Fig. 3.2a) and disappeared at 06:00 UTC (Fig. 3.2b) on 30 January 2008. These cells formed a quasi–stationary line of precipitation very close and parallel to the coastline of the gulf of Sidra, in Libya. The maximum recorded 3-h accumulated precipitation was around 2 mm in the core of the three cells.

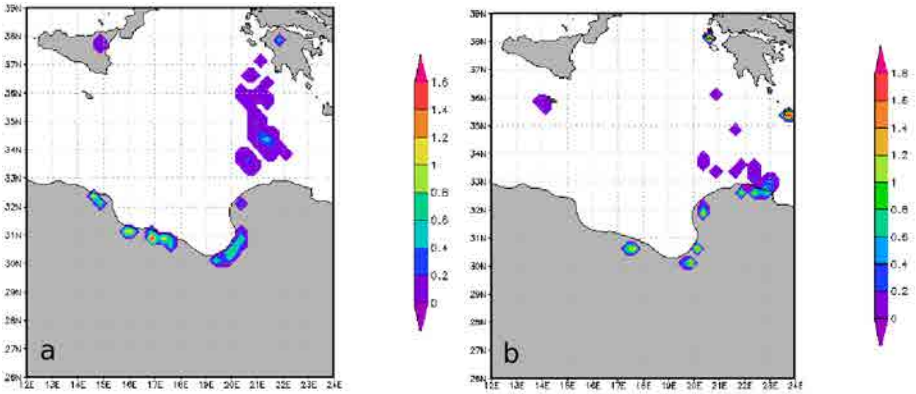

Figure 3.2: (a) 3–h accumulated precipitation estimated by TRMM between 00:00 and 03:00 UTC and (b) between 03:00–06:00 UTC on 30 January 2011

3.2.2 Synoptic analysis

The NCEP reanalysis on the 29 January 2008 at 00:00 UTC is shown in Fig. 3.3. Figure 3.3a shows the geopotential height at 500 hPa and the surface pressure on 30 January 2008 at 00:00 UTC. The high–pressure area over the central Mediterranean basin extended to the south. The isobar of 1030 hPa was located over the coastline of Libya. The low pressure area over Turkey moved to the northeast (not shown). Consequently, surface northerly winds prevails over Libya. Figure 3.3b shows the temperature field at 850 hPa at 00:00 UTC on 30 January 2008. A cold tongue from the north reached Egypt, having temperatures between −5 and 0°C. Moreover, a warm mass was located in central Mediterranean basin (5 to 10°C over Tunis). Between these two different air masses, there was a weak thermal gradient (0 to 5°C over Libya).

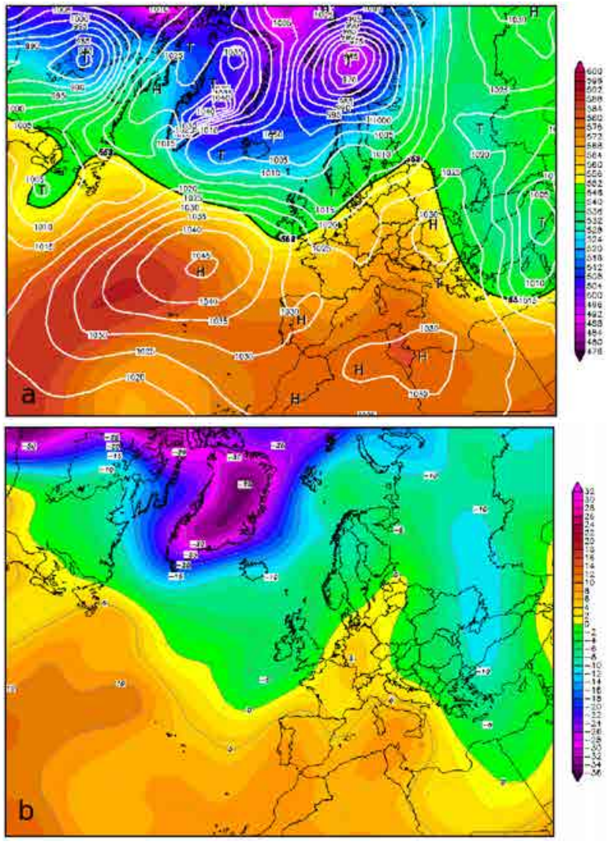

Figure 3.3: NCEP Reanalysis of (a) geopotential height in decameters at 500 hPa (color contours) and sea level pressure (white isolines) and (b) the temperature field (color contours) at 850 hPa on 30 January 2008 at 00:00 UTC.

3.2.3 WRF–ARW simulation

Three nested domains were defined with a horizontal grid space of 18, 6 and 2 km, having 125×110, 223×199 and 355×355 points, respectively. Figure 3.4 shows these nested domains (upper panel) and the smallest domain used (lower panel), which covers 710×710 km^2. The red and blue lines are the projection of the vertical cross sections used to analyze the role of the shape of the coastline. The simulation begins on 28 January 2008 at 00:00 UTC, and runs for 90 hours.

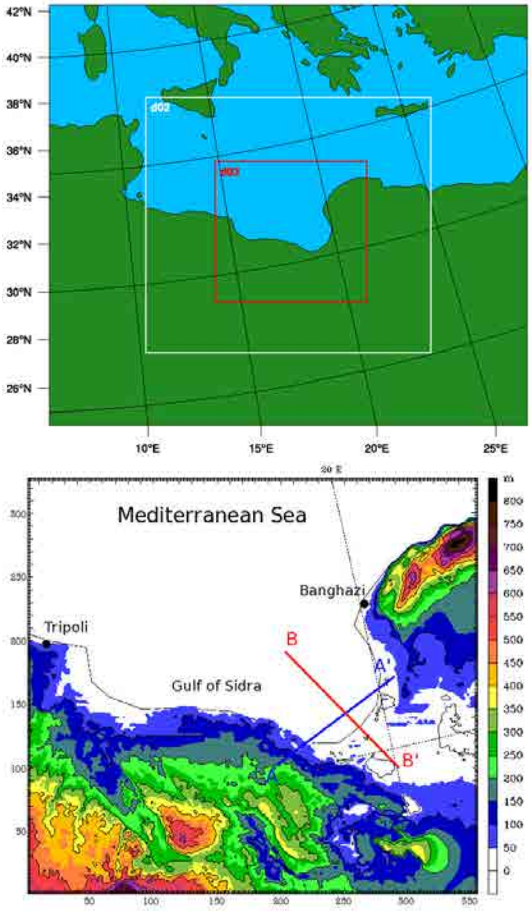

Figure 3.4: Nested domains (upper panel) and the orography in the smallest domain defined in WRF simulation (lower panel) on 30 January 2011. The red BB' and blue AA' lines are the projections of the vertical cross sections used to analyze the front.

Figure 3.5 shows the simulated 2–m potential temperature (color contours) and the wind field (arrows) at several hours during the night on 30 January 2008. At 00:00 UTC (Fig.

3.5a) the colder air mass is located inland. As the night advances, the sea–land air thermal difference increases. At 04:00 UTC (Fig. 3.5b) the inland cold air is located offshore near the coastline in a narrow strip, especially over the concave part of gulf of Sidra (following the line AA' indicated in Fig. 3.4). At 08:00 UTC (Fig. 3.5c) the cold air is located few kilometers offshore to the gulf.

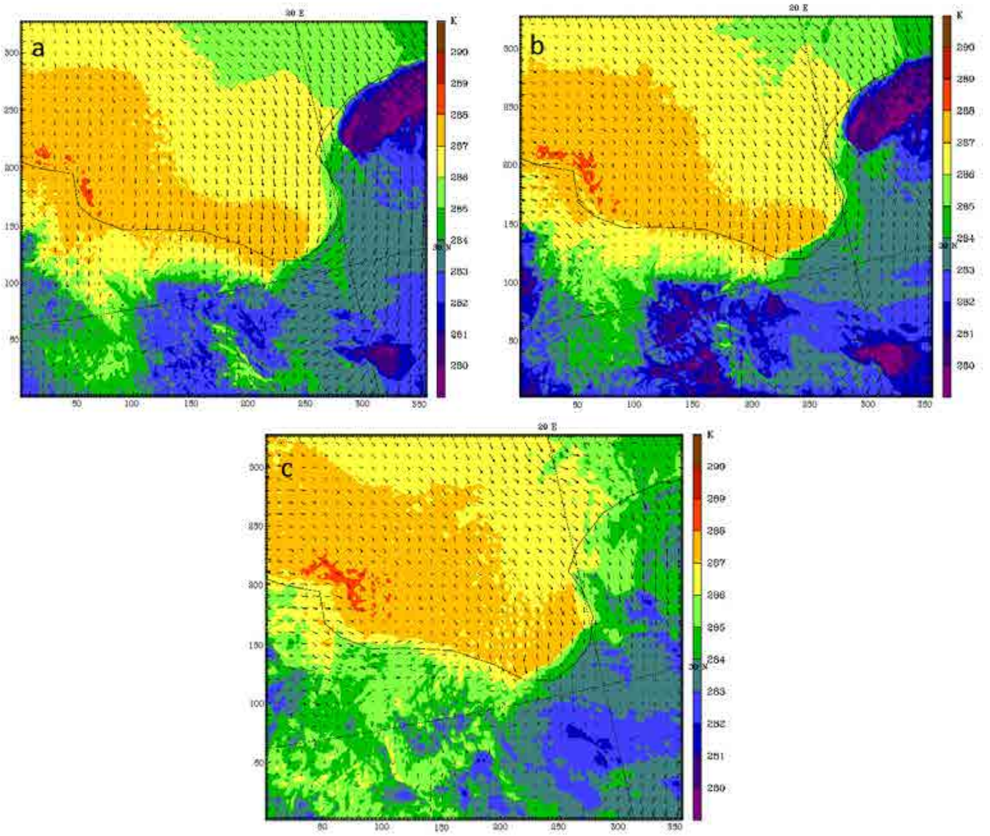

Figure 3.5: Simulated surface potential temperature (color contours) and surface wind field (arrows) on 30 January 2008 at (a) 00:00 UTC, (b) 04:00 UTC and (c) 08:00 UTC. The contour orography is plotted every 100 m.

Figure 3.6 shows the simulated surface divergence (color contours) and the wind field (arrows) in domain 3 at 04:00 and 08:00 UTC on 30 January 2008. At 04:00 UTC (Fig. 3.6a) a line of convergence follows approximately the coastline few kilometers offshore. This line of convergence becomes more continuos over the area indicated as AA' in Fig. 3.4, where the gulf exhibit their maximum curvature. At 08:00 UTC (Fig. 3.6b) this line of convergence remains approximately over the same location, while many lines of convergence are located offshore near the coastline in the rest of the domain.

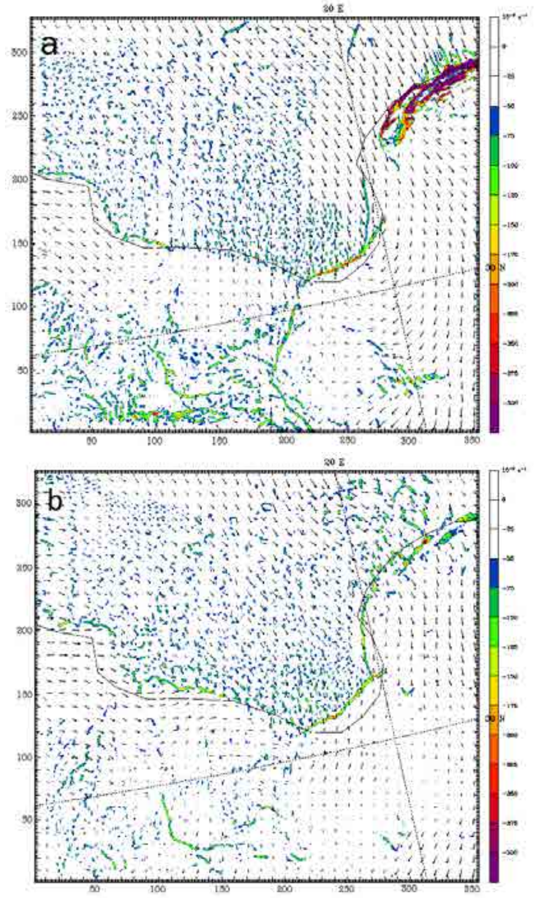

Figure 3.6: Simulated surface divergence (negative convergence, color contours) and wind field (arrows) on 30 January 2008 at (a) 04:00 UTC and (b) 08:00 UTC.

Figure 3.7 shows the simulated hourly accumulated precipitation (color contours) and the surface wind field (arrows) at 03:00, and 08:00 UTC on 30 January 2011. Several precipitation cells appear at 01:00 UTC and slowly move offshore forming an offshore line of precipitation near the coastline at 03:00 UTC (see Fig. 3.7a). This line of precipitation remains quasi–stationary until 08:00 UTC (Fig. 3.7b), when precipitation cells start to vanish. The simulated line of precipitation is located where the line of convergence is simulated in Fig. 3.6, approximately over the line AA' indicated in Fig. 3.4. The rainfall rate of the precipitation cells shown in Fig. 3.7 that form the rainband are lower than 1.5 mm h^{-1}, which is in a good agreement with the estimation of TRMM shown in Fig. 3.2. The location of the rainband are approximately the same, as well as the precipitation rate. Figure 3.7 also shows the opposite direction of the northerly synoptic flow and the southerly drainage winds in the area where the precipitation occurred.

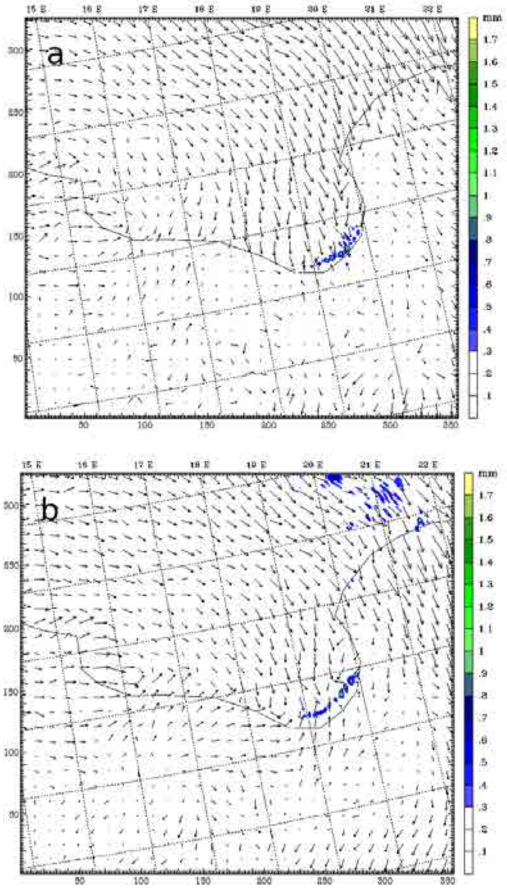

Figure 3.7: Simulated 1–h accumulated precipitation (color contours) and surface wind field (arrows) in the smallest domain at 03:00 UTC (a) and 08:00 UTC (b). The maximum wind speed is 11.3 m s^{-1} at 03:00 UTC and 12.1 m s^{-1} at 08:00 UTC.

Figure 3.8 shows the potential temperature (color contours), wind pattern (arrows) and equivalent potential temperature (contour lines) at several hours on 30 January at the vertical cross section along the line AA', defined in Fig. 3.4. The concave shape of the coastline plays an important role in enhancing convergence and upward movements. At 00:00 UTC, an inland cold air mass began to move slowly offshore from the oppossite east–west coastlines (see Fig. 3.8a). As the two opposing air masses approached, the convergence increased and the warm and wet Mediterranean air mass was forced upward (see Fig. 3.8b). Then vertical velocity increased to more than 1 m s^{-1} (maximum vertical velocity is 1.2 m s^{-1}), enough to overcome layers of stable atmosphere and reach LFC, located at around 800–1100 m from 01:00 to 07:00 UTC. Note that in this case the potential temperature decreased with height (a local, unstable layer appeared) but the equivalent potential temperature increased with height over the drained cold air. Consequently, a stable stratification prevailed producing weak convection. The potential temperature changed slightly with height, which indicates a low Brunt-Väisälä frequency. Consequently, weak vertical movements (waves over the cold air) were able to be formed. Few hours later, at 08:00 UTC, both cold masses joined and a cold layer formed over the sea (see Fig. 3.8c) producing a descending movement of the air masses and causing the precipitation cells to disappear. Over this cold air mass, the equivalent potential temperature increased with height, which denotes a stable stratification at low levels.

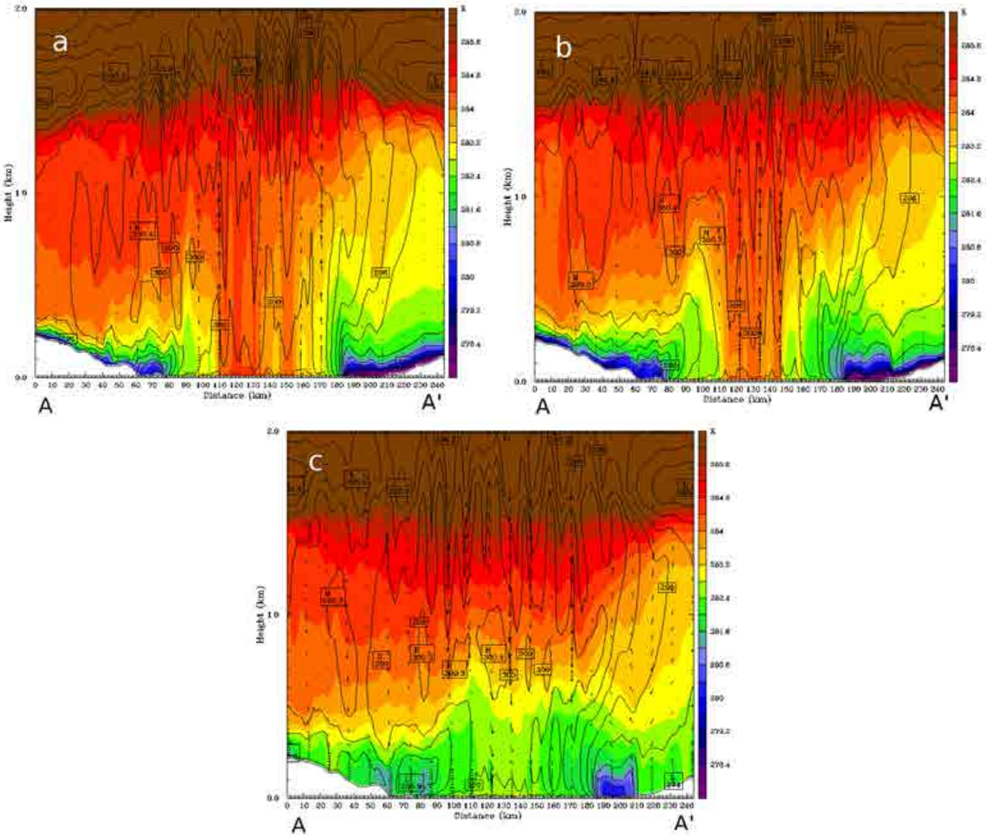

Figure 3.8: Vertical cross section defined along the blue line AA' shown in Fig. 3.4 of the simulated potential temperature (color contours), equivalent potential temperature (black contour lines) and the wind field (arrows) on 30 January 2008 at (a) 03:00 UTC, (b) 06:00 UTC and (c) 08:00 UTC. The maximum vertical velocity is 1.3 m s^{-1}.

In addition to the convergence of these air masses from opposite areas of the concave coast, many other drained cold air masses moved seaward, converging offshore with the northerly synoptic flow and/or with the other drainage winds that moved offshore from many other areas of the concave coastline (such as those shown in Fig. 3.8), enhancing the upward movements of the warm and wet air mass. As an example, the wind field and the potential temperature are shown in a vertical cross section along the line BB' defined in Fig. 3.4 on 30 January at 03:00, 06:00 and 08:00 UTC (see Fig. 3.9). The head of this cold air mass was stationary few kilometers offshore for several hours, at the approximately junction of lines AA' and BB', defined in Fig. 3.4. In this area, the convergence of cold air drained from the inland followed different directions, due to the concave shape of the coastline, and produced an upward transport of heat and moisture, enhancing the formation of convective cells.

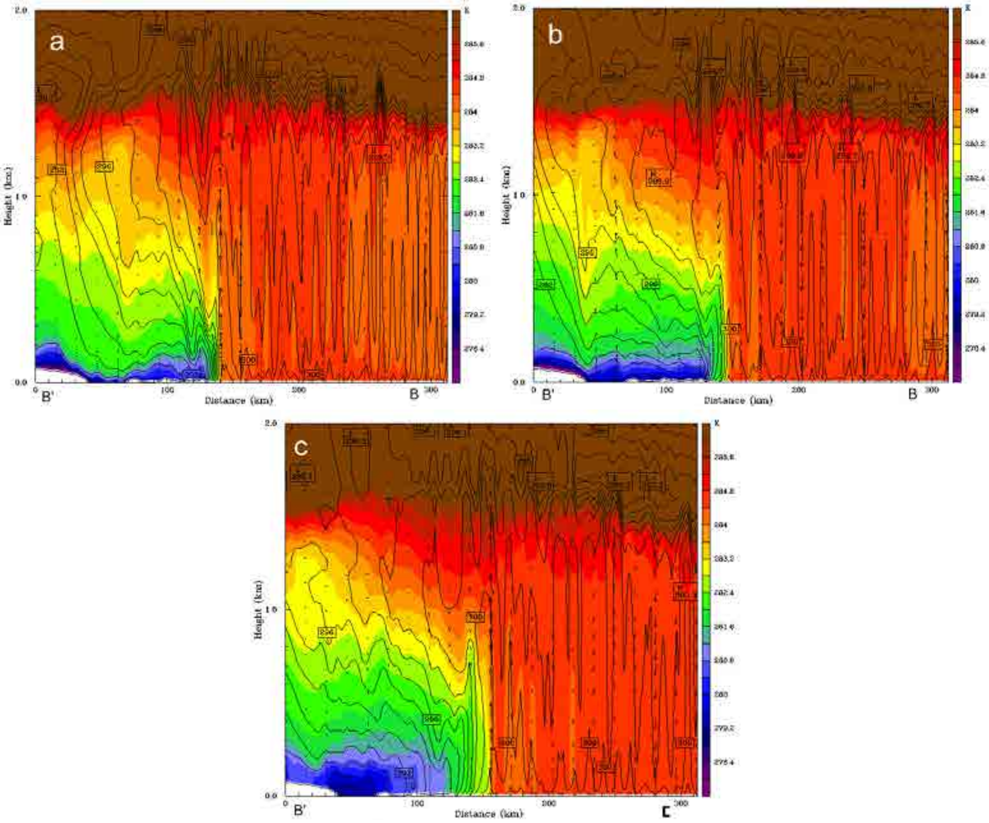

Figure 3.9: Vertical cross section defined along the red line BB' shown in Fig. 3.4 of the simulated potential temperature (color contours), equivalent potential temperature (black contour lines) and the wind field (arrows) on 30 January 2011 at (a) 03:00 UTC, (b) 06:00 UTC and (c) 08:00 UTC. The maximum vertical velocity is 1.3 m s^{-1}.

3.3 The rainband on the gulf of Genoa: CF1

3.3.1 Observations

TRMM multi–satellite measurements and estimations shows a precipitation area offshore the gulf of Genoa on 30 January 2008 between 03:00 and 06:00 UTC. Figure 3.10 shows the location within the Mediterranean basin where this precipitation occurred.

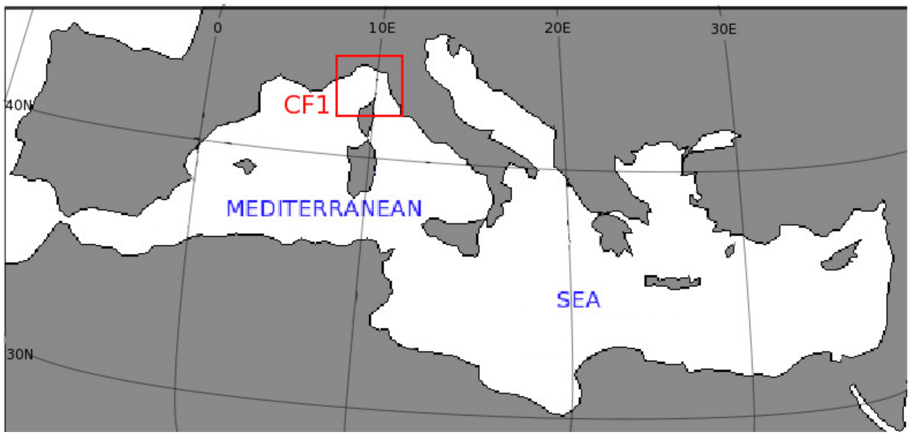

Figure 3.10: Location of the region where the CF1 occurred (red square).

Left panel of Fig. 3.11 shows the maximum 3–h accumulated precipitation estimated by TRMM between 00:00 and 03:00 UTC on 30 January 2008. Maximum values of 10 mm are recorded. The right panel of Fig. 3.11 shows the infrared image recorded at 02:32 UTC on 30 January 2008 by the satellite NOAA–18. Several clouds were recorded over the Gulf of Genoa.

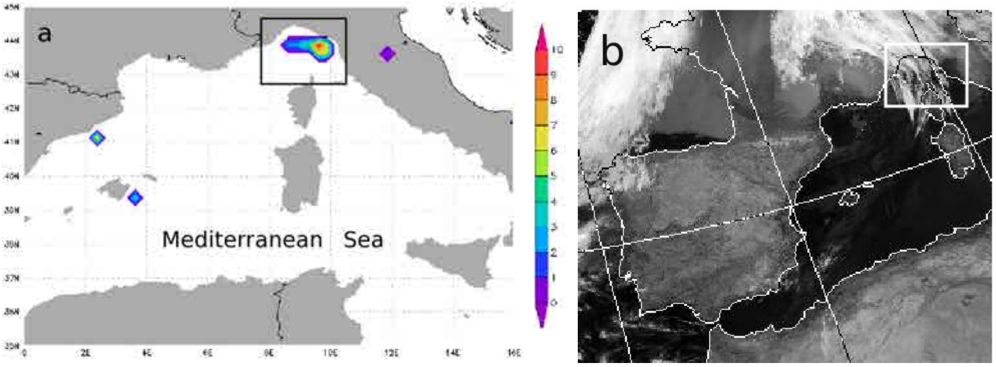

Figure 3.11: 3–h accumulated precipitation estimated by TRMM between 03:00 and 06:00 UTC (a) and data recorded from NOAA–18 in the thermal IR channel at 02:32 UTC on 30 January 2008 (b). The black and white rectangles indicate the approximate location of the smallest domain used in the WRF simulations.

3.3.2 Synoptic analysis

NCEP reanalysis shown in Fig. 3.3 two surface high–pressure areas are observed over North Africa (Tunis) and the Iberian Peninsula, with sea level pressure higher than 1030 hPa in each pressure center. A warm ridge from North Africa affected the center of the Mediterranean basin, advecting air over the Gulf of Genoa from the southwest. At 850 hPa (Fig. 3.3b), the west and centre of the Mediterranean basin was affected by a relatively warm air mass, between 5 and 10°C. No remarkable thermal gradients were observed over the gulf of Genoa.

3.3.3 WRF–ARW simulation

Three nested domains have been defined for simulation this event, with a horizontal grid space of 18, 6 and 2 km, having 40×40, 73×70 and 103×103 points, respectively. Figure 3.12a shows the location of these domains. Figure 3.12b shows the orography in the smallest domain, which covers the whole gulf of Genoa. The simulation begins at 00:00 on 28 January 2008 and finished at 18:00 UTC on 31 January 2008.

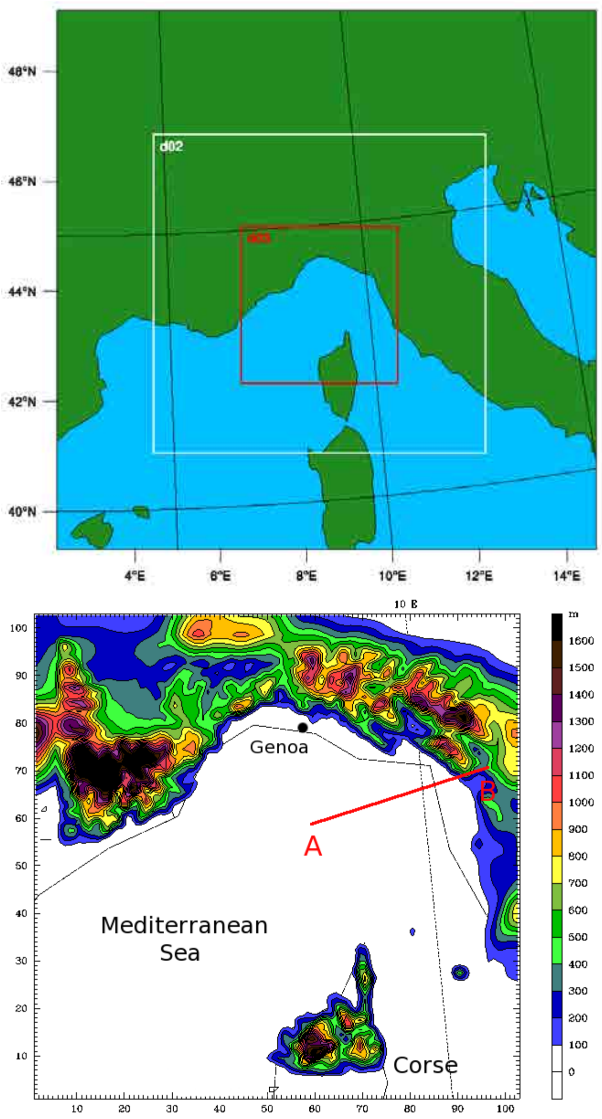

Figure 3.12: (a) Nested domains defined for the simulations; in (b) the orography in the smaller domain used for the analysis. The line AB indicates the direction of the vertical cross section used to analyze the front.

Figure 3.13 shows the potential temperature (color contours), wind pattern (arrows), the equivalent potential temperature (contour solid lines) and the cloud mixing ratio (contour dashed lines) at the vertical cross section along the line AB, defined in Fig. 3.12 at (a) 22:00 UTC on 29 January 2008, (b) 03:00 UTC and (c) 06:00 UTC on 30 January 2008. Driven by the drainage winds, the inland cold air moves offshore. Then, the maritime air is lifted over the cold mass. The head of the coastal front remain approximately at the same position, while the maritime air is lifting above. Vertical motions are simulated with a maximum vertical velocity of 0.9 m s^{-1} at 03:00 UTC. Over the coastal front head, clouds form. The simulated LFC is located around 300 and 550 m height from 22:00 UTC on 29 January 2008 to 08:00 UTC on 30 January 2008.

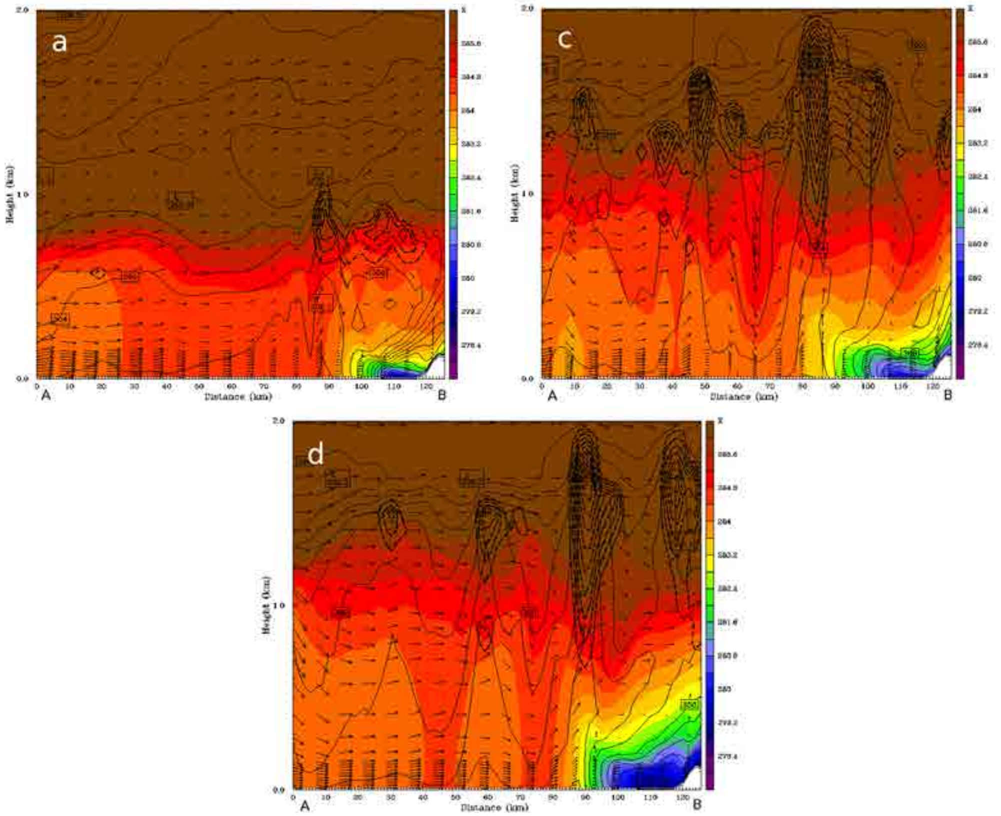

Figure 3.13: Vertical cross section defined along the red line AB shown in Fig. 3.12b of the simulated potential temperature (color contours), equivalent potential temperature (black solid contour lines), the wind field (arrows) and the cloud mixing ratio (black dashed contour) on 29 January 2008 at (a) 22:00 UTC, and on 30 January 2008 at (b) 03:00 UTC and (c) 06:00 UTC. The maximum vertical velocity is 1.3 m s^{-1}.

The role of the concave shape of the gulf can be noticed by analyzing the convergence field. Figure 3.14 shows the convergence field (color contours) and the surface wind field (arrows) in the smallest domain during the night from 29 to 30 January. At 22:00 UTC on 29 January 2008 (Fig. 3.14a) a line of convergence is simulated offshore following the the coastline along the Gulf of Genoa, formed by the interaction between the inland drainage air with the prevailing southeasterly maritime air. This line of convergence remains near the coastline during the whole night, shifting to the west part of the gulf. Figure 3.14b and c show the convergence and wind field at 02:00 and 06:00 UTC on 30 January 2008. The line of convergence is located the middle west part of the gulf. From 09:00 UTC, the simulated line of convergence disappears as did the inland drainage flow.

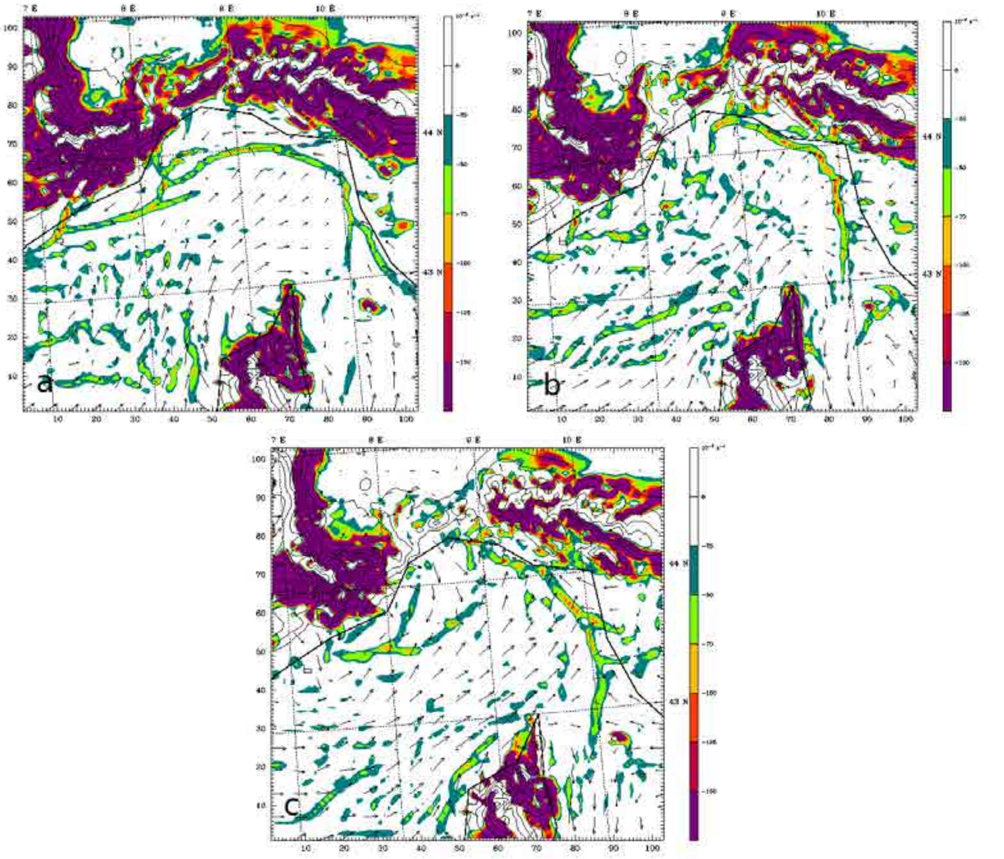

Figure 3.14: Simulated surface divergence (color contours) and wind field (vectors) at (a) 22:00 UTC on 29 January 2008 (maximum wind vector 8.1 m s^{-1}), (b) 02:00 UTC (maximum wind vector 8.8 m s^{-1}) and (c) 06:00 UTC (maximum wind vector 9.7 m s^{-1}) on 30 January 2008. The convergence scale is saturated in order to show better the offshore convergence bands. The orographic contours are plotted every 300 m.

Around the convergence zones, precipitation cells form. Figure 3.15 shows 1–h accumulated precipitation and the surface wind field at 00:00 and 06:00 UTC. At 00:00 UTC (see Fig. 3.15a), several precipitation cells along the coastline were simulated at the boundary between the drainage and the prevailing synoptic flows. During the night, these cells moved onshore, but new precipitation cells formed continuously over the convergence line as shown in Fig. 3.15b. From 09:00 UTC, the rain bands dissipated because the wind speed of the cold air mass decreased, while there was an increase in the parameter that accounts for the deceleration induced by the cool pool in the upstream flow. Weak convection is suggested according to the simulated values of CAPE, which take maximum value at early morning around 600 J kg^{-1}.

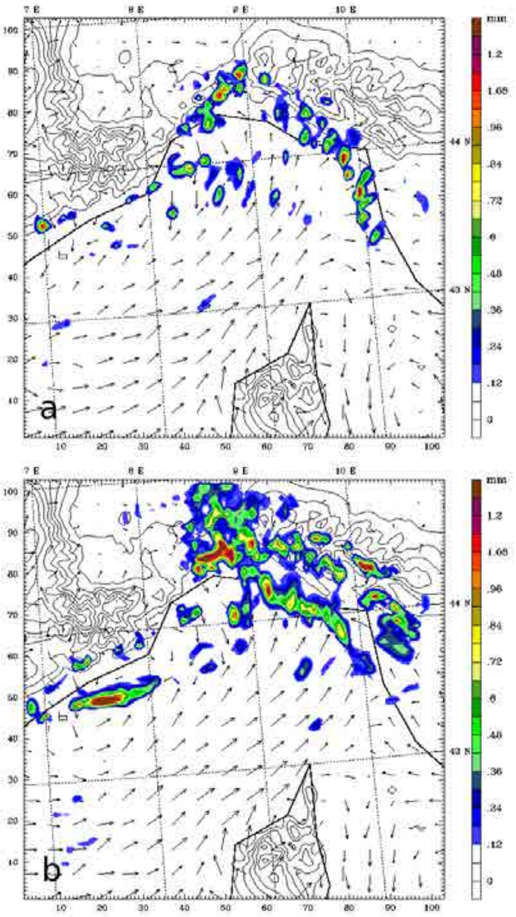

Figure 3.15: 1–h accumulated precipitation (color contours) and surface wind field (vectors) at (a) 00:00 UTC (maximum wind vector 8.7 m s^{-1}) and (b) 06:00 UTC (maximum wind vector 9.7 m s^{-1}) on 30 January 2008. The orographic contours are plotted every 300 m.

3.4 Conclusions

The role of the shape of the coastline has been analyzed in two CF: CF6 occurred over the gulf of Sidra, in the mid–south of the Mediterranean basin, and the CF1, occurred in the gulf of Genoa, in the northwest Mediterranean basin, both on 30 January 2008. The concave shape of the Gulf of Sidra and the gulf of Genoa play an important role in enhancing nocturnal convergence offshore during those events. Both numerical simulation results are in a good agreement with the location of the precipitation done by TRMM.

Concerning the CF on the gulf of Sidra, a rainband formed by several rain cells formed by offshore convergence near the coastline. This convergence is due to inland cold air led by drainage winds from many areas along the concave coastline in the extreme East part of the extreme Gulf of Sidra. Drainage winds flew offshore frontally from the opposite parts of the concave coastline, converging offshore. Additionally, drainage winds also converged frontally with the northern prevailing maritime flow. This convergence area transported heat and moisture upwards from the sea, at velocities that reach 1.2 m s^{-1}. The simulated equivalent potential temperature increased with height over the coastal front head, and consequently a stable stratification prevailed, producing weak convection. The simulated LFC was located at around 800–1100 meters between 01:00 and 07:00 UTC, the time when the CF develops. Weak precipitation is simulated by WRF, and estimated by TRMM.

Concerning to the event at the gulf of Genoa, a line of convergence is simulated following the coastline of this gulf, formed by drainage winds from many areas along the concave coastline. Around this line of convergence, several precipitation cells are simulated and remain quasi–stationary for several hours, mainly from 00:00 to 07:00 UTC on 30 January 2008. Over the coastal front head clouds form during these hours. The simulated LFC is located around 300 and 550 m height from 22:00 UTC on 29 January 2008 to 08:00 UTC on 30 January 2008. The maximum simulated vertical velocity is 0.9 m s^{-1} at 03:00 UTC, when the estimated coastal front height is 550 m and the simulated LFC over the coastal front head is around 600 m.

Chapter 4

Role of the Sea Surface Temperature

4.1 Introduction

Sea surface temperature (SST) and air temperature control moisture and heat fluxes. When a coastal front is formed over the sea, the depth of the cold air mass associated to this front (H) is directly proportional to the virtual potential temperature of the warm air mass (Simpson and Britter, 1980), in our case the maritime air mass. Consequently, the higher the temperature and moisture of sea–air (influenced by the values of the SST), the higher the sea–air virtual potential temperature. Consequently, H can grow reaching the LFC and deeper clouds can develop. In a previous work, Malda et al. (2007) concluded, by using mesoscale numerical experiments, that increasing SST enhances rainfall rates over the sea.

In the Mediterranean basin large values of SST are commonly recorded during late summer and autumn. Consequently, the air over the sea is much warmer and moister than the inland air during the night. A large land–sea air thermal difference enhances drainage winds, as it has been shown in previous chapters. This situation also may occur during the winter months.

Two are the main aims of this chapter[a]. The first one is to analyze two coastal fronts occurred at the end of the summer and early autumn, when the SST presents their larger values. These fronts are CF9, occurred at the western Mediterranean basin during the night on 6 September 2011, and the CF2, occurred on the middle of the Mediterranean basin on

---

[a] This chapter is partially based on Mazon, J. and Pino, D.: The role of sea–land air thermal difference, shape of the coasline and sea surface temperature in nocturnal offshore convection. Tellus **A** 2013, 65, 20027, http://dx.doi.org/10.3402/tellusa.v65i0.20027 and Mazon, J. and Pino, D: Mesoscale numerical simulations of heavy nocturnal rainbands associated with coastal fronts in the Mediterranean Basin. Nat. Hazards Earth Syst. Sci., **14** 1185–1194, 2014, doi: 10.5194/nhess–14–1185–2014

28 September 2008. These two events are analyzed in 4.2 and 4.3.

The second objective is to analyze the sensitivity of two relatively heavy nocturnal offshore rainbands to SST, the CF5 (in the western Mediterranean basin) and the CF9 (in the easter part of the basin). This has been done by performing two numerical experiments with the WRF–ARW model, including an increase on the SST in order to evaluate the sensitivity effect on the dynamics of the front and the precipitation pattern. This point is analyzed in Section 4.4.

It is important to note that the aim of this section is not to evaluate the influence of global warming in coastal front formation, but to analyze the sensitivity of nocturnal coastal front formation to an increase of the SST. However, this sensitivity analysis has a relevant importance since several climatic models predict a significant increase of the Mediterranean SST (Somot et al., 2008), which enhances evaporation, and consequently the amount of water vapor near the surface. Consequently, precipitation and clouds related to coastal fronts may be altered as a consequence of this increase of the SST. According to the report of the Fourth Assessment Report from the Intergovernmental Panel on Climate Change (IPCC), SST worldwide has increased an average of 0.7°C from the beginning of the 20^{th} century (Trenberth et al., 2007). In the west Mediterranean basin the SST has increased by approximately 0.6°C (Rixen et al., 2005; Vargas-Yáñez et al., 2008). This value is consistent with the regular measurements of SST 4 km offshore of the northeast coast of the Iberian Peninsula, where a clear increase in SST of around 0.7°C has been recorded over the last 30 years (Salat and Pascual, 2002, 2006). Moreover, at the end of the 21^{st} Century, a large increase in SST over the whole Mediterranean basin has been simulated with the Sea Atmosphere Mediterranean Model (SAAM) for all seasons (Somot et al., 2008). They evaluated the increase in SSTin the whole Mediterranean basin in the IPCC–A2 scenario by performing several SAAM numerical experiments over the 1960-2099 period. In the IPCC–A2 scenario, the SST anomalies found for the 30–year average in the period 2070–2099 as compared to the 1961–1990 control period are: between 2.5 and 3°C in the west Mediterranean region in summer (near the Iberian peninsula coastline, where CF9 occurred); and between 2 and 2.5°C in the east Mediterranean region during winter (where CF5 occurred).

The relation between the modification of SST and the consequent response to CAPE has been studied by several authors. According to Williams (1994), over the tropical Pacific area increasing 2°C the SST enhances the local evaporation to moisten the boundary layer which increases CAPE by 800 J Kg^{-1}. These authors show that the air temperature lapse rate hardly changes and has little contribution to CAPE change. Ye et al. (1998) investigated the response of CAPE to a warm SST over the Pacific by using Global Circulation Models. According to these authors, CAPE increases around 200 J Kg^{-1} in most regions over the Pacific ocean if SST increases 2 K, which suggests the environment of a warmer climate is slightly more unstable than that of the current climate. Regarding on convective clouds intensity, according to Ye et al. (1998), an increase of CAPE around 200 J Kg^{-1} would result in a 10%–15% increase in the updraft air parcel velocity. These authors also argue that assuming as an upper limit that CAPE increases due to an increase of the SST of 2 K is converted into kynetic energy, and consequently a 4 m s^{-1} increase in the cumulus updraft velocity.

4.2 The rainband on the western Mediterranean basin: CF9

4.2.1 Observations

A rainband was observed in the reflectivity radar images at the northeast of the Iberian Peninsula from 22:00 UTC from 5 September 2011 to the early morning on 6 September 2011. Figure 4.1 shows the location of the region in the Mediterranean basin where this CF occurred.

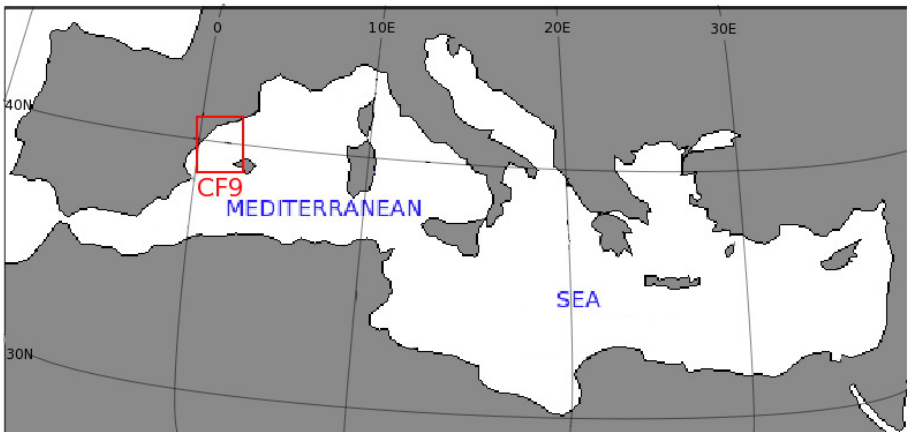

Figure 4.1: Location of the region where CF9 occurred (red square) within the Mediterranean basin.

Figure 4.2a shows the reflectivity radar image at 22:00 UTC on 5 September 2011. Several weak and isolate precipitation cells located parallel to the coastline were recorded. Figure 4.2b shows these cells forming a line of precipitation at 01:00 UTC on 6 September 2011. Figure 4.2c and d show the rainband moving offshore from 03:00 until 08:00 UTC. This line of precipitation extends around 150–200 km wide from 05:00 to 07:00 UTC on 6 September 2011.

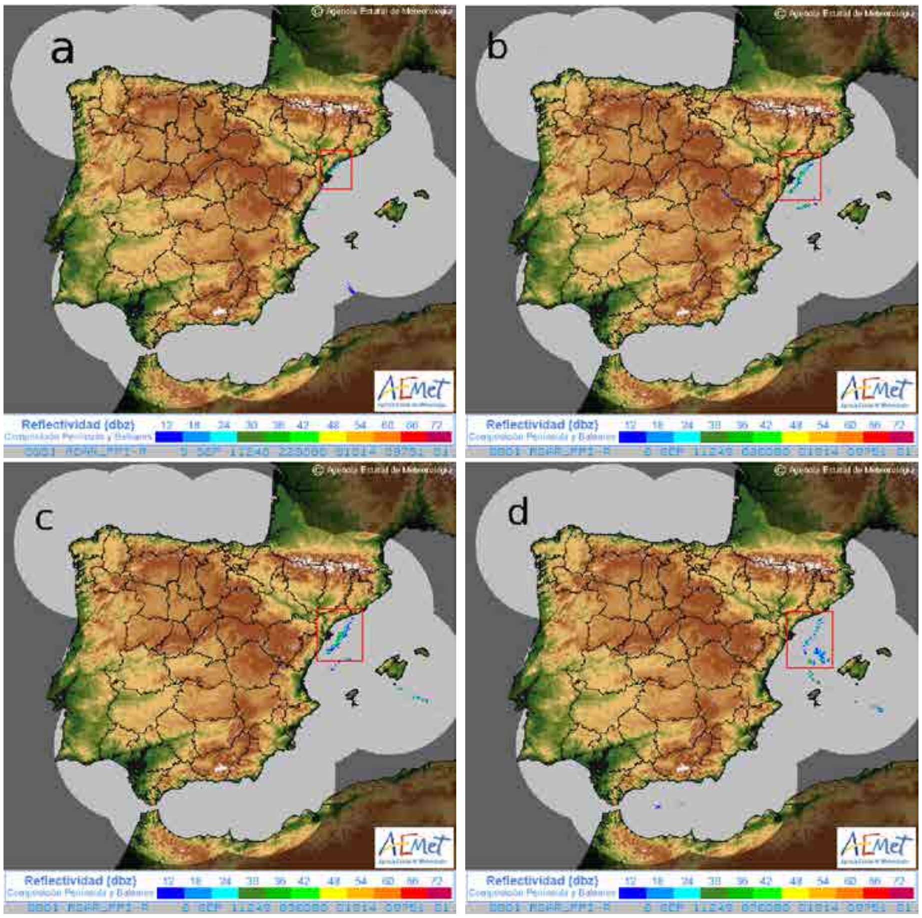

Figure 4.2: Reflectivity radar images recorded by the AEMET radar network at (a) 22:00 UTC on 5 September 2011, (b) 01:00 UTC, (c) 03:00 UTC and (d) 08:00 UTC on 6 September 2011. The red square indicates the location of the rainband associated with the CF analyzed in this section.

Clouds associated to this rainband was also recorded by satellite sensing. Figure 4.3a shows the thermal image recorded by Meteosat at 03:00 UTC, in which clouds area can be observed over the same area in which reflectivity radar recorded precipitation. Finally, Fig. 4.3b shows the 3–h accumulated precipitation estimated at 03:00 by TRMM, at approximately the same location in where the meteorological radar and Meteosat satellite recorded precipitation and clouds.

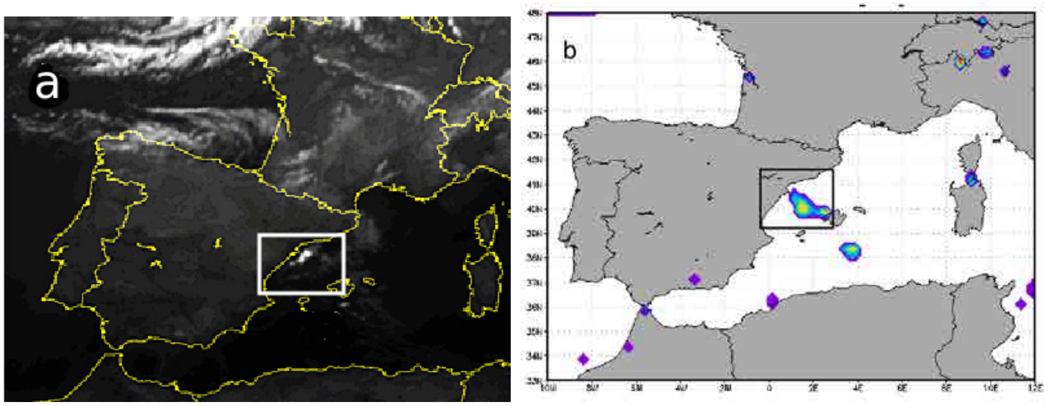

Figure 4.3: (a) Thermal IR channel of Meteosat satellite and (b) the 3–h accumulated precipitation estimated by TRMM at 03:00 UTC.

4.2.2 Synoptic analysis

Figure 4.4a shows the NCEP reanalysis of the geopotential height at 500 hPa and the surface pressure on 6 September 2011 at 00:00 UTC. A high–pressure area (1025 hPa) located over the Iberian Peninsula affects the entire western Mediterranean basin. Higher geopotential heights dominate the whole Mediterranean basin caused by a ridge from North Africa. Figure 4.4b shows the temperature at 850 hPa. A relative cold outbreak affected mainly the northeast of the Iberian peninsula, with a temperature of around 10°C.

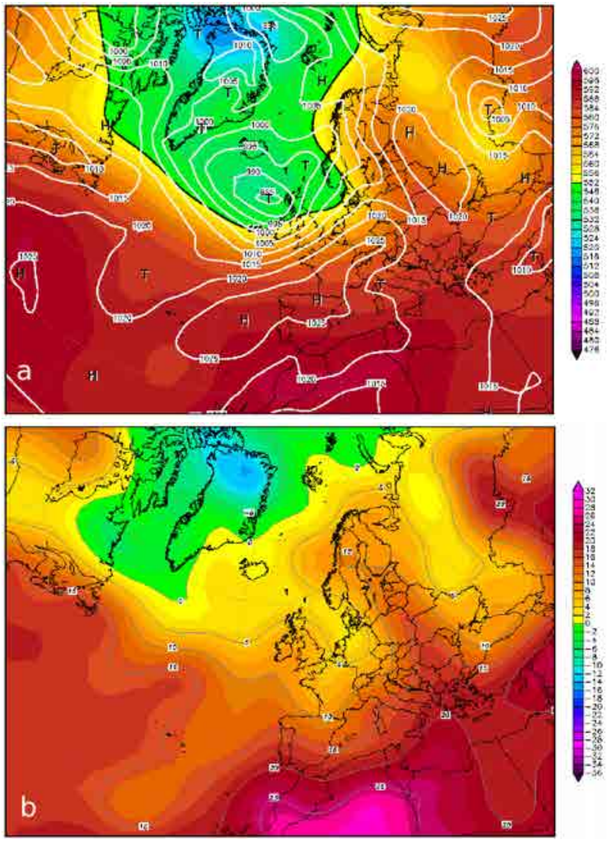

Figure 4.4: NCEP reanalysis of (a) geopotential height in decameters at 500 hPa (color contours) and sea level pressure (white isolines) and (b) temperature field (color contours) at 850 hPa on 6 September 2011 at 00:00 UTC.

4.2.3 WRF–ARW simulations

Three nested domains were defined with a horizontal grip space of 18, 6 and 2 km, having 80×80, 121×112 and 148×148 points. Figure 4.5 shows these nested domains (upper panel) and the orography of the smallest domain used (lower panel), which covers 296 × 296 km^2. The blue line AB indicates the projection of the vertical cross section used to analyze the front. The simulation begins at 00:00 UTC on 5 September 2011 and finishes at 18:00 UTC on 6 September 2011.

Figure 4.6 shows the simulated surface potential temperature (color contours) and the wind field (arrows) in domain 3 at 00:00, 02:00 and 06:00 UTC on 6 September 2011. At 00:00 UTC on 6 September 2011 (Fig. 4.6a) a cold inland outbreak is simulated along the coastline. The simulated surface potential temperature over the sea is around 297–298 K,

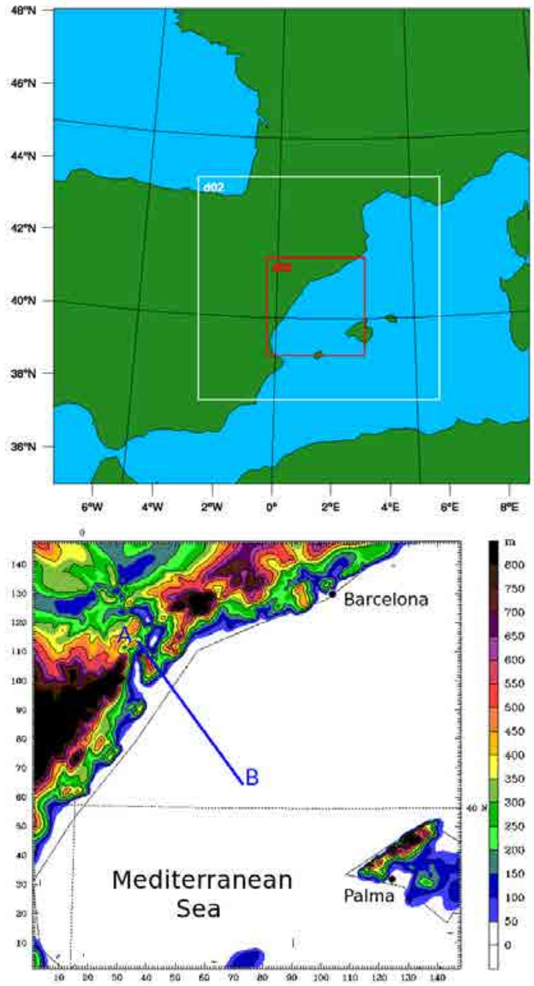

Figure 4.5: Nested domains defined (upper panel) and the orography of the smallest domain defined in WRF simulation (lower panel) on 6 September 2011. The blue line is the projection of the vertical cross section used to study the front.

while the inland surface potential temperature is about 293–294 K. At 03:00 UTC, Fig. 4.6b shows the inland cold air located offshore. Drainage winds drive offshore the inland cold air. At the edge of the inland cold outbreak, drainage winds veers to southerly when interacts with the prevailing easterlies, which drive warm and wet air mass. At 06:00 UTC (Fig. 4.6c) shows the inland cold air mass located around 100 km offshore.

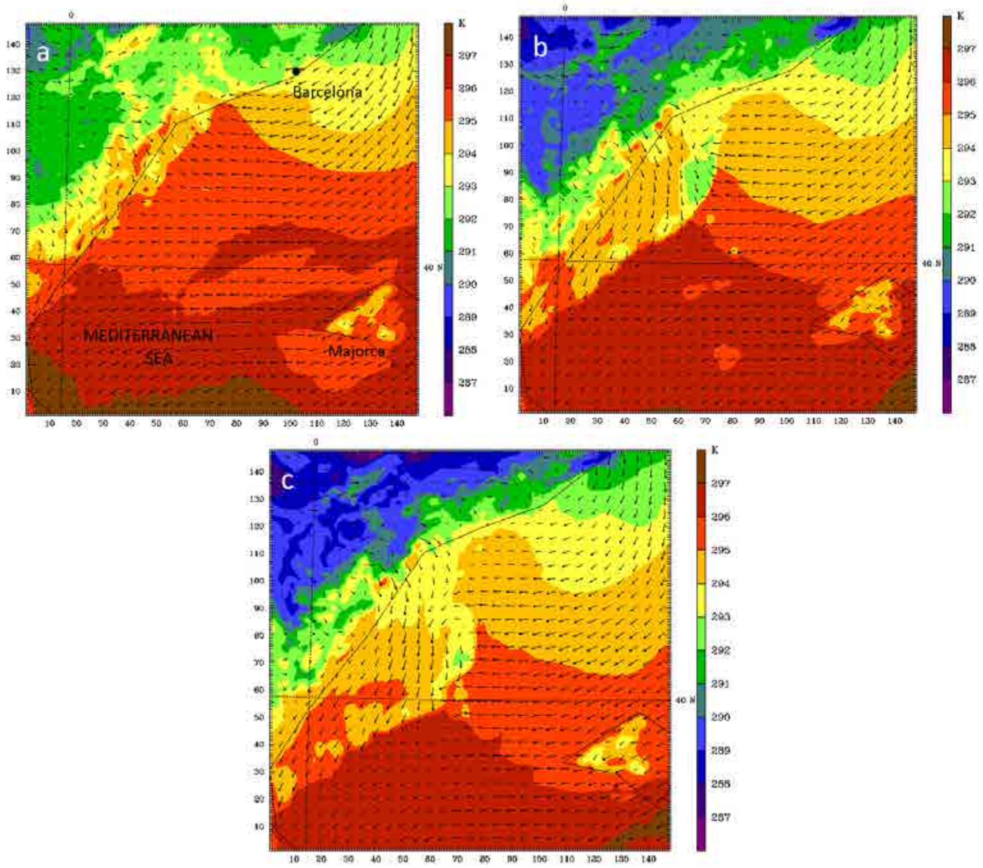

Figure 4.6: Simulated surface potential temperature (color contours) and wind field (arrows) in the smallest domain at (a) 00:00 UTC, (b) 03:00 UTC and (c) 06:00 UTC on 6 January 2011.

The cold inland air driven by drainage winds form a coastal front when interact offshore with the warmer sea–air. Figures 4.7a–c show the simulated surface divergence (color contours) and the wind field (arrows) in domain 3 at 00:00, 03:00 and 08:00 UTC on 6 January 2011, respectively. Regarding the convergence field offshore (onshore convergence is caused by the interaction with the orography) at 00:00 (Fig. 4.7a) several, concave and thin lines of convergence are simulated close to the coastline where a change in the wind field is noticed. These lines of convergence move offshore with time, driven by the drainage winds, joining and forming a larger offshore line of convergence running parallel to the coastline (see Fig. 4.7b). The change in wind direction at the line of convergence is well noticed as the night advances. Behind the line, the drainage wind is northerly while in front of the line the prevailing wind is southeasterly. At 08:00 UTC the line of convergence is located around 100 km offshore. The convergence line vanishes at 08:00 UTC.

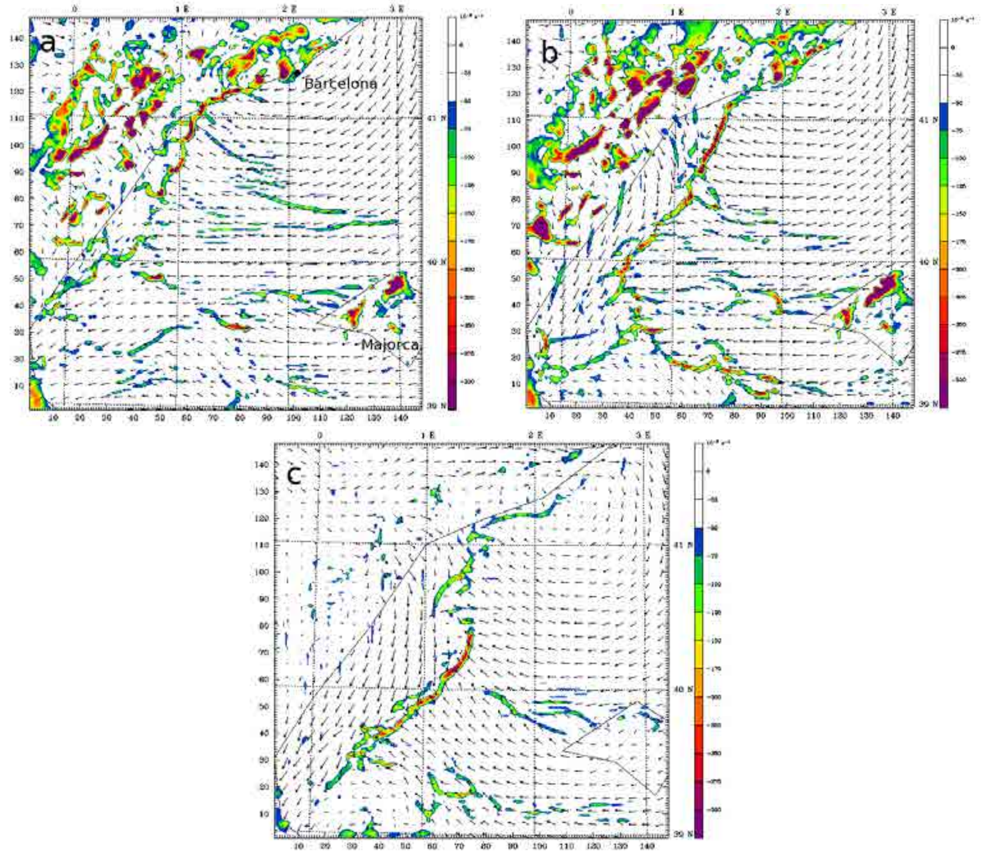

Figure 4.7: Simulated surface divergence (negative convergence, color contours) and wind field (arrows) in the smallest domain at (a) 00:00 UTC, (b) 03:00 UTC and (c) 08:00 UTC on 6 September 2011.

Around the line of convergence a line of precipitation is also simulated in quite good agreement with the reflectivity radar images shown in Figs 4.2b-d. Figure 4.8 shows, in the smallest domain of the simulation, the 1–h accumulated precipitation (color contours) and the surface wind field (arrows) at (a) 19:00 and (b) 22:00 UTC on 5 September 2011, (c) 03:00 and (d) 06:00 UTC on 6 September 2011. At 19:00 UTC (Fig. 4.8a), easterly flow prevails over the coastline but there is no drainage winds. From 19:00 UTC, a cold air flow moving from land to sea appears. At 22:00 UTC (Fig. 4.8b) some precipitation cells form, which join to produce a line of precipitation moving offshore due to the drainage winds (see Figs. 4.8c, d). The precipitation rate is around 20 mm h^{-1} in some parts of the line. The simulated CAPE over the line of convergence shows values between 1400 and 1500 J kg^{-1} between 01:00 UTC and 04:00 UTC, reaching maximum values at 06:00 UTC with 1590 J kg^{-1}, which indicates moderate convection. At 06:00 UTC (Fig. 4.8c) the simulation shows an arc of precipitation of around 150 km, formed by several intense convective cells. Behind the arc, the cold air mass flow veered northwest while an easterly flow prevailed ahead of the arc. From 06:00 UTC the precipitation associated to the coastal front tends to disappear due to the decrease of the propagation speed of the cold air associated to the front.

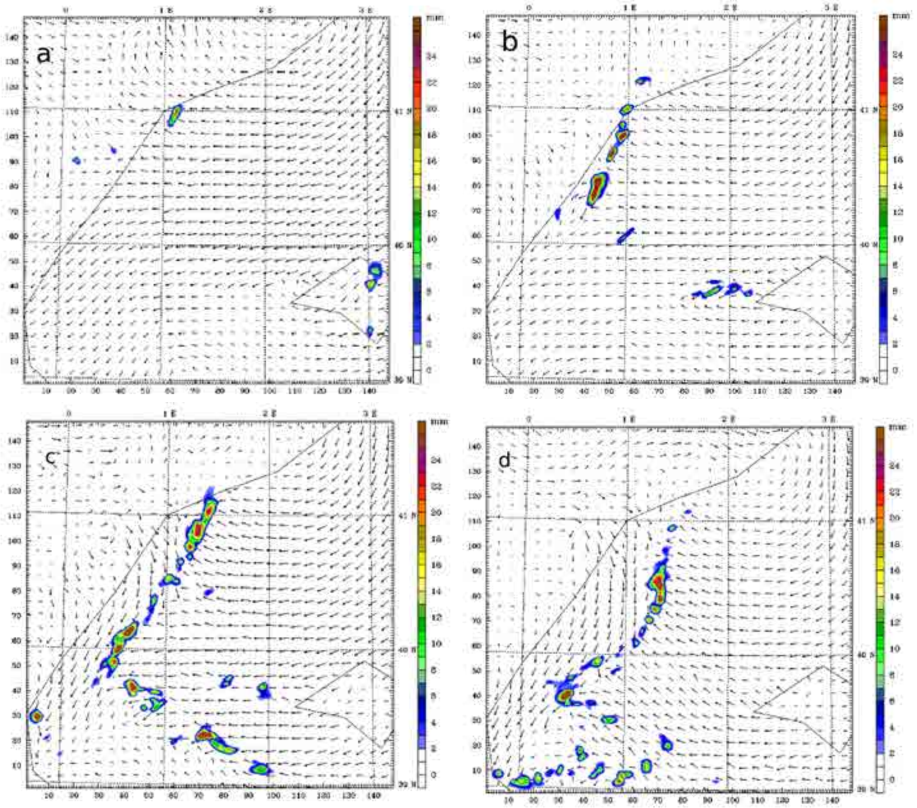

Figure 4.8: Simulated 1–h accumulated precipitation (color contours) and surface wind field (arrows) at (a) 19:00 UTC and (b) 22:00 UTC on 5 September 2011 at (c) 03:00 and (d) 06:00 UTC on 6 September 2011. Maximum wind speed is 10.6 m s^{-1}, 9.8 m s^{-1}, 9.7 m s^{-1} and 8.6 m s^{-1} in (a), (b), (c), and (d), respectively.

Figure 4.9 shows the vertical cross section along the blue line A–B shown in Fig. 4.5 of the potential temperature (color contours), wind field (arrows) and the total cloud mixing–ratio (contour lines) at 22:00 UTC on 5 September 2011, 00:00, 03:00, 06:00 and 08:00 UTC on 6 September 2011. At 22:00 UTC (Fig. 4.9a), the inland cold air mass with a surface potential temperature around 293–294 K is simulated descending the mountains near the coastline, and reaching the sea. At the edge of this cold air, vertical motions of the warmer sea–air (with a surface temperature around 296–297 K) are simulated. Some clouds are formed as it is indicated by the simulated cloud mixing ratio. Driven by the drainage winds, the inland cold air mass move offshore (Fig. 4.9b–e), as well as the cloud formed over the front. The simulated vertical velocity reaches maximum values of around 1.2 m s^{-1}, which enhanced vertical motion of moisture and heat from the sea–air. Simulated clouds above the cold front have their base at 800 m, and their top at 3000 m.

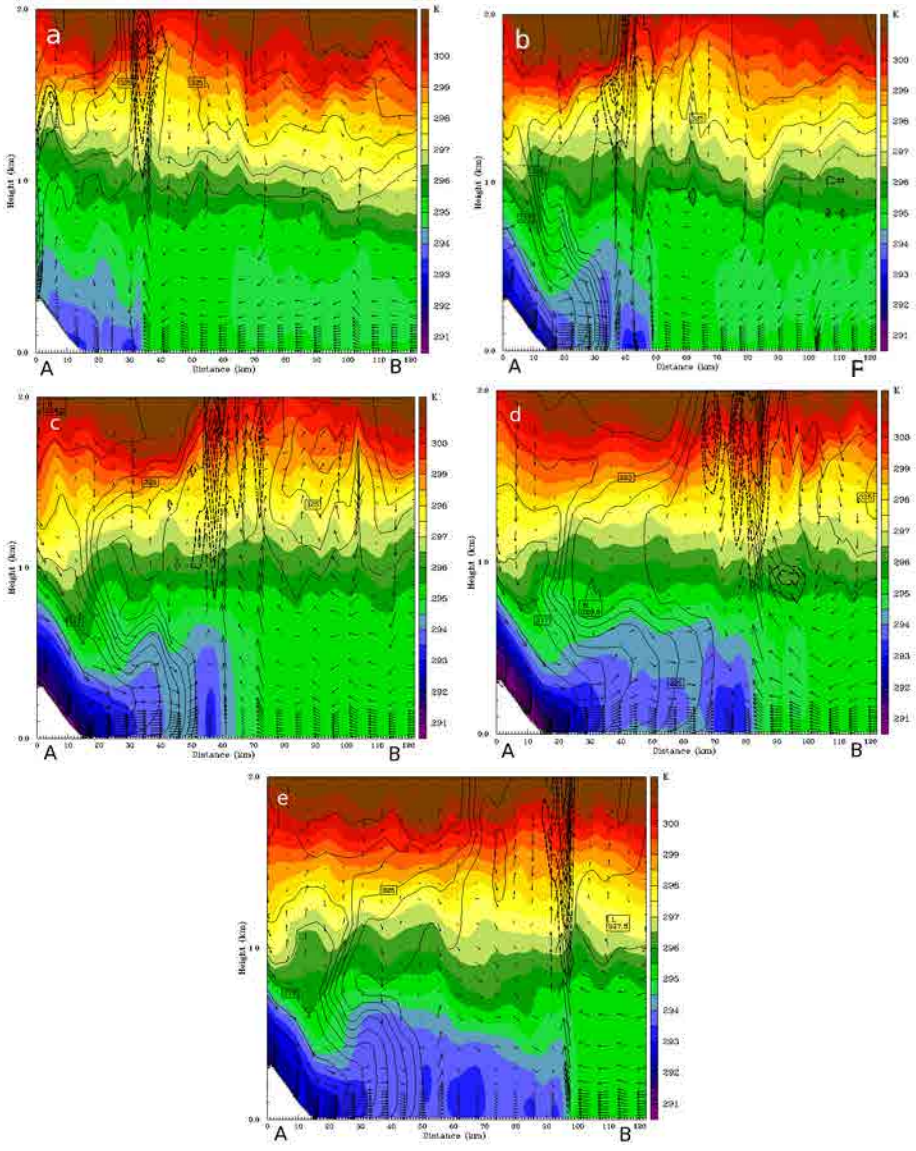

Figure 4.9: Vertical cross section of the simulated potential temperature (color contours), liquid water mixing–ratio (black contours lines, maximum value 5 g kg^{-1}) and wind field (arrows) along the line A–B shown in Fig. 4.5 at (a) 22:00 UTC on 5 September 2011, (b) 00:00 UTC, (c) 03:00 UTC, (d) 06:00 UTC and (e) 08:00 UTC on 6 September 2011. The maximum horizontal wind speed is 11.3 m s^{-1}, and the maximum vertical wind speed is 1.2 m s^{-1}.

This nocturnal coastal front, CF9, as well as the CF10 analyzed in chapter 2 occurred at different temporal and spatial scales over the same area, the western Mediterranean basin. Considering the estimated time life and horizontal scales of these CFs are, they can be included into the meso–β and meso–γ scales defined by Orlanski (1975), respectively. Based on the frontogenesis over the western Mediterranean basin at these scales, in Appendix A a discussion about the character of the western Mediterranean basin as a frontogenesis zone at the whole mesoscale is argued, by adding a new simulation of a coastal front occurred at the meso–α scale on 25 and 26 August 2012 over the west Mediterranean basin. The estimated time life, horizontal and vertical scales of each of these three CFs at the correspondent mesoscale are shown in Appendix A.

4.3 Precipitation cells around the central Mediterranean basin: CF2

4.3.1 Observations

Many precipitation cells formed around the Italian peninsula during the night of 28 September 2004. Figure 4.10 shows the location of the region where one of these precipitation areas occurred, CF2.

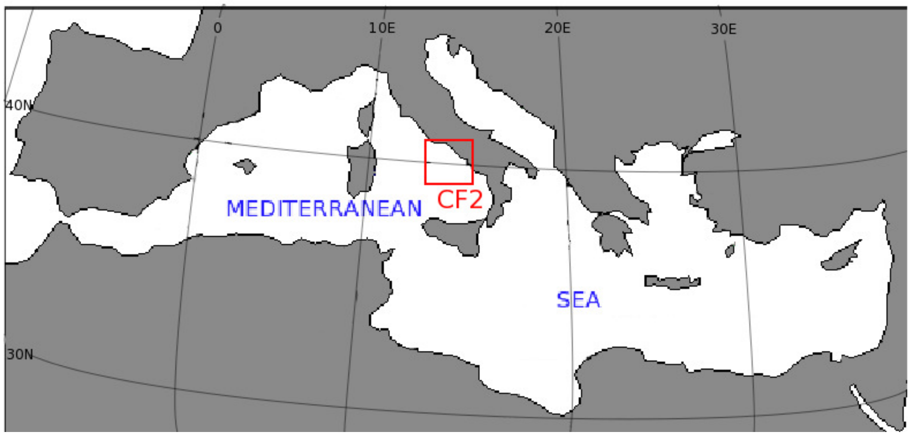

Figure 4.10: Location (red square) of the region where CF2 occurred.

According to the TRMM database (see Fig. 4.11), on the night of 28 September 2004, many offshore weak precipitation cells formed between 00:00 and 06:00 UTC surround the Italian peninsula: around the Tyrrhenian Sea, the Mediterranean Sea, in the Adriatic coast and in the central area of the Adriatic sea.

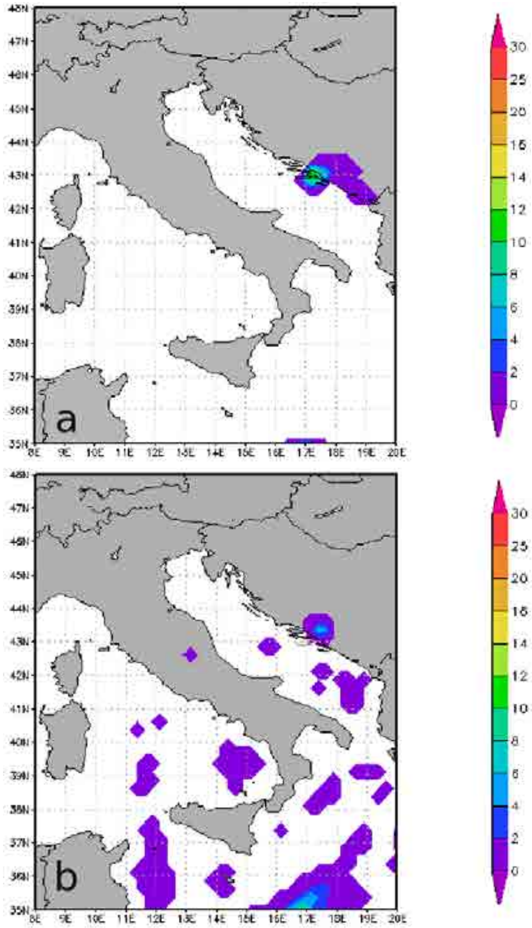

Figure 4.11: 3–h accumulated precipitation estimated by TRMM at (a) 00:00 and (b) 03:00 UTC on 28 September 2004.

4.3.2 Synoptic analysis

Figure 4.12a shows the NCEP reanalysis at 500 hPa and surface pressure on 28 September 2004. At 500 hPa, low values of the geopotential height over the mid Mediterranean basin is observed. At sea–level, a small relative low–pressure area was located over the Ionian Sea. But pressures around 1020 hPa in the center of the Italian peninsula are observed in the reanalysis. Surrounding the middle Mediterranean basin, relative high-pressure areas defined the atmosphere (1025 hPa and 1020 hPa in both western and eastern Mediterranean basin). At 850 hPa (Fig. 4.12b a relatively cold air from northern Europe affected the central Mediterranean basin, with temperature between 5 and 10°C. At sea–level, a weak northeasterly flow is observed.

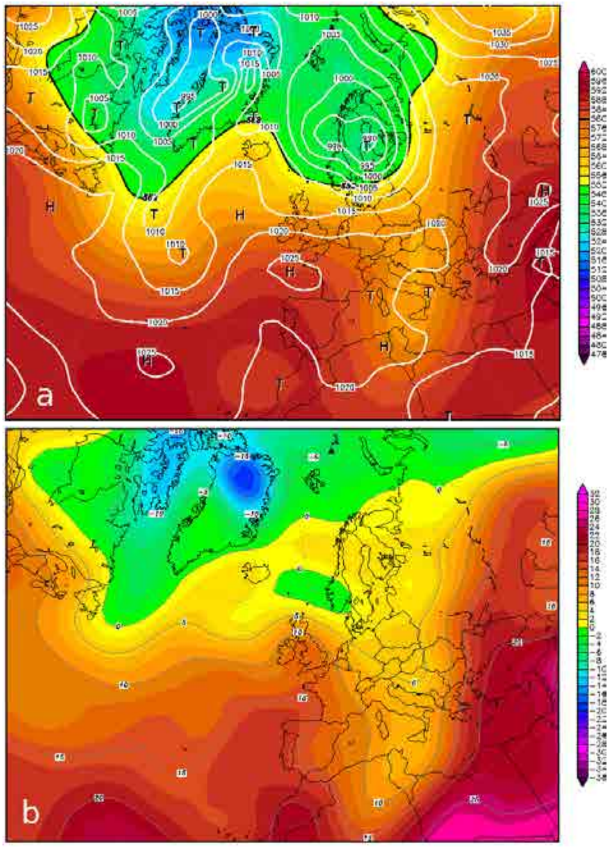

Figure 4.12: NCEP Reanalysis of (a) geopotential height in decameters at 500 hPa (color contours) and sea level pressure (white isolines) and (b) the temperature field (color contours) at 850 hPa on 28 September 2004 at 00:00 UTC.

4.3.3 WRF–ARW simulation

As many small precipitation cells were observed by TRMM around the Italian peninsula, a single domain has been defined to simulate this event. Figure 4.13 shows this single domain defined in the WRF simulation, which covers the whole Italian peninsula, having 1200×1200 km^2. The grid spacing is 3×3 km^2, with 400×400 points. The simulation was initialized at 12 UTC on 26 September, more than 12 hours prior to the event, and it ends at 18 UTC on 27 September.

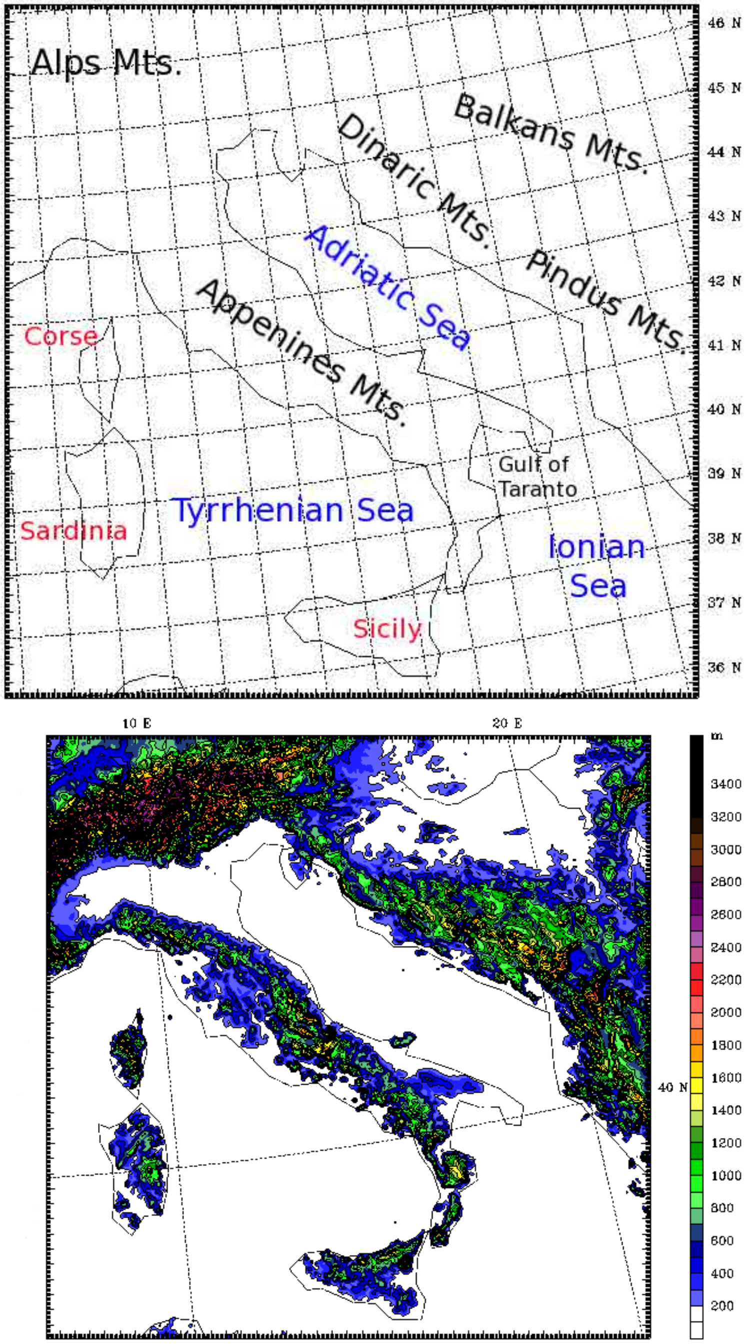

Figure 4.13: WRF domain defined for the 28 September 2004 event and the main geographical features (upper panel) and the topography (lower panel).

Figure 4.14 shows the simulated surface potential temperature (color contours) and wind field (arrows) at 22:00 UTC on 27 September 2004, 00:00, 03:00 and 06:00 UTC on 28 September 2004. At 22:00 UTC on 27 September 2004 (Fig. 4.14a) cold inland air moved offshore driven by drainage winds in many areas around the Italian peninsula. The simulated sea–air temperature is around 295 K over the Ionian Sea, around 291 K in the Adriatic Sea and around 293 K on the Tyrrhenian Sea, while the inland surface temperature is around 287 K in the north of the Italian peninsula, and 289–290 K in the south. The land–sea thermal gradient around the Italian peninsula enhances movements of inland air offshore, as is shown in Figs. 4.14b–d.

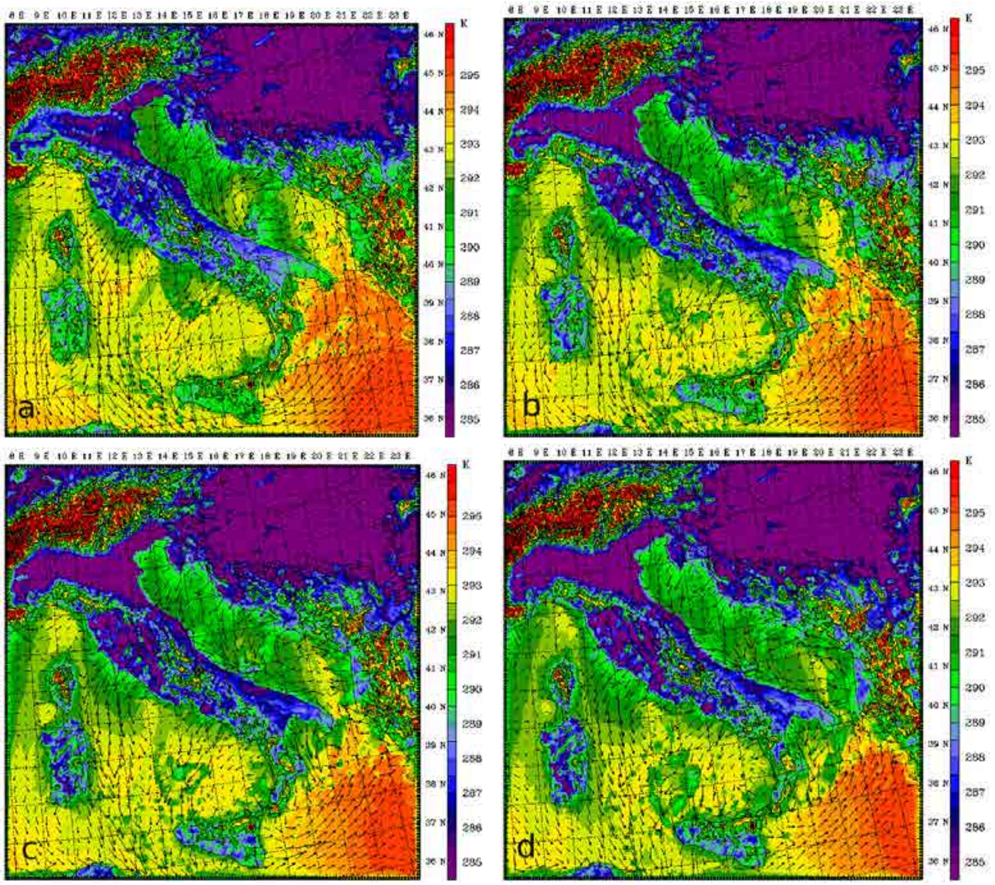

Figure 4.14: Simulated surface potential temperature (color contours) and surface wind field (arrows) in the smallest domain at (a) 22:00 UTC on 27 September 2004, (b) 00:00 UTC, (c) 03:00 UTC and (d) 06:00 UTC on 28 September 2004. The maximum wind speed is 9.5 m s^{-1}, 10.6 m s^{-1}, 11.1 m s^{-1} and 12.1 m s^{-1} respectively. The scale is saturated in some inland areas in order to show better the cold outbreaks offshore. The orographic contours are plotted every 400 m.

Figure 4.15 shows the surface air divergence (color contours) and the wind field (arrows) at 22:00 UTC on 27 September 2004 and 03:00, 06:00 and 08:00 UTC on 28 September 2004. Several offshore lines of convergence are simulated around the coastlines, formed by the interaction between the inland cold air mass (driven by the drainage winds) with the warmer sea air mass. At 22:00 UTC on 27 September 2004 (Fig. 4.15a) two significant lines of convergence are simulated offshore over the Tyrrhenian Sea near the coastline of the Italian peninsula. Over the Adriatic Sea, a line of convergence is also simulated very close to the Italian coastline, which remains stationary from 03:00 until 08:00 UTC on 28 September 2004 (Fig. 4.15b, c and d). At 03:00 UTC on 28 September (Fig. 4.15b) the simulation shows over the Tyrrhenian Sea many irregular shape areas of convergence. At 06:00 UTC (Fig. 4.15b), an arc of convergence is simulated over the south coast of the Italian peninsula on the Tyrrhenian Sea. Over the Adriatic Sea, the line of convergence near the Italian coast is located offshore, and new lines of convergence appear on the South of the Italian peninsula, offshore over the Ionian Sea. All these lines of convergence are also simulated at 08:00 UTC (Fig. 4.15d).

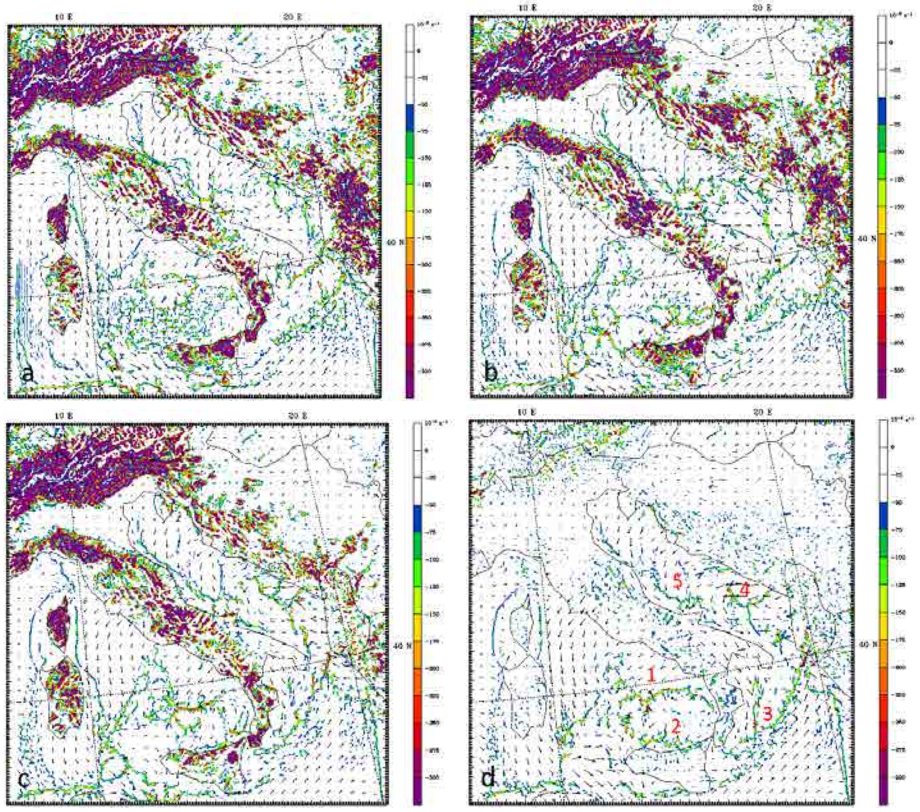

Figure 4.15: Simulated surface divergence (negative convergence, in contour colors) and wind field (arrows) at (a) 22:00 UTC on 27 September 2004, (b) 03:00, (c) 06:00 UTC and (d) 08:00 UTC on 28 September 2004. The numbers in (d) indicate the lines of convergence associated with precipitation.

These lines of convergence suggest that coastal fronts are formed, and consequently warmer sea–air is lifted over the cold drained air mass. Precipitation cells occur over these lines of convergence, especially from 03:00 UTC on 28 September. Figure 4.16 shows the simulated 1–h accumulated precipitation pattern (color contours) and the surface wind field (arrows) at 03:00 and 08:00 UTC. Different precipitation areas appear in the simulation. The first one is located in the Tyrrhenian Sea off the coastlines of the Italian peninsula and Sicily (indicated as 1 in Fig. 4.16a). Strong drainage winds (around 11 m s^{-1}) blow from northwestern Italian coast into the Tyrrhenian Sea, leading the inland cold air offshore forming a coastal front, with a cold depth of around 500–700 m height between 04:00 and 08:00 UTC. At this time the simulated LFC over the front is around 700 m. Weak values of CAPE are simulated by WRF, with maximum values around 400 J kg $^{-1}$ at 06:00 UTC. Around one hundred kilometers offshore, the drainage winds deflects to the south, probably forced by the drainage winds coming from Corsica and Sardinia. These drainage winds interact with the drainage winds coming from the Southern part of the Italian Peninsula, enhancing convection.

The second area of precipitation indicated as 2 in Fig. 4.16a appears at the north coast of Sicily. Drainage winds from north Sicily converge frontally a few kilometers offshore with a northeast flow (drainage wind coming from the southwest of Italy).

A third area (3 in Fig. 4.16a) can be observed in the Ionian Sea, in the Gulf of Taranto, where drainage winds reach 12 m s^{-1} at 03:00 UTC and converge offshore with a southwest synoptic flow. Several convective cells adopted a line of precipitation.

A fourth area (4 in Fig. 4.16a) can be differentiated in the extreme southeast of the Adriatic Sea, where southeast drainage winds move offshore to the Adriatic Sea. Several kilometers offshore, northwest drainage winds from the Italian inland move offshore in the Adriatic Sea. Both drainage winds converge offshore, forming several rain cells forming a quasi-stationary precipitation area.

Finally, the last interested area is located over the Adriatic Sea, between the Apennines and Balkans Mountains (indicated as 5 in Fig. 4.16a). The cyclonic rotation over this area associated with the relatively low pressure area located over the Ionian Sea (see Fig. 4.12) might be the main cause of the simulated precipitation over this area.

These precipitation areas are in a agreement with the precipitation estimated by TRMM.

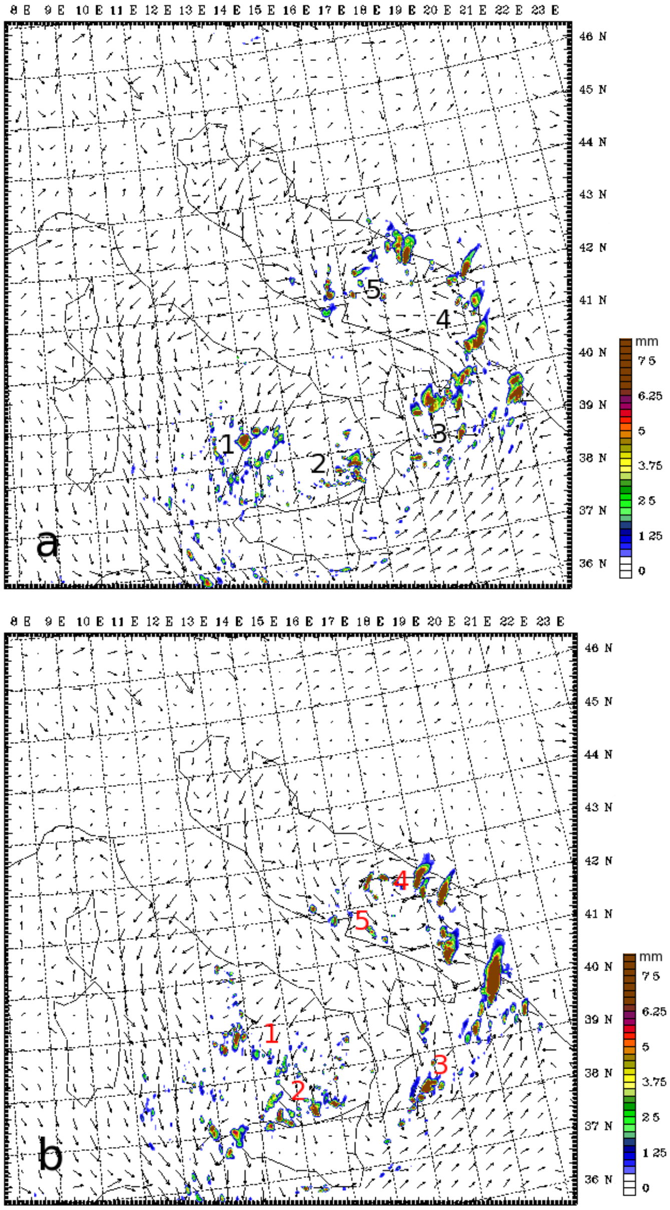

Figure 4.16: Simulated 1–h accumulated precipitation (color contours) and surface wind field (arrows) at (a) 03:00 UTC and (b) 08:00 UTC on 28 September 2004. The numbers indicate the precipitation areas associated with the line of convergence shown in Fig. 4.15. The maximum wind speed is (a) 11.1 m s^{-1} and (b) 12.5 m s^{-1}.

4.4 Sensitivity of CF precipitation on SST

4.4.1 Methodology for the numerical experiments

To analyze the influence of SST, in this section the results of the control run simulation (CR, presented in previous chapters) where the SST is provided by the model of the European Centre for Medium–Range Weather Forecasts (ECMWF), are compared with the run with a modified SST (SSTR) with the same parameterizations than CR (described in chapter 1). To prescribe the new SST the results obtained by Somot et al. (2008) for the different part within the Mediterranean basin at the correspondent season are used. The values of the increased SST for these events are 2.2 K for the CF5 (occurred during winter at the easter Mediterranean) and 2.5 K for the CF9 (occurred at the end of summer, in the western part of the Mediterranean basin). Figure 4.17 shows the location of these CFs.

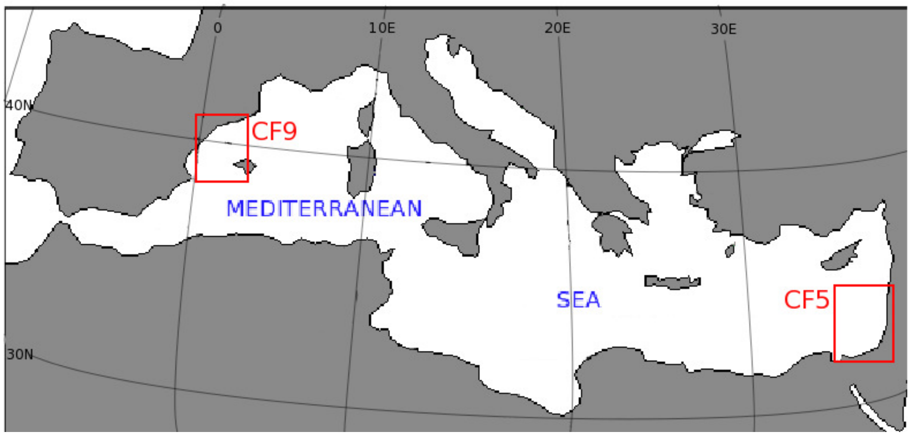

Figure 4.17: Location of CF5 and CF9 (red squares) in which the sensitivity analysis of SST in CF has been performed.

The analysis and comparison between CR and SSTR has been focussed on the 10–h accumulated precipitation, wind velocity, coastal front depth and the estimated parameters that accounts for the triggering, the blockage and the deceleration that the coastal front offers to the prevailing maritime air defined by Durran and Klemp (1987), Wang et al. (2000) and Miglietta and Rotunno (2010).

4.4.2 The rainband associated to CF5

Figure 4.18 shows the simulated 10–h accumulated precipitation in the smallest domain at 08:00 UTC on 6 January 2011, obtained by (a) CR (shown in chapter 2) and (b) SSTR, where the SST has increased 2.2 K. The line of precipitation simulated by CR is closer to the coast than the one simulated by SSTR. Both lines of precipitation are formed by several precipitations cells, with values of 10–h accumulated precipitation that has a maximum value around 26 mm in both cases. However, in the SSTR simulation the precipitation area is wider and a larger number of rainfall cells show higher values of 10–h accumulated precipitation. A warmer SST increases heat and moisture fluxes from the sea–water to the air, which may enhance precipitation rates and extension.

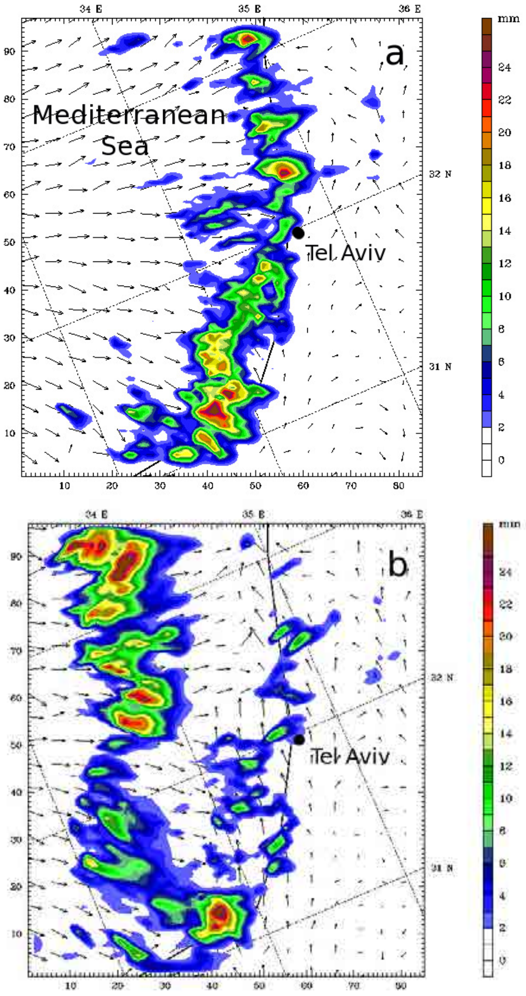

Figure 4.18: Simulated 10–h accumulated precipitation (color contours) and surface wind field (arrows) at the smallest domain at 08:00 UTC on 6 January 2011, obtained by (a) CR and (b) SSTR (ΔSST=2.2 K).

The differences simulated in the location of the precipitation can be explained because greater inland–sea air temperature difference increases thermal wind velocity (Khain et al., 1993). Consequently, for the SSTR the line of precipitation is shifted several kilometers offshore and the precipitation occurred mainly over the sea, while inland areas received less precipitation. Figure 4.19 shows the wind speed difference between CR and SSTR at 04:00 UTC. Warm colors indicate an increase in wind speed in the SSTR. This suggest that higher SST enhances the drainage wind speed by 5 m s^{-1} in some areas of the rainband. Consequently, the stronger wind keeps the line of precipitation offshore in respect to CR simulation.

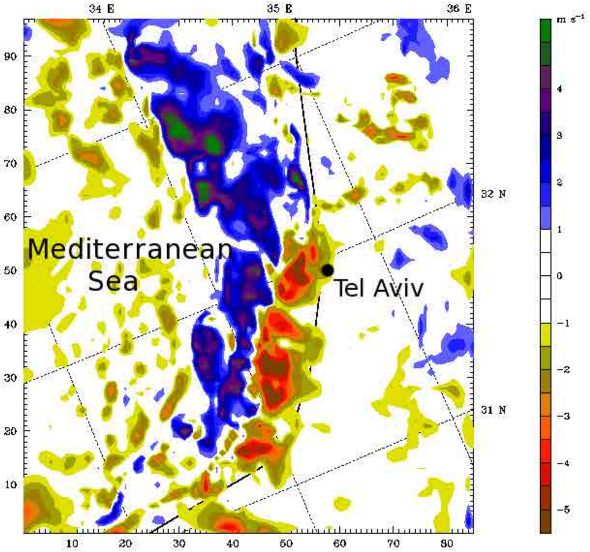

Figure 4.19: Simulated surface wind speed difference between CR and SSTR at 04:00 UTC on 6 January 2011 in the smallest domain. Negative values (warm colors) indicate intensification of the wind velocity for SSTR.

Focusing on the cold air depth, H, Fig. 4.20 shows the vertical cross section along the line AA' indicated in Fig. 2.4 of the potential temperature (color contours), the equivalent potential temperature (black lines) and the wind field (arrows) of SSTR at the same hours than the CR shown in Fig. 2.8. There are some significant differences between simulations. Lower values of H are obtained with respect the CR, especially from 04:00 UTC. Additionally, shorter offshore penetration of inland cold air into the sea is simulated in CR respect to the SSTR. For instance, at 06:00 UTC H is around 1000 m height and the coastal front head at sea–level is located approximately 35 km offshore in CR (Fig. 2.8c), while H is around 700 m height and coastal front head at sea–level is located father, around 50 km offshore in SSTR (Fig. 4.20 c).

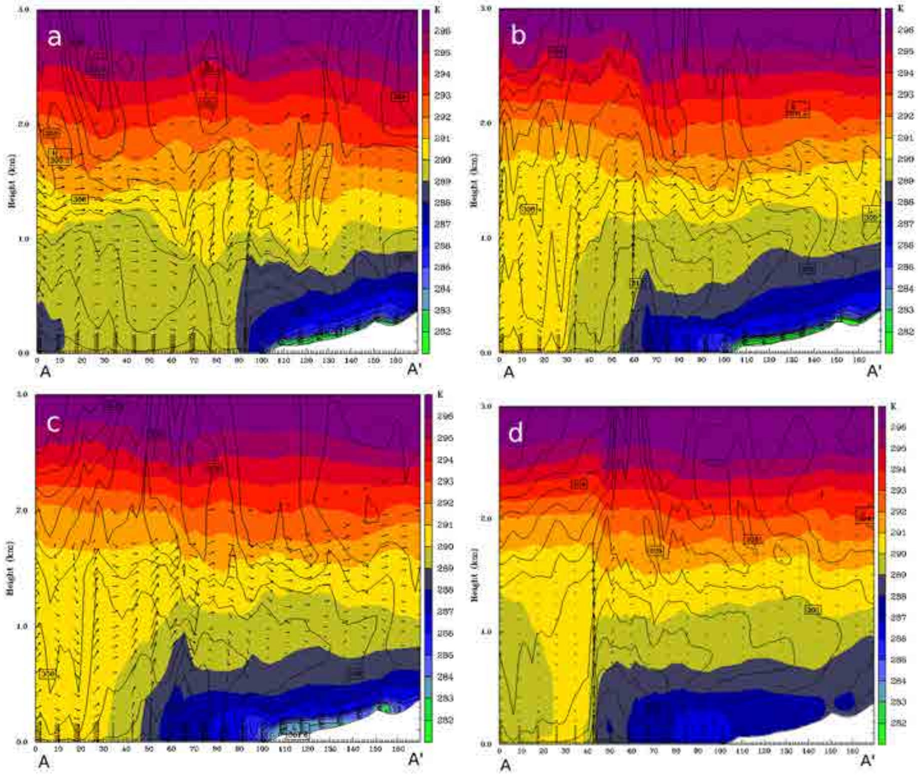

Figure 4.20: Simulated vertical cross section defined along the blue line AA' shown in Fig. 2.4 of the simulated potential temperature (color contours), equivalent potential temperature (black contour lines) and wind field (arrows) at (a) 00:00 UTC, (b) 04:00 UTC, (c) 06:00 UTC and (d) 08:00 UTC on 6 January 2011 in the SSTR (ΔSST=2.2 K).

The parameters that account for the triggering, the blockage and the deceleration that the cold air offers to the prevailing flow in the SSTR simulation have been estimated and compared with the CR. Figure 4.21 shows the temporal evolution of these parameters from 00:00 to 09:00 UTC estimated in the SSTR (closed lines) and compared with the CR simulation (dashed lines). Some differences appear when comparing both simulations.

Regarding the triggering term (H/LFC), lower values are estimated in the SSTR with respect the CR. In order to explain this, the LFC has been obtained from the SSTR and compared with the CR. No significant variations are noticed from 00:00 to 09:00 UTC, LFC is located approximately at the same height in both simulations. Consequently, the reduction in the estimated values of the triggering parameter are due to a lower estimation of H in SSTR. Despite of lower triggering term, higher precipitation rates are simulated along the rainband in SSTR, and the precipitation is wider. In order to explain this paradox, it is important to note that the triggering term does not take into account the vertical wind speed at the coastal front, but only accounts for the relation between the coastal front height

H with respect to the LFC. The simulated vertical velocity at the head of the coastal front are higher in SSTR, and consequently, larger amount of heat and humidity in a warmer SST can reach higher atmospheric levels. Consequently, deeper cumulus can be formed.

Focussing on the blockage term (NH/U), lower values are estimated in the SSTR with respect CR, which is consistent with the fact that H is lower in the SSRT. Furthermore, as H decreases in the SSTR, the upward maritime flow has a lower deceleration (NLFC$/U$). Therefore, the maritime wet air can reach higher levels with respect to the CR, forming deeper clouds, which produce larger amount of precipitation, as is shown in Fig. 4.18b. Moreover, SSTR simulates slightly higher values of CAPE, reaching maximum simulated values of 962 J kg^{-1} over the coastal front head at 06:00 UTC.

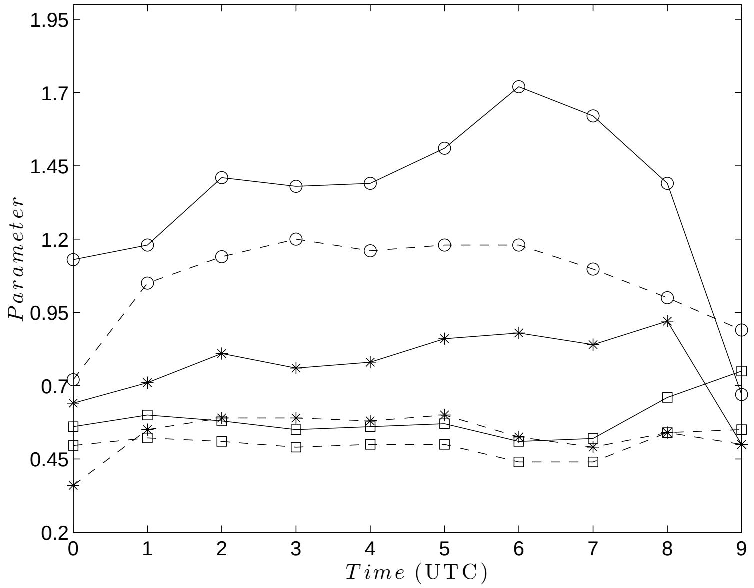

Figure 4.21: Temporal evolution of the estimated triggering (circles), blockage (asterisks) and deceleration (squares) terms in the SSTR simulation (dashed lines) and the CR (closed lines) simulations.

4.4.3 The rainband associated to CF9

The rainband associated to CF9 occurred during the night on 5 September and the early morning on 6 September 2011 in the northeast coast of the Iberian Peninsula, in the western part of the Mediterranean basin. As is described in Chapter 4, this rainband occurred at the end of the summer, when the SST present the largest values. The CR simulation shows a convergence due to the interaction of colder air masses (wind speed around 6 m s^{-1}) with a prevailing northeast wind that advects warm and wet air to the coast, forming an offshore line of convergence. Over this line of convergence, a line of precipitation is simulated and moves offshore until the early morning on 6 September 2011.

In order to evaluate the differences in the accumulated precipitation over the rainband, Fig. 4.22 shows the simulated 10–h accumulated precipitation at 08:00 UTC on 6 September 2011 obtained by (a) CR and (b) SSTR. CR shows a rainband of accumulated precipitation near and approximately parallel to the coastline, that reach around 30 mm over 10 hours in several areas along this line of precipitation. When the SST increases 2.5 K, the 10–h accumulated precipitation shows higher values in many parts of the rainband with respect the CR. The rainband moves away from the coast and is no longer parallel to the coastline in SSTR. (see Fig. 4.22 b).

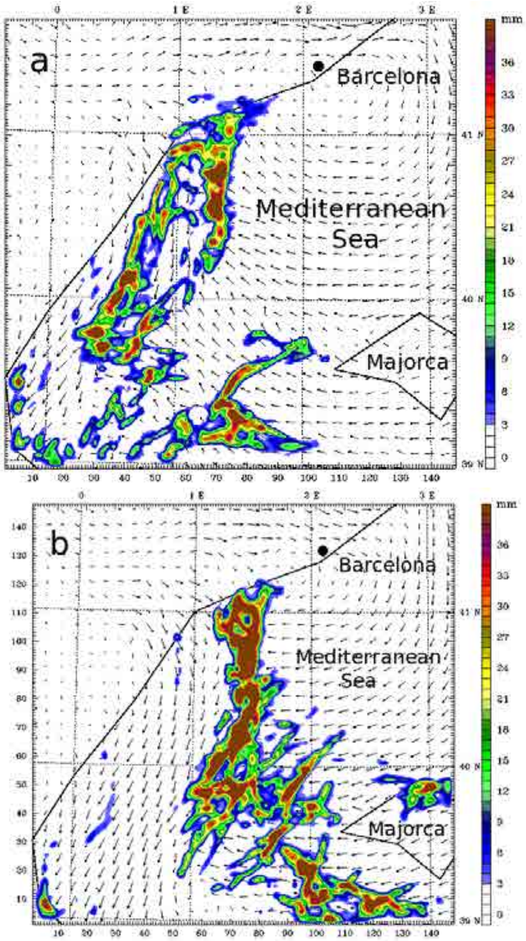

Figure 4.22: Simulated 10–h accumulated precipitation (color contours) and surface wind field (arrows) in the smallest domain at 08:00 UTC on 5 September 2011, simulated by (a) CR and (b) SSTR (ΔSST=2.5 K).

In order to explain these features, Fig. 4.23 shows the wind speed difference at 01:00 UTC between CR and SSTR. Negative values indicate that the velocity is higher in SSTR as compared to the CR. The intensified velocity of the drainage winds is noticed by observing the red colors near the coastline. This suggest that the inland cold air move offshore faster as a consequence of higher velocity in the drainage winds, due to the larger temperature difference between land and sea air masses in SSTR. Additionally, the precipitation formed over the coastal front is shifted offshore respect to the CR.

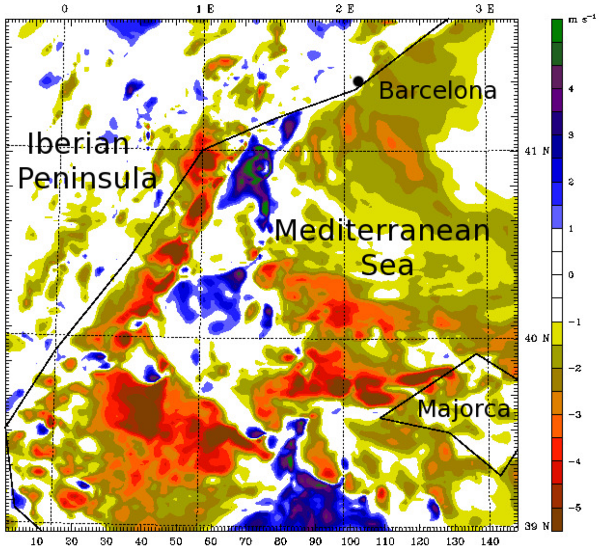

Figure 4.23: Simulated wind speed difference between CR and SSTR in the smallest domain at 01:00 UTC on 5 September 2011. Negative values (warm colors) indicate intensification of the wind velocity for SSTR.

The parameters that account for the triggering, the blockage and the deceleration that the cold air offers to the prevailing flow in the SSTR simulation have been estimated and compared with the CR. Figure 4.24 shows the temporal evolution of these parameters from 00:00 to 09:00 UTC estimated in the SSTR (solid lines) and CR (dashed lines) simulations.

Regarding the triggering term, lower values are estimated in the SSTR between 00:00 and 03:00, and quite similar values from 03:00 to 09:00 UTC. As in the analysis done in the previous subsection with the CF5, the location of the LFC shows quite similar values in both simulations, while H shows slight lower values in SSTR from 00:00 to 03:00 UTC, and similar values for the rest of the night.

Concerning to the blockage and deceleration terms, quite similar values are estimated in both simulations, suggesting that the air flows in a similar way around the cold air mass related to the coastal front.

Furthermore, simulated CAPE over the coastal front is increased in SSTR respect the CR, reaching maximum values around 1700–1800 J kg^{-1} respect to the CR, where maximum simulated values were around 1400–1600 J kg^{-1}.

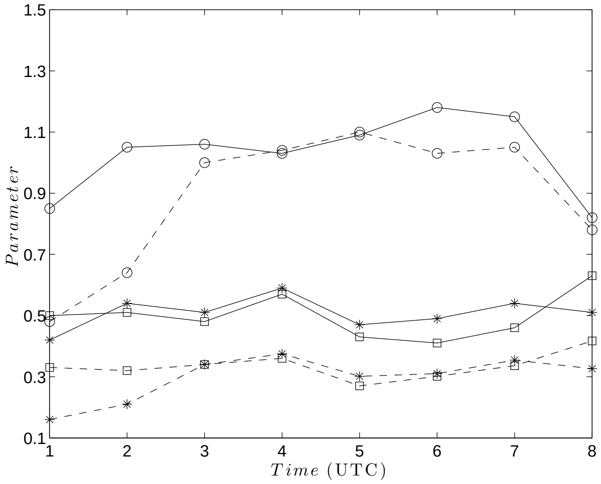

Figure 4.24: Temporal evolution of the triggering (circles), blockage (asterisks) and deceleration (squares) terms in the SSTR simulation (dashed lines) and the CR (closed lines) simulations.

4.5 Conclusions

Focussing on the first aim of this chapter, two CFs occurring in September (late summer), when the SST shows their maximum values after the summer, are analyzed. Higher values of the SST releases more heat and moisture from the sea to the lower troposphere, and then the sea–air becomes warmer containing larger values of moisture, which can condensate when ascending. Among the 10 simulated CFs, CF3 and CF9 are associated with the maximum value of the SST. CF3 occurred in the mid–west of the Italian peninsula, in the Tyrrhenian Sea on 27 September 2004, and CF9 in the northeast of the Iberian Peninsula on 6 September 2011. Focusing on the CF3, a relatively heavy rainband is recorded by reflectivity radar images, as well as by TRMM estimations. The simulation shows a rainband which moves offshore in a good agreement with these radar observations and TRMM estimations. WRF simulates a sea–air temperature around 297–298 K (the largest among the 10 simulated CFs in the Mediterranean basin), while the inland air temperature is about 293–294 K. At the coastal front head, the sea–air moves upward with a maximum velocity of 1.2 m s^{-1}. Over the offshore coastal front head, the simulated CAPE shows moderate values, reaching near 1600 J kg^{-1} at 06:00 UTC on 6 September 2011. Simulated precipitation cells within the rainband show 3–h accumulated precipitation of 25 mm at 06:00 UTC, quite similar value than the accumulated precipitation estimated by TRMM at 03:00 UTC.

Focusing on CF9, many precipitation areas were estimated by TRMM around the Italian Peninsula, over the Tyrrhenian, Ionic and Adriatic Seas. WRF simulations reproduce the location of many of these precipitation areas, which are characterized by relatively high values of sea–air temperature: 295 K over the Ionian Sea, 291 K over the Adriatic Sea and around 293 K over the Tyrrhenian Sea. WRF model simulates five different areas of precipitation (four associated with CFs) with a higher amount of precipitation associated to these precipitation cells with respect the TRMM estimations.

Concerning with the second aim of this chapter, a sensibility analysis of the influence of SST on the precipitation associated to coastal fronts has been studied by using WRF simulations. These experiments consist in increasing the SST 2.2 and 2.5 K according the projections obtained by Somot et al. (2008) for each season at the end of the 21^{st} century in the eastern (CF5) and western (CF9) Mediterranean basin, respectively.

In SSTR, the precipitation associated to the rainbands shifted offshore when comparing with the CR simulations. However, wider precipitation areas, with higher amount of accumulated precipitation, are simulated within the rainbands in SSTR. Concerning to the wind, SSTR show that drainage wind speed increases close to the coastline. In SSTR cases, the warmer sea–air induced by higher SST enhances the speed of drainage winds, which is consistent with the fact that the rainband is simulated futher offshore than in the CR simulation.

Simulated values of CAPE over the coastal front head are also increased for SSTR: an increase of 200–300 J kg^{-1} in CF9, and near 100 J kg^{-1} in CF5. These values are lower than those shown by Williams (1994), which found that over the tropical Pacific area an increase of 2 K in the SST implies at least an increase of 800 J Kg^{-1} increase in CAPE. However, the modification of the simulated CAPE are in a good agreement with the obtained by Ye et al. (1998). These authors found that CAPE increases around 200 J Kg^{-1} over the Pacific ocean in increasing 2 K the SST. According to these authors, an increase of CAPE of 200 J Kg^{-1} would result in a 10%–15% increase in the updraft air parcel velocity, of around 4 m s^{-1}.

The modification on the triggering, the blockage and the deceleration that the cold air offers to the prevailing maritime sea–air have been also analyzed. Concerning to the triggering term, lower values are estimated in the SSTR with respect the CR, as a consequence of lower values on the estimated coastal front depth, H, in SSTR. The blockage parameter takes quantify the blockage that the cold air associated to the coastal front offer to the prevailing maritime air (NH/U). This parameter shows lower values in the SSTR with respect CR, which is consistent with the fact that H shows lower values in the SSRT. Furthermore, as H decreases in the SSTR, the upward maritime flow has a lower deceleration, as the estimated deceleration term has shown.

As a final comment, despite the global warming has many and complex influences over the atmospheric dynamics, and consequently also over the nocturnal coastal fronts, the increase of the SST is one of the most significant affectations. As it has been shown in this chapter, in a warmer sea the rainbands are simulated further offshore, associated with higher amount of precipitation which falls over the sea. This may affect some regions where this type of precipitation is a significant source of water.

Chapter 5

The role of the coastal–front depth on cloud formation and precipitation

5.1 Introduction

As it was explained in Chapter 1, when ascending the maritime warm and wet air over the cold air, this warmer air may condensate and form stratiform clouds if the air reaches its Lifting Condensation Level (LCL). In some cases, convective clouds will appear if the corresponding Level of Free Convection (LFC) is reached. In both cases the depth of the colder inland air mass (coastal–front depth, H) plays an important role in helping the wetter and warmer maritime air mass to reach LCL or LFC (Schoenberg, 1984b; Miglietta and Rotunno, 2010). No clouds will form if $H <$ LCL.

This chapter[a] aims tho investigate the temporal evolution of the coastal–front depth for the ten nocturnal coastal fronts simulated around the Mediterranean basin (see Fig. 1.9).

Furthermore, several parameters related to trigger convection, the blockage effect that the cold air mass offers to the prevailing flow, the deceleration induced by cold front on the upstream maritime flow and the location of precipitation with respect to the front shown in Section 1.1.2 are estimated. Additionally, a forecasting cloud-band index is proposed in this chapter, in order to evaluate whether stratiform clouds are formed offshore in these ten simulated nocturnal coastal fronts.

---

[a] This chapter is based on Mazon, J. and Pino, D.: Role of the nocturnal coastal–front depth on cloud formation and precipitation in the Mediterranean basin. Atmos. Res. **153** (2015) 145–154

5.2 Estimation of the coastal–front depth

Determination of H is critical for the purpose of this research. For this reason two different methods have been considered to estimate H:

1. Method A. The coastal–front depth is defined here as the maximum height where a horizontal gradient of potential temperature exists. This is estimated for each simulation by plotting the vertical cross section of potential temperature along a line perpendicular to the coastline. Similar definition was already used by LaCasse et al. (2008) to analyze the evolution of the depth of land breezes at the coast of Florida (USA). The estimation of H by using this method presents slight variations during the evolution of the coastal front, and it can only be applied to cold fronts, where the boundary between air masses presents a significant slope. Additionally, the depth of the sea breeze has been also analyzed from mesoscale simulations by using a similar definition (Pérez et al., 2004; Hernández-Ceballos et al., 2013).

2. Method B: According to Simpson and Britter (1980), the depth of the cold air associated to a front moving offshore can be estimated by using the Eq.(1.2) shown in Chapter 1.

$$H = \frac{\theta_{v,w}(V_c + 0.7V_w)^2}{gk_S^2(\theta_{v,w} - \theta_{v,c})} \ , \tag{5.1}$$

We apply both methods for evaluating H every hour to the ten simulated CFs shown in Fig. 1.9. Figure 5.1 shows for each CF H obtained by method A (H_A) and B (H_B). As can be observed, similar values are obtained by using both methodologies. However, while H_B shows variations related to the hourly variation of the virtual potential temperature of both warm and cold air masses, and to their velocities, H_A is almost constant for several hours of the same event. Consequently, in the subsequent analysis the coastal–front depth is calculated by using method B and named H.

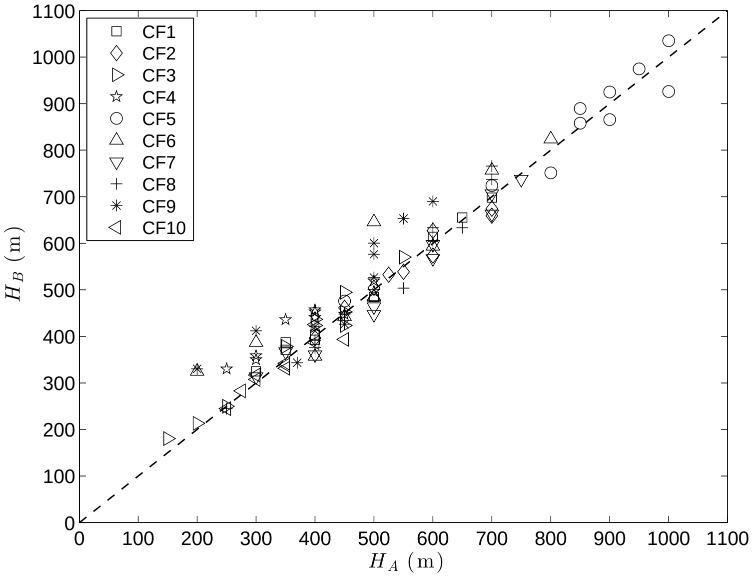

Figure 5.1: For all the analyzed CFs, hourly coastal–front depth estimated by using Simpson and Britter (1980) (H_B) method as a function of the coastal–front depth estimated by using the proposed definition (H_A).

5.3 Temporal evolution of the coastal–front depth

Figure 5.2a shows, for each hour of all the CFs, the estimated coastal–front depth by using Eq. 5.1 as a function of the 2–m potential temperature difference between the warm and cold air masses ($\Delta\theta = \theta_w - \theta_c$). Despite in Eq. (5.1) H is inversely proportional to $\Delta\theta_v$ ($\Delta\theta_v \sim \Delta\theta$), coastal–front depth increases with potential temperature difference. This can be explained because large sea–land air thermal difference increases the drainage wind speed of the cold air mass, V_c (Mapes et al., 2003a). Consequently, the increase in V_c has a larger effect on H that the increase of $\Delta\theta$, enhancing the vertical movements of the warm air mass.

Coastal–front depth has been averaged ($\overline{H}$) from 00:00 to 09:00 UTC, when the coastal fronts are well–developed. Figure 5.2b shows $\overline{H}$ as a function of the average 2–m sea–land potential temperature difference ($\overline{\Delta\theta}$). A good linear relationship is observed ($r^2 = 0.826$), suggesting that large average values of sea–land air temperature differences enhance the average value of the coastal–front depth.

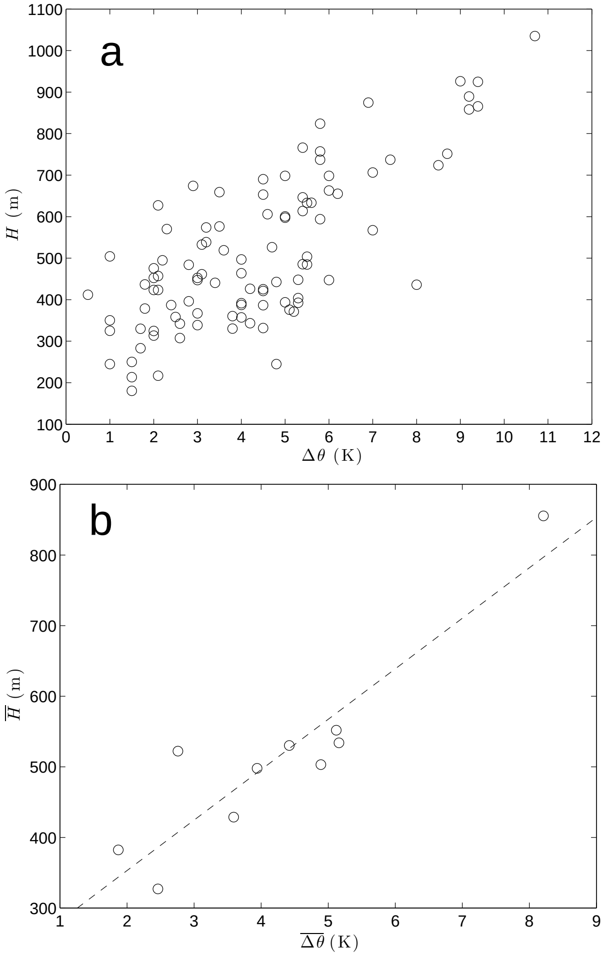

Figure 5.2: For all the analyzed CFs, (a) hourly, and (b) averaged H from 00:00 to 09:00 UTC as a function of the sea–land 2–m potential thermal difference. The dashed line in (b) is the linear fit to these date.

Focusing on the effect of wind speed of both warm and cold air masses on H, Fig. 5.3a shows H as a function of $U_t = V_c + V_w$. As expected, large values of H are associated with large U_t. These large values of U_t are mainly due to large values of V_c occurring when large land–sea air potential temperature difference exists for the simulated events. As larger the land–sea air potential temperature difference is, higher the drainage wind velocity is, which drives offshore the inland cold air (Schoenberg, 1984a; Khain et al., 1993). Additionally, H grows if $\Delta V = V_c - V_w$ takes small values. Regarding this point, Fig. 5.3b shows, for each hour of all the simulated CFs, U_t as a function of $\Delta V = V_c - V_w$ for different range of H. As can be observed, the largest values of H (squares) occur for large values of U_t and small values of ΔV. On the contrary, the lowest values of H (circles) correspond with low values of ΔV and U_t. However, no significant trend can be determined for medium range of H (greater than 300 m and lower than 900 m).

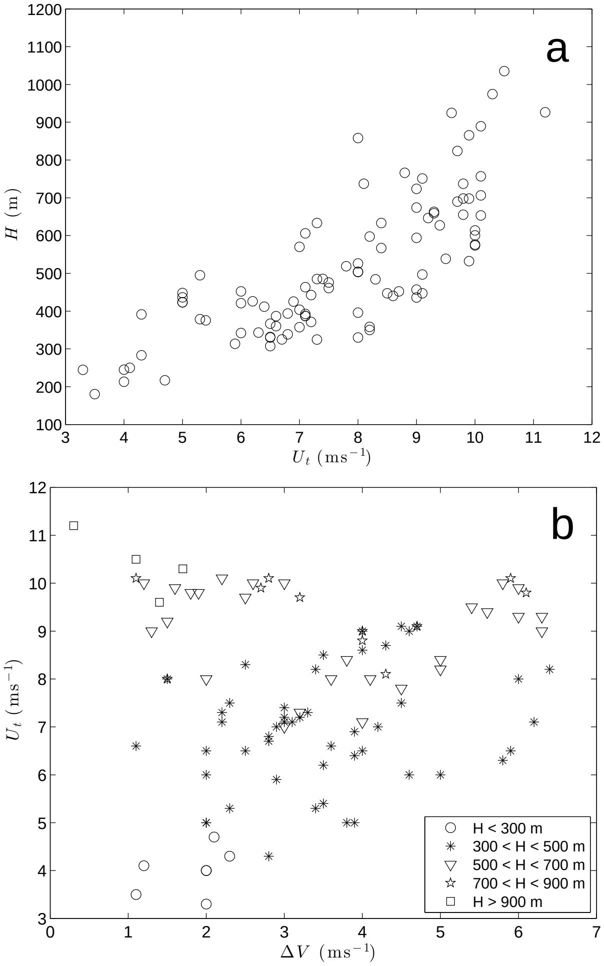

Figure 5.3: (a) H as a function of U_t for the ten simulated events front 00:00 to 09:00 UTC. In (b) U_t as a function of ΔV; H is plotted every 200 m for the ten simulated coastal fronts from 00:00 to 09:00 UTC.

5.4 Theoretical parameters associated to the evolution of a costal front

The parameters related to the trigger convection, the blockage that the cold coastal front offers to the warm maritime air mass, the deceleration induced by cold pool on the upstream

Event	Data	T_{WRF} (h)	T_{TRMM} (h)	P_{WRF12} (mm)	P_{TRMM12} (mm)
CF1	29 Jan 2008 (23 UTC)	10	8	20	15
CF2	28 Sept 2004 (00 UTC)	8	6	10	7
CF3	4Oct 2011 (00 UTC)	6	3	9	6
CF4	3 Dec 2010 (00 UTC)	7	3	0	2
CF5	6 Jan 2011 (22 UTC)	11	6	32	27
CF6	30 Jan 2008 (00 UTC)	9	6	4	3
CF7	4 Dec 2010 (00 UTC)	7	3	0	2
CF8	3 Mar 2011 (23 UTC)	10	6	5	4
CF9	6 Sept 2011 (23 UTC)	9	6	34	23
CF10	11 Oct 2011 (00 UTC)	8	3	3	2

Table 5.1: For each CF, duration (T) and 12–h accumulated precipitation (P) estimated by TRMM and simulated by WRF.

flow and the position of the precipitation (Durran and Klemp, 1987; Wang et al., 2000; Miglietta and Rotunno, 2010) described in Section 1.1.2 are estimated for the ten simulated CFs. Figure 5.4 shows the hourly evolution from 00:00 to 09:00 UTC of H/LFC, NH/U_t and $N\mathrm{LFC}/U_t$ for all the simulated CFs. Regarding the temporal evolution of the trigger convection parameter shown in Fig. 5.4a, CF1, CF5 and CF9 presents values higher than 1 during the whole night, indicating that the warmer and moister maritime air can reach the LFC, and convective precipitation can occur. According to the simulations, these CFs present the maximum amount and intensity of precipitation, as shows Table 5.1. The trigger convection parameter for CF2, CF8 and CF10 present values between 0.8 and 1 during few hours at early morning (between 05:00 and 08:00 UTC), when WRF simulates several precipitation cells. For the other events, the trigger convection parameter is lower than 0.8 during the whole night, suggesting that precipitation is not associated to convective processes. According to the simulations, weak precipitation occurs for CF3, CF4, CF6 and CF7 (see Table 5.1).

Figure 5.4b shows the temporal evolution of the blockage parameter, NH/U_t. Maximum values are estimated around early morning in all cases, when the estimated coastal front depth shows the maximum values and simulations show the maximum precipitation rate, between 05:00 and 08:00 UTC. Values between 0.3 and 0.8 are estimated, which can be classified as a weak blockage according to Durran and Klemp (1987).

Regarding the deceleration parameter, $N\mathrm{LFC}/U_t$, Fig. 5.4c shows a similar trend in this parameter for all the CFs. Between 05:00 and 08:00 UTC minimum values are estimated, suggesting that maximum accelerations occurred approximately when the trigger and the blockage parameters present the largest values (see Figs. 5.4a, b). From around 08:00 UTC, values of the deceleration parameter increase, which indicates that the deceleration induced by the cold pool on the upstream flow increases.

Finally the evolution of $B = U_t/N$ can be also analyzed by using Fig. 5.4c. Wang et al. (2000) showed that cloud bands form at the flow separation line between warm and cold air masses if the ratio $B = U_t/N > \mathrm{LFC}$. Consequently, these cloud bands appear if

Event	$\overline{H}$ (m)	$\overline{H/\mathrm{LFC}}$	$\overline{NH/U_t}$	$\overline{B}$ (m)
CF1	530	1.3	0.5	1004
CF2	551	0.8	0.8	1060
CF3	382	0.5	0.4	840
CF4	428	0.5	0.4	800
CF5	855	1.3	0.8	1090
CF6	530	0.4	0.6	900
CF7	430	0.5	0.5	810
CF8	533	0.8	0.6	870
CF9	497	1.0	0.5	1010
CF10	326	0.6	0.5	620

Table 5.2: For each CF, averaged values from 00:00 to 09:00 UTC of H, LFC, H/LFC, B and NH/U_t.

$B/\mathrm{LFC} > 1$, but B/LFC is the inverse of the deceleration parameter. As Fig. 5.4c shows the deceleration parameter is less than 1 during several hours for all CFs except for CF6. Consequently, for all the CFs, except for CF6, $B/\mathrm{LFC} > 1$, and the cloud bands are located over the separation line. CF6 (see Chapter 3) presents light non–convective precipitation during several hours and WRF estimates a very large LFC.

Table 5.2 shows the average values from 00:00 to 09:00 UTC of H/LFC, NH/U_t and B. The averaged parameters over the whole night allow to analyze the average evolution of the front during this period. Regarding the average of the trigger convection parameter, $\overline{H/\mathrm{LFC}}$, only CF1, CF5 and CF9 shows values greater than 1, suggesting that convective cells are forming during the whole night. These two events are characterized by relatively heavy precipitation during the whole night. CF2 and CF8 present values of $\overline{H/\mathrm{LFC}}$ between 0.8 and 0.9, suggesting that during many hours at night convective cells are forming. For the rest of the simulated CFs the average trigger convection parameter presents values between 0.4 and 0.8, suggesting that stratiform precipitation is dominant.

Regarding to parameter $\overline{B}$, all values are higher than $\overline{\mathrm{LFC}}$, suggesting that the precipitation cells and bands are formed over the front.

The average blockage term ($\overline{NH/U_t}$) shows values between 0.4 and 0.8, suggesting that the cold drained air offer a weak blockage to the prevailing air during the whole night.

5.5 Forecasting cloud bands index

Cloud and rain bands associated to the simulated nocturnal coastal fronts occurred at low levels in the troposphere within the meso–β and meso–γ scales. As a consequence, they are difficult to be forecasted. In this section a simple index to forecast cloud bands associated to nocturnal offshore coastal fronts is defined and verified. This index only depends on the

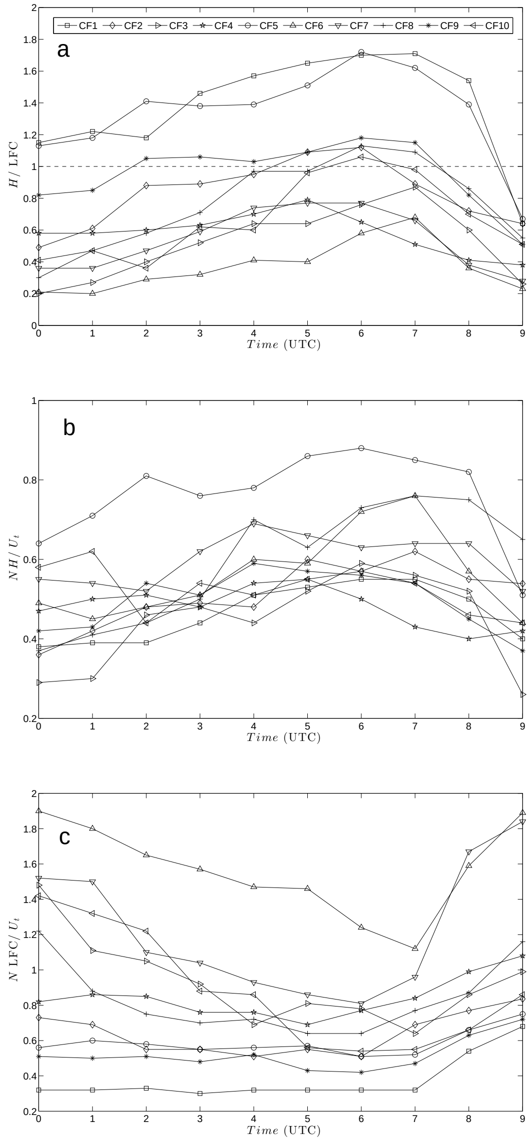

Figure 5.4: Temporal evolution from 00:00 to 09:00 UTC for the ten simulated CFs of the estimated parameters (a) trigger convection, (b) blockage and (c) deceleration induced by cold pool on the upstream flow.

average 2–m temperature of the cold and warm air masses ($\overline{T_c}$, $\overline{T_w}$) and on the average 2–m dew point temperature of the warm air mass ($\overline{T_{d,w}}$).

As mentioned in previous sections, clouds are formed over the coastal front if $H \geq$ LCL.

Taking into account Espy's equation (Bohren and Albrecht, 1998), LCL $= \alpha(T_w - T_{d,w})$, where $\alpha = 125$ m K^{-1}, clouds are formed over the coastal front if $H \geq \alpha(T_w - T_{d,w})$. From 00:00 to 09:00 UTC for the ten simulated CFs, LCL, T_w and $T_{d,w}$ show small variations. Then, $\overline{H} \geq \alpha(\overline{T_w} - \overline{T_{d,w}})$ fulfills. As it was shown in Fig. 5.1b, a good linear relationship exists between $\overline{H}$ and $\overline{\Delta\theta}$, being $\overline{H} \approx A_2 + A_1\overline{\Delta\theta}$, where $A_1 = 67.6$ m K^{-1} and $A_2 = 232$ m. Finally, assuming that at sea–level $\theta \simeq T$, we can conclude that clouds will form over the front if

$$\overline{T_c} \leq \tau = \frac{\overline{T_w}(A_1 - \alpha) + \alpha\overline{T_{d,w}} + A_2}{A_1}. \tag{5.2}$$

The forcing mechanism, which helps the warm air to reach LCL, is related to the colder air mass associated to nocturnal CF that enhances vertical movements of the warmer and moister maritime air mass. Due to this mechanism, the above condition is a necessary and also sufficient condition to form clouds. Figure 5.5 shows $\overline{T_c}$ as a function of τ for the ten simulated coastal fronts. As can be observed, the relationship $\overline{T_c} \leq \tau$ is verified for all the analyzed CFs.

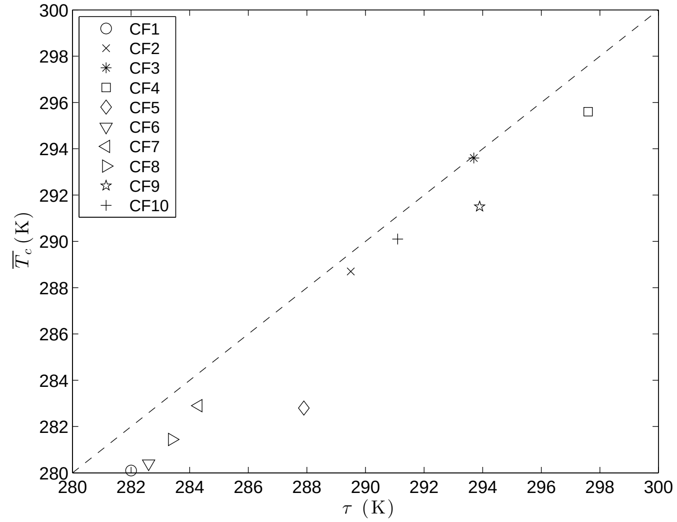

Figure 5.5: For all the analyzed CFs, τ as a function of the average 2–m temperature of the cold air mass ($\overline{T_c}$).

5.6 Conclusions

In this chapter H has been evaluated by using two methodologies (for the ten detected and simulated CFs). The first methodology is based in evaluating H by plotting the vertical cross section of the simulated potential temperature. The second methodology uses the equation proposed by Simpson and Britter (1980). Both methods show quite similar results. From this evaluation, the average and the maximum coastal–front depth in each event has been estimated.

By analyzing the time evolution of H for each CF, it can be concluded that the maximum depth of the cold air mass, which occurs for all the cases during the early morning, is related to the module of the relative wind speed between the cold and the warm air masses at the coastal front head (U_t), and to the 2–m potential temperature difference between the two air masses ($\Delta\theta$). If the two air masses have similar wind speed, ΔV is small, but $U_t = V_c + V_w$ is large, and H_{max} is larger when compared to the cases in which both ΔV and U_t are small.

The cold air mass acts similar to a moving orographic barrier to the warmer prevailing flow. For this reason the parameters proposed by Miglietta and Rotunno (2010), Wang et al. (2000) and Durran and Klemp (1987) in their idealized studies have been adapted in order to analyze the dynamic of the CFs. Regarding the blockage parameter, NH/U_t, values between 0.4 and 0.8 are estimated, suggesting that the CFs offers a weak blockage to the prevailing maritime air flow. The largest values of this parameter are estimated between 05:00 and 08:00 UTC, when H presents the maximum values. From 08:00 UTC this parameter decreases with H because the cold drained air warms and the drainage wind speed decreases.

Focusing on the trigger convection parameter, H/LFC, values higher than 1 are estimated for those CFs with relatively larger amount of precipitation simulated (CF1, CF5, and CF9), specially between 05:00 and 08:00 UTC, suggesting that convective processes induced this precipitation during practically the whole night. For CF2, CF8 and CF10 this only occurs during some hours. For the rest of the simulated CFs, the trigger convection parameter presents smaller values, between 0.4 and 0.9, during the whole night.

The deceleration parameter, $N\text{LFC}/U_t$, presents values smaller than during most of the time for all the CFs except for CF6 due to the larger LFC simulated in this event.

The averaged trigger convection parameter, $\overline{H/\text{LFC}}$, shows values greater than 1 for CF1, CF5 and CF9. This suggests that rain bands were formed during the whole night. In these three events, the 12–h accumulated–precipitation pattern at 09:00 UTC is a stationary offshore line parallel to the coast. For CF2 and CF8 average H/LFC takes smaller values but close to 1, and, the rain cells are also significant during the night. For the other cases (CF3, CF4, CF6, CF7, CF10), the trigger has values between 0.4 and 0.8, suggesting that convective cells are not formed continuously during the night.

A cloud band forecasting index is proposed by using the classical Espy's equation and the relationship found between the average coastal–front depth and the sea–land thermal difference for the ten simulated coastal–fronts. If the average dew point temperature over the sea ($\overline{T_{d,w}}$) and the average cold coastline temperature ($\overline{T_c}$) are known, the defined index

τ is larger than $\overline{T_c}$ for each of the ten simulated coastal fronts, suggesting that clouds are formed over the coastal front.

Chapter 6

Overall conclusions and further research

6.1 Summary of the aim, approach and main results of the thesis

The main goal of this Thesis is to investigate the formation of nocturnal offshore precipitation near the coastline around the Mediterranean basin. It focusses on this area because, despite nocturnal precipitation associated to coastal fronts has been well studied over the tropical regions, the Mediterranean basin presents a lack of research. This thesis fills the existing gap of the current knowledge about this phenomena on this area.

The hypothesis to explain these precipitation events is based on the formation of nocturnal coastal fronts, not associated to a low–pressure center or large–scale synoptic fronts. During the night the inland air mass cools faster than the maritime air mass. Then drainage winds move offshore the cold inland air mass following rivers, valleys, streams and sloping down the mountains located close to the coastline. This cold air mass forms a coastal front when interacting with the warmer sea–air. The warmer and moister maritime air mass is lifted over the cold air mass and clouds and rainfall can form. Depending on the depth of the cold air mass (H), LCL and LFC of the warm air, clouds or precipitation can occur. Moreover, several theoretical parameters defined to quantify the intensity and location of convective rainfall over an idealized mountain have been adapted and applied here, assuming that the cold air associated to a coastal front acts as a mountain to a prevailing flow. These parameters accounts for the triggering, the deceleration and the blockage that the front offers to the prevailing flow, and whether the precipitation occurs over the flow separation line between the cold and the warm air masses.

Ten coastal fronts have been simulated by using the version 3.3 of the WRF–ARW model. In chapter 2, the role of the land–sea thermal gradient has been analyzed, showing that the large sea–land thermal difference enhances drainage wind moving the associated inland cold air offshore. In Chapter 3, the shape of the coastline is analyzed. Concave shape enhances offshore convergence of drainage winds, which form offshore coastal–fronts. In Chapter 4, the influence of a large SST is studied. A couple of CFs, occurring in early autumn, when the SST presents the largest values in the Mediterranean basin, have been simulated. Additionally, two numerical experiments have been performed in order to evaluate the sensitivity of the precipitation associated to the CFs to the SST. Finally, in Chapter 5, the role of the coastal–front depth (H) on cloud and rainbands has been investigated. Moreover, based on the average value of H for the ten simulated coastal fronts, an index (τ) has been proposed to forecast cloud bands associated to the coastal fronts.

6.2 Answers to the original research questions

The specific objectives of this thesis have been formulated as several detailed research questions in the introduction. In this section answers are given based on the results presented in previous chapters.

1. *Are the physical processes responsible for the precipitation associated to nocturnal coastal fronts on the Mediterranean basin the same as those found by other authors on the tropical regions?*

   Yes. Simulations of nocturnal precipitation events around the Mediterranean basin show that drainage winds drive offshore the inland cold air during the night and early morning. The cold air mass forms a coastal front when interacts with the warm air mass over the sea. Over the coastal fronts, WRF model simulates clouds, rain cells and rainbands which remain stationary or move offshore as the night advances. From early morning, the drainage wind vanishes and as a consequence precipitation dissapears. This physical process is the same as referenced on tropical regions by several authors.

2. *What are the main factors influencing this mechanism of precipitation?*

   The main factors investigated in this Thesis that influence over the coastal fronts are four: land–sea air thermal gradient, shape of the coastline, sea surface temperature, and coastal–front depth.

   Among the studied CFs, three are characterized by a relatively large land–sea air thermal gradient: CF5, occurred at the eastern Mediterranean on 6 January 2011, CF8 occurred at the southwest of the Mediterranean basin (south of the Iberian Peninsula) on 3 March 2011 and CF10, at the northeast of the Iberian Peninsula on 13 October 2010. Note that these events occurred in winter (CF5 and CF8) and mid autumn (CF10), when the inland air has been cooled while the sea surface temperature is still relatively warm. CF5 shows the higher land–sea air thermal difference, with around 8–10 K simulated at early morning on 6 January 2011; CF8 shows thermal differences around 6 K, and CF10 around 7 K. As a consequence of this thermal difference, drainage winds can develop and consequently drive offshore the inland air mass, forming a well marked line of convergence.

In two coastal fronts the shape of the coastline played an important role: CF6 occurred over the gulf of Sidra, in the mid South of the Mediterranean basin on 30 January 2008, and CF1, occurred in the gulf of Genoa, in the Northwest Mediterranean basin on 29 January 2008. The concave shape of the Gulf of Sidra and the gulf of Genoa plays an important role in enhancing convergence offshore. Concerning to the CF at the Gulf of Sidra, a rainband formed by several raincells is formed by offshore convergence near the coastline, caused by inland cold air driven by drainage winds from many areas along the concave coastline in the extreme East of the Gulf of Sidra. Drainage winds move the inland air mass offshore from the opposite parts of the concave coastline, converging offshore. Additionally, the inland air masses also converge frontally with the northern synoptic flow. The result is a convergence area that moves heat and moisture upwards from the sea, at velocities that reach 1.2 m s^{-1}. Due to this strong vertical velocity, and despite there is a large atmospheric stability aloft which prevents the formation of severe convection, the air reaches LCL that is located at around 800–1100 m.

Concerning the CF at the Gulf of Genoa, a line of convergence is simulated parallel to the coastline of this gulf, formed by drainage winds from many areas along the concave coastline. A rainband is formed over this line of convergence, remaining quasi–stationary for several hours.

The SST has also a significant importance in enhancing precipitation associated to nocturnal coastal fronts. This influence has been studied in CF3 and CF9, both occurred in September, where maximum values of the SST exist. CF3 occurred at the west of the Italian peninsula, in the Tyrrhenian Sea on 27 September 2004, and CF9 in the northeast of the Iberian Peninsula on 6 September 2011. A higher SST value releases more heat and moisture from the sea, and if this air moves upwards it can condensate at lower levels. Focusing on CF3, the surface sea–air is around 293 K over the Tyrrhenian Sea, with a thermal gradient of around 3–4 K. For the CF9, the simulated sea–air temperature is around 296 K, while the simulated inland air temperature is around 294 K, as in the CF3 around 3–4 K of thermal gradient. Despite this relatively lower thermal gradient, precipitation occurs in both events, specially in CF9, where a heavy rainband is observed and simulated.

Furthermore, a sensibility analysis of the coastal–front precipitation to the SST has been done by performing two additional numerical experiments. The SST has been increased by 2.2 and 2.5 K according the projections obtained by Somot et al. (2008) for each season at the end of the 21^{st} century in the CF5 and CF9. These simulations show an increase of the precipitation field when the SST is increased. The simulations also show that the drainage wind velocity increases, and the rainbands formed in CF5 and CF9 are located far away of the coast.

3. *What is the meteorological scale in which these events occurs?*

   Taking into consideration the classification proposed by Orlanski (1975), the observed and simulated coastal fronts in this Thesis can be included within the meso–β and meso–γ scales. Focussing on time, the observed and simulated coastal fronts have lasted from 3 hours (CF10) to the whole night, around 10 hours (CF5, CF1, CF9). Regarding the horizontal dimension, the maximum rainband associated to a coastal front has around 150–200 km long (CF5, CF9), and the minimum horizontal dimension around 20–30 km long (CF10).

Considering the coastal–front depth, H, its maximum estimated value has been 1052 m at the early morning in the CF5, and minimum estimated value is 190 m in CF10. However, average values of H ranges from around 350 to 850 m, being around 500–600 m the most frequent average H.

Taking into account the scale classification proposed by Markowski and Richardson (2010), the ratio H/L between the vertical (H) and the horizontal (L) scales defines whether a meteorological phenomenon is either hydrostatic (if $(H/L \ll 1)$ or is not $(H/L \geq 1)$. This parameter on the simulated CFs ranges CF, it ranges from 0.01 for the CF10 to 0.001 for the CF9 and CF5. Consequently, all the CFs simulated in this Thesis are hydrostatic.

4. *In which synoptic atmospheric conditions do these events form?*

   By using the NCEP reanalysis information, the synoptic configurations at 500 hPa and 850 hPa have been investigated. It is important to remark that following the criterion defined in the methodology, the selected nocturnal coastal fronts in this Thesis are not associated to a low–pressure area or to large–scale synoptic fronts. As a common feature, a weak cold outbreak at 850 hPa is observed in all coastal fronts, but not always corresponding with a lower geopotential height at 500–hPa, where in some cases a warm ridge is observed.

   Additionally, WRF–ARW simulations show that the vertical profile of the equivalent potential temperature decreases over the coastal front, suggesting that a certain degree of local instability exist at low levels. Moreover, low values of CAPE are simulated in all the studied events, smaller than 1000 J kg^{-1}, which suggest that these events are associated to weak instability. Only for the CF9, CAPE reaches around 1500 J kg^{-1}, and relatively heavy precipitation is simulated.

5. *Why do cloud bands sometimes develop producing showers and rainbands, and sometimes no clouds appear?*

   After sunset the cool inland air moves into the coastline. The warm and wet sea–air is lifted by the cold, drained air as it moves offshore. There are several factors influencing this phenomenon, such as the intensity of the drainage and prevailing winds, the coastal–front depth (H), or the atmospheric stability. If the warm air mass reaches LFC, convective clouds are formed and may produce precipitation. Moderate precipitation occurs if H is located above the LCL, which is close or above the LFC. In contrast, stratiform clouds with no or weak precipitation are formed if $LFC > H > LCL$, or there no clouds form if $H < LCL$. CAPE is the most used parameter to indicate the atmospheric instability.

6. *Would it be possible to forecast the cloud bands formed at the coastal–front by using a simple empirical index?*

   A cloud band forecasting index, τ, has been proposed by using the classical Espy's equation (Bohren and Albrecht, 1998) and the relationship found between $\overline{H}$ and $\overline{\Delta\theta}$ for the ten simulated coastal fronts. If the average dew point temperature over the sea ($\overline{T_{d,w}}$) and the average cold coastline temperature ($\overline{T_c}$) are known, the defined index τ is larger than $\overline{T_c}$ for each of the ten simulated coastal fronts, suggesting that clouds are formed over the coastal front.

6.3 Further research

Taking into account the presented results and the limitations imposed by the model assumptions, further research about the following topics is suggested.

1. *To analyze additional CFs in the Mediterranean Basin*

   By so doing we will (a) enlarge the geographical zones within the basin where these phenomena occur, (b) enlarge the seasonal period where CFs form (spring and summer) in order to compare with those presented in this thesis, (c) estimate more variables related to CFs, (d) evaluate the contribution on the water budget of these CFs, and (e) analyze and quantify the contribution of the rain fall over inland in some areas, especially in arid areas.

2. *To study events occurring at two opposite and close coastlines*

   In the Mediterranean basin there are some areas characterized by two nearby and opposing coastlines, such as the Alboran, Adriatic, or Aegean seas. In these areas, the collision of two air masses driven by drainage winds can enhance the vertical motions over the sea producing larger amounts of precipitation.

3. *Verification of index τ*

   The proposed cloud bands forecast index, τ, defined in Eq. (5.2) in Chapter 5 has to be verified for additional CFs.

4. *Extension of the analysis to the Red and Black seas*

   No reference dealing precipitation associated to coastal fronts over the Red and Black seas has been found. Red Sea is a long strip of warm sea surrounded by mainly desert areas with elevation that reach around 1000 m in some areas. Black Sea is a enclosed sea, with approximately circle shape, surrounded by high elevations, where drainage winds can reach significant values. The large concave shape of the coastline can enhance the offshore convergence of the inland air mass offshore.

Appendix A

Frontogenesis at mesoscales in the West Mediterranean basin

It is well known (Alpert et al., 1990; Trigo et al., 1999; Reale and Atlas, 2001) that in the Mediterranean basin, especially at the western and center areas, cyclones are formed. This appendix aims to demonstrate that fronts, not related to low–pressure areas or cyclones, form within the whole mesoscale over the West Mediterranean basin. This new idea is supported by the analysis and the simulation of three observed fronts, each one in the three sub–mesoscales. The nocturnal coastal fronts CF9 and CF10 presented in chapters 4 and 2 are within the meso–β and meso–γ scales, respectively, formed during the night by interacting the inland cold air mass drive by drainage winds with the warmer sea–air. Additionally, cold outbreaks over the gulf of Lion (see Fig. A.1 for location) may form meso–α fronts when the cold air mass moves offshore over the West Mediterranean basin.

As a consequence of the many surrounding mountains ranges that in some areas exceed 2000 m, the western Mediterranean basin (hereafter WMB) is a semi-enclosed basin. At the north, there are three major mountain ranges (Pyrenees, Massif Central, and Alps, see Fig. A.1). These topographical features combine to create a channeling effect of the air that flows between these mountain ranges. Moreover, along the southern coast of the WMB, the Atlas mountain range dominates North Africa, with elevations that reach 2000 m close to the coastline. At the western part, some mountain ranges in the Iberian Peninsula (Betica Mountains, Iberic System) are located close to the coast with elevations between 700 and 3000 m. Finally, in the eastern part of the area, the Apennines range enclosed the basin. Consequently, at low levels the air over the sea can be replaced only through some areas, the Gulf of Lion, the strait of Gibraltar and the strait of Sicily. All these facts allow to consider the WMB as a source region, where the named Mediterranean air mass is originated (Jansà, 1959). High temperatures and high moisture content, especially during the summer and autumn, characterize the surface air in this region.

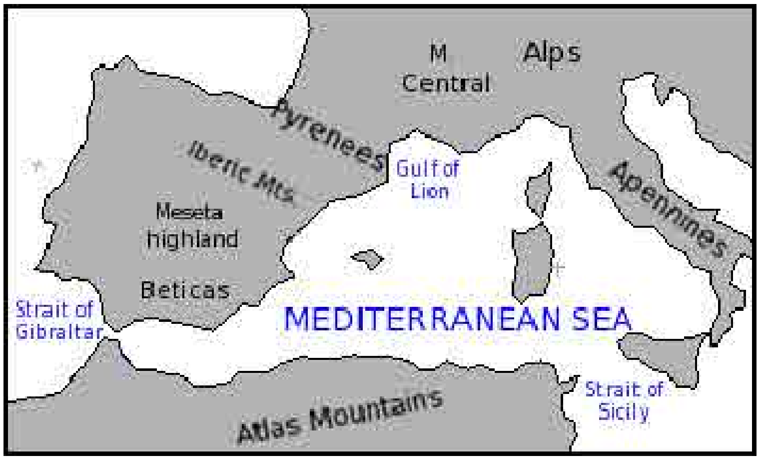

Figure A.1: The area under study with the locations of the main orographic features in the WMB.

It is important to remark that the WMB has been mainly studied and characterized as a cyclogenesis area (Ulbrich et al., 2009; Buzzi and Tibaldi, 1978; McGinley, 1982; Radinovic, 1986). More recently, the HYdrological cycle in Mediterranean EXperiment project (HyMeX, Drobinski et al. (2013); Ducrocq et al. (2013)) is analyzing by using observations and numerical simulations the water budget in the WMB. However, the main concept suggested here, i.e., WMB is a frontogenesis area at the whole mesoscale not necessarily associated to cyclones, is not suggested in any of these previous works and it is not a subject considered in HyMeX. Consequently, the studied CF9 and CF10 within the meso–β and meso–γ, and the meso–α front presented in this appendix show a new perspective about the frontogenesis in the WMB, contributing to add a new point of view and improving the knowledge of the meteorological events that occur in the WMB.

A.1 Cold outbreaks forming meso–α fronts in the WMB

Due to the complex orography that surrounds the WMB, outbreaks of cold air over the warmer and moister sea–air may occur at the mesoscale. Cold air into the WMB at meso–α usually comes from the gulf of Lion, associated to synoptic northwesterly flow known as Mistral or tramontana wind. Mistral is a cold and strong northwesterly to north-northeasterly offshore wind perpendicular to the coast of the Gulf of Lion. Its influence occasionally extends beyond the Gulf of Lion (Jansà, 1987) and affects the weather of the whole WMB, being one of the primary causes of storms over some areas of the western Mediterranean basin (Trigo et al., 1999; Campins et al., 2000). Mistral produces an intense air–sea heat exchange (Flamant, 2003) and sea surface cooling (Millot, 1979). During Mistral clear skies are usually reported and precipitation is uncommon except if the Mistral occurs at low levels interacting with a southerly flow (Jansà, 1987). In some of these cases shallow clouds, even convective clouds and weak precipitation may appear associated to the cold front formed as a consequence of the cold outbreak over the warmer Mediterranean sea-air (Jiang et al., 2003).

As an example of meso–α front formation, the cold outbreak occurred on 25 and 26 August 2012 is analyzed. Figure A.2 show the domains used in this simulation (upper panel) and the orography surrounding the WMB (lower panel).

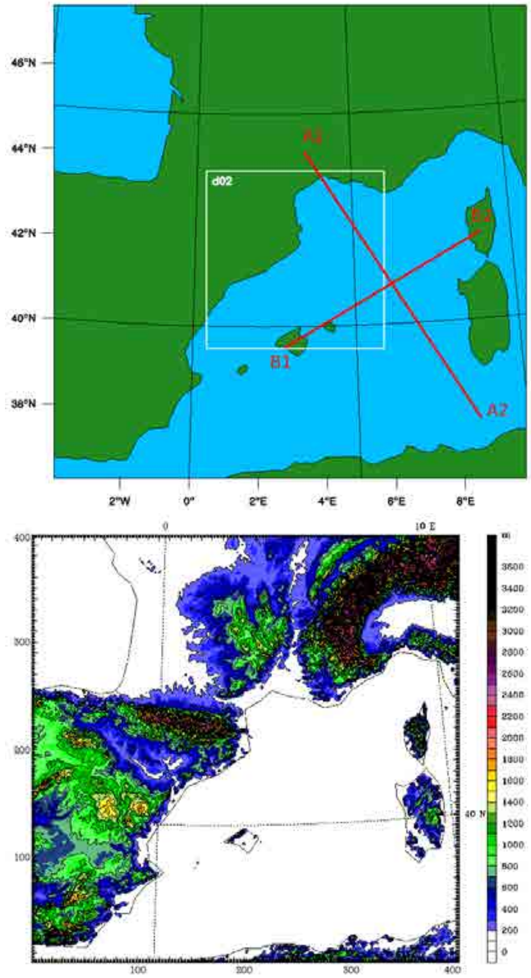

Figure A.2: In upper panel, domains used in the WRF simulation. The red lines A1–A2 and B1–B2 are the projection of the vertical cross section used in the analysis of this event. In the lower panel, the orography surrounding the WMB in domain1.

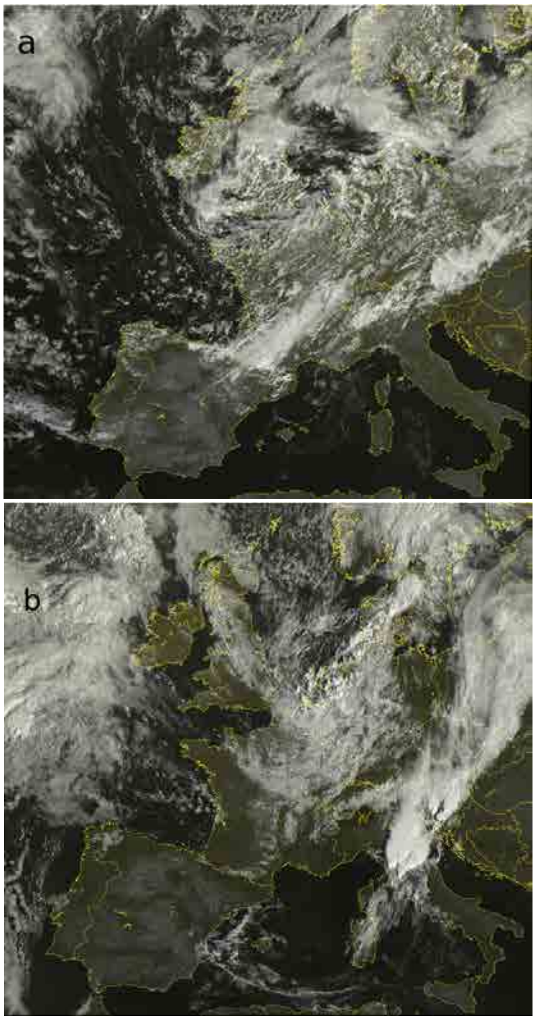

Figure A.3: Visible images recorded by Meteosat satellite at (a) 12:00 UTC on 25 August 2012 and (b) 08:00 UTC on 26 August 2012.

A.1.1 Observations

Figure A.3 shows the image recorded by Meteosat satellite in the visible channel at (a) 12:00 UTC on 25 August 2012 and (b) 08:00 UTC on 26 August 2012. An arc of clouds located offshore the coast of the gulf of Lion is recorded at 12:00 UTC. It moved offshore and expands out in the WMB. At 08:00 UTC on 26 August 2012, the cloud arc was located near the north of the African cost. No precipitation was observed during those days in the area under study.

A.1.2 Synoptic analysis

Figure A.4a shows the NCEP reanalysis of geopotential height at 500 hPa and the surface pressure on 26 August 2012 at 00:00 UTC. A ridge affecting the WMB defined the synoptic situation at 00:00 UTC on 25 August 2012. A low–pressure area (1000 hPa) located south of the British Islands had associated a synoptic polar cold front elongated from south of the British Islands to north of the Iberian Peninsula and moving northeastward. At 12:00 UTC on 25 August 2012 this cold front was located at central Europe, and the low–pressure center displaced to the Northeast, located over the west coast of the Jutland Peninsula. Figure A.4b shows the reanalysis of the temperature at 850 hPa on 26 August 2012 at 00:00 UTC. A north and northwesterly advection over the gulf of Lion was well defined. It is important to notice the different direction of propagation of the synoptic polar cold front, moving northeastward, and the meso–α coastal front analyzed below moving southward.

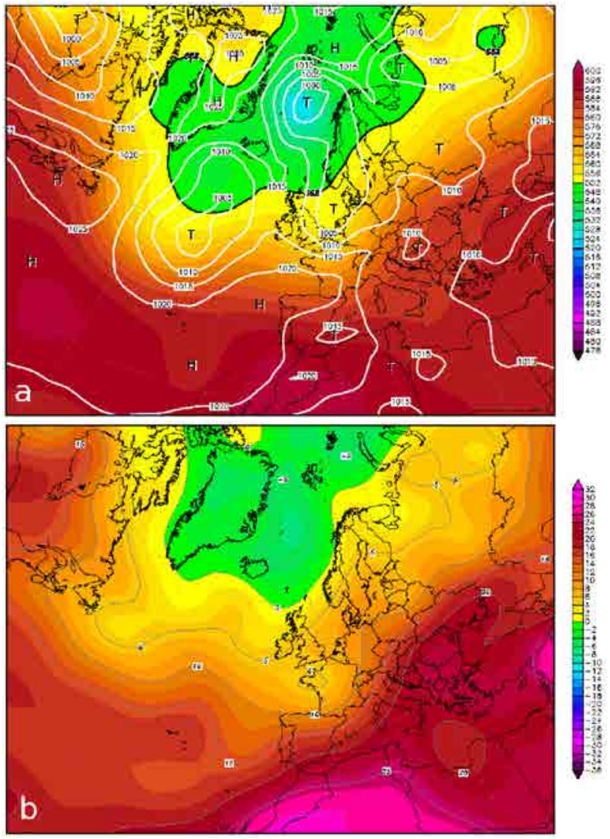

Figure A.4: NCEP Reanalysis of (a) geopotential height in decameters at 500 hPa (color contours) and sea level pressure (white isolines) and (b) the temperature field (color contours) at 850 hPa on 26 August 2012 at 00:00 UTC.

A.1.3 WRF simulation

Two nested domains having 3 and 1 km of horizontal resolution were defined with 400×400 and 451×451 points, respectively (see Fig. A.2). The physical parameterizations used are MRF (Hong and Pan, 1996) scheme for the PBL, RRTM scheme for longwave radiation (Mlawer et al., 1997); MM5 shortwave scheme for shortwave radiation (Dudhia, 1989); and WSM 6–class scheme (Hong and Lim, 2006) for the microphysics parameterization. No cumulus parameterization is used for any of the domains. The initial and boundary conditions were updated every six hours with information obtained from the analysis of the ECMWF model, at 0.125° of horizontal resolution. The simulation begins on 24 August 2012 at 00:00 UTC and runs during 72 hours, and two–way method is employed.

Figure A.5 shows the surface wind field (arrows) and the liquid water mixing–ratio (color contours) at 700 m in domain 1 at (a) 08:00, (b) 10:00, (c) 20:00 UTC on 25 and (d) 08:00 UTC on 26 August 2012. Below 700 m no clouds are simulated. According to the simulations, at 08:00 UTC on 25 August 2012 (Fig. A.5a) southerlies prevailed over the Gulf of Lion. Simulated clouds are related with the orography but not caused by a cold front. A small vortex is simulated approximately at the middle of the gulf of Lion, as recorded by Meteosat (see Fig. A.3a). A northwesterly outbreak starts on the west part of the Gulf, while southeasterly flow prevails in the easter part. At 10:00 UTC (Fig. A.5b) a small cloud arc associated to this northwesterly flow is simulated at approximately the same location as observed by the Meteosat satellite (see Fig. A.3a). This cloud arc expands out to the south of the WMB driven by the northwesterly flow. A well–defined cloud arc is simulated at 20:00 UTC on 25 August 2012 at 700 m (Fig. A.5c). The strong northwesterly Mistral flow (17.5 m s^{-1}) over the coast in the Gulf of Lion deflects to a northerly flow at the center of the WMB and to northeasterly at the western part of the WMB. The cloud–arc associated reaches around 1200 km length. At 08:00 UTC on 26 August 2012 (Fig. A.5d), the cloud arc is located between the island of Sardinia and the Southeast of the Iberian Peninsula, near to the north coast of Africa, at approximately the same location as observed by the Meteosat satellite (see Fig. A.3b). From this moment the simulated cloud arc starts to disappear.

Figure A.6 shows the vertical cross section along the lines (a) A1–A2 and (b) B1–B2 indicated in Fig. A.2 of the simulated potential temperature (color contours), wind field (arrows) and the liquid water mixing–ratio (black contours) at 20:00 UTC on 25 August 2012. The depth of the cold air mass is around 700–1000 m in both Figs. A.6. Approximately over the head of this cold front clouds are formed. Clouds extend vertically from around 700 m up to 1500 m. No precipitation is simulated by WRF.

A.2 Costal fronts at the mesoscale in the WMB

In order to classify and determine the scale of these three events, CF9, CF10 and the CF presented in this Appendix, Table A.1 summarizes the values obtained from the WRF simulation of the horizontal (L), vertical (H) and temporal (T) scales. The cold front depth (H) is estimated from a vertical cross section of the potential temperature along the red, blue and green lines defined in Fig. A.2. Furthermore, the ratio H/L, defined by Markowski

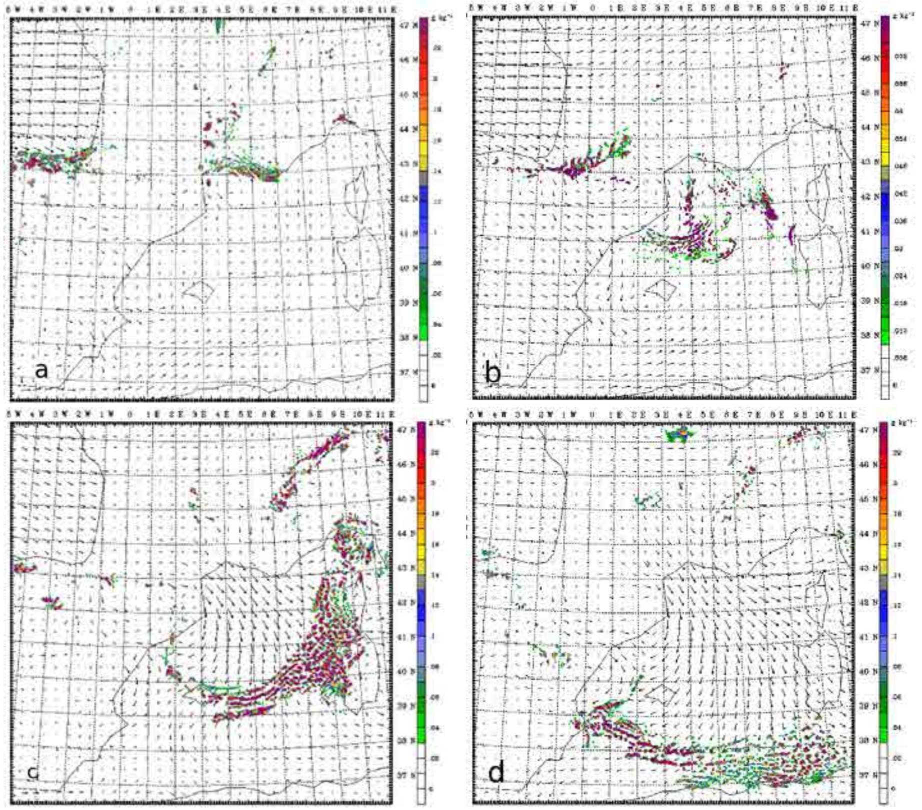

Figure A.5: Simulated liquid water mixing–ratio at 700 m (color contours) and surface wind field (arrows) at (a) 08:00 UTC, (b) 10:00 UTC, (c) 20:00 UTC on 25 August 2012 and (d) at 08:00 UTC on 26 August 2012. The maximum horizontal wind speed is 12.7 m s^{-1}, 17.5 m s^{-1} and 16.9 m s^{-1} in (b), (c) and (d) respectively.

and Richardson (2010), is also determined.

Table A.1: Characteristics of horizontal (L), vertical (H) and temporal (T) scales, and the ratio H/L (Markowski and Richardson, 2010) obtained from the WRF simulation in each event.

Event	L (km)	H (km)	H/L	T (h)	Scale
25 August 2012	2000	0.7–1	10^{-4}	24–30	meso–α
6 September 2011(FC9)	200	0.6	10^{-3}	10–12	meso–β
13 October 2010 (CF10)	20	0.2–0.5	10^{-2}	3	meso–γ

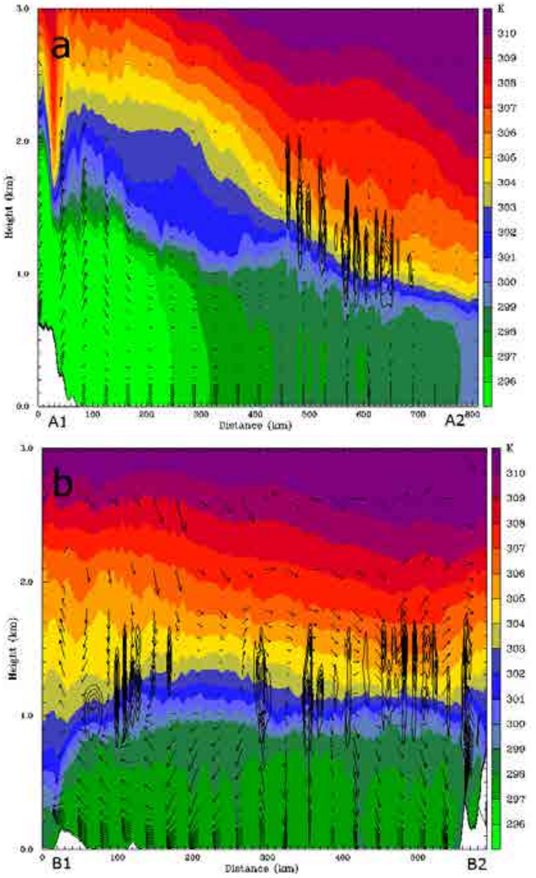

Figure A.6: Vertical cross section of the simulated potential temperature (color contours), liquid water mixing–ratio (black contours, maximum value 0.18 g kg^{-1}) and wind field (arrows) along the lines (a) A1–A2 and (b) B1–B2 indicated in Fig. A.2 at 20:00 UTC on 25 August 2012. The maximum horizontal wind speed is 19.6 m s^{-1}, and the maximum vertical wind vector is 25.6 cm s^{-1}.

Taking into account the values of L, H and T and the criteria defined in Orlanski (1975), the three selected events are within the three sub–mesoscales. Figure A.7a shows each event classified in a T and L diagram. The cloud arc event on 25 August 2012 is within the meso–α scale; the line of precipitation associated to CF9 occurred on 6 September 2011 is within the meso–β; the precipitation cells associated to CF10 occurred on 11 October 2010 is within the meso–γ. Additionally, following Markowski and Richardson (2010), Fig. A.7b shows the relation between H and L of a meteorological event, and in colored dots the position of the three simulated events. The hydrostatic regime occurs when the ratio H is much small than L. As expected, the three studied cases present an hydrostatic regime because $H/L \ll 1$.

Observations and simulations suggest that the WMB can be considered as a frontogenesis

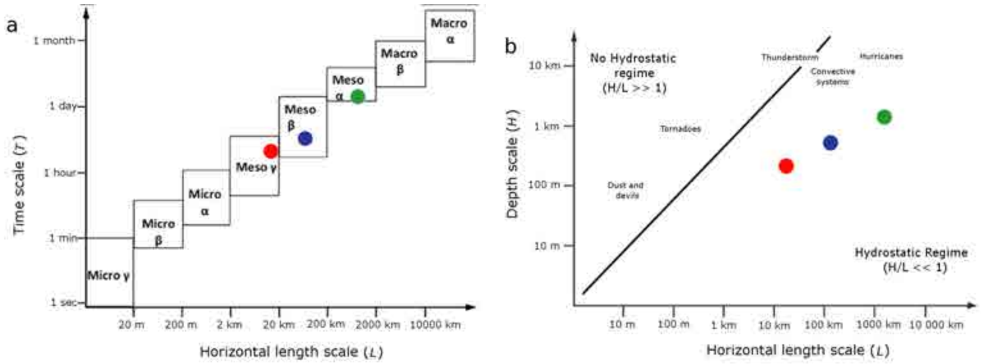

Figure A.7: (a) Temporal scale (T) as a function of the horizontal scale (L) (Orlanski, 1975). The colored dots indicate the position within these scales of the simulated coastal–fronts formed over the WMB on 25 August 2012 (green), CF9 on 6 September 2011 (blue) and CF10 on 13 October 2010 (red). In (b), horizontal scale (L) as a function of the vertical scale (H) (Markowski and Richardson, 2010).

region in which cold fronts are formed at the mesoscale, associated to outbreaks of cold air over the relatively warm sea–air. The complex topography around the WMB plays an important role in two aspects. First, by channelizing Mistral flows and promoting drainage winds following valleys and the slope of some mountains located close the coast. Second, by enclosing the basin and as a consequence making the WMB the source region of the maritime Mediterranean air, a relatively warm and wet air mass.

Despite that Mistral outbreaks are well–known and well–studied, as well as the dynamics of the large–scale fronts over the WMB, frontogenesis over this area has not been studied in detail. Taking into account the nocturnal coastal fronts observed and simulated within the WMB, as well as the cold outbreak though the gulf of Lion, it can be proposed the WMB as a frontogenesis area in the whole mesoscale.

Bibliography

Acker, J. G. and G. Leptoukh, 2007: Online analysis enhances use of NASA earth science data. *EOS Trans.*, **88**, 14–17.

Alpert, P., B. U. Neuman, and Y. Shay-El, 1990: Climatological analysis of Mediterranean cyclones using ecmwf data. *Tellus A*, **42**, 65–77.

Benjamin, T. B., 1968: Gravity currents and related phenomena. *J. Fluid Mech.*, **31**, 209–248.

Bohren, C. F. and B. A. Albrecht, 1998: *Atmospheric Thermodynamics*. Oxford University Press, New York, (402 pp.).

Bukovsky, M. and D. Karoly, 2009: Precipitation simulations using WRF as a nested regional climate model. *J. Appl. Meteorol. Clim.*, **48**, 2152–2159.

Buzzi, A. and S. Tibaldi, 1978: Cyclogenesis in the lee of the Alps: A case study. *Q. J. Roy. Meteor. Soc.*, **104**, 271–287.

Callado, A. and R. Pascual, 2002: Storms in front of the mouth rivers in north-eastern coast of Iberian peninsula. *Proceedings, 4th Plinius Conference on Mediterranean Storms*, Mallorca (Spain), URL `http://www.uib.es/depart/dfs/meteorologia/METEOROLOGIA/ROMU/informal/proceedings_4th_plinius_02/PDFs/Callado_and_Pascual.pdf`.

Camberlin, P. and O. Planchon, 1997: Coastal precipitation regimes in Kenya. *Phys. Geogr.*, **79**, 109–119.

Campins, J., A. Genovès, A. Jansà, J. A. Guijarro, and C. Ramis, 2000: A catalogue and a classification of surface cyclones for the western Mediterranean. *Int. J. Climatol.*, **20**, 969–984.

Clarke, R., 1961: Mesostructure of dry cold fronts over featureless terrain. *J. Meteorol.*, **18**, 715.

Davolio, S., A. Buzzi, and P. Malguzzi, 2006: Orographic influence on deep convection: case study and sensitivity experiments. *Meteor. Z.*, **15**, 215–223.

Drobinski, P., V. Ducrocq, P. Alpert, and co authors, 2013: HyMeX, a 10-year multidisciplinary program on the Mediterranean water cycle. *B. Am. Meteorol. Soc.*, doi: 10.1175/10.1175/BAMS-D-12-00242.1.

Ducrocq, V., I. Braud, S. Davolio, and co authors, 2013: HyMeX-SOP1, the field campaign dedicated to heavy precipitation and flash flooding in the northwestern Mediterranean. *B. Am. Meteorol. Soc.*, doi:10.1175/BAMS-D-12-00244.1.

Dudhia, J., 1989: Numerical study of convection observed during the winter monsoon experiment using a mesoscale two–dimensional model. *J. Atmos. Sci.*, **46**, 3077–3107.

Dudhia, J., 1993: A nonhydrostatic version of the Penn–State–NCAR mesoscale model: Validation test and simulation of an Atlantic cyclone and cold front. *Mon. Weather Rev.*, **121**, 1493–1513.

Durran, D. R. and J. B. Klemp, 1987: Another look at down–slope winds. Part II: nonlinear amplification beneath wave–overturning layers. *J. Atmos. Sci.*, **44**, 3402–3412.

Flamant, C., 2003: Alpine lee cyclogenesis influence on air–sea heat exchanges and marine atmospheric boundary layer thermodynamics over the western Mediterranean during a Tramontane/Mistral event. *J. Geophys. Res.*, **108 C2**, 5–24, doi:10.1029/2001JC001040.

Frye, J. L. and Y. L. Chen, 2001: Evolution of downslope flow under strong opposing trade winds and frequent trade-wind rainshowers over the island of Hawaii. *Mon. Weather Rev.*, **129**, 956–977.

Glickman, T., 2000: *Glossary of Meteorology.* American Meteorology Society (2on ed.), Boston (USA).

Goldreich, Y., H. Mozes, and D. Rosenfeld, 2004: Radar analysis of cloud system and their rainfall yield in Israel. *Israel J. Earth Sci.*, **53**, 63–76.

Grell, G., J. Dudhia, and D. Stauffer, 1995: A description of the fifth–generation Penn State/NCAR Mesoscale Model (MM5). Tech. Rep. NCAR/TN–398+STR, NCAR Tech.

Haddad, Z. S., E. A. Smith, C. D. Kummerow, T. Iguchi, M. R. Farrar, S. L. Durnen, M. Alves, and W. S. Olson, 1997: The TRMM 'day–1' radar/radiometer combined rain profiling algorithm. *J. Meteorol. Soc. Jpn.*, **75**, 799–809, URL `http://hdl.handle.net/2014/22850`.

Heiblum, R. H., I. Koren, and O. Altaratz, 2011: Coastal precipitation formation and discharge based on TRMM observations. *Atmos. Chem. Phys.*, **11**, 13 201–13 217.

Hernández-Ceballos, M. A., J. A. Adame, J. P. Bolívar, and B. A. de la Morena, 2013: A mesoscale simulation of coastal circulation in the Guadalquivir valley (southwestern Iberian Peninsula) using the WRF–ARW model. *Atmos. Res.*, **124**, 1–20.

Hong, S.-H., J. Dudhia, and S.-H. Chen, 2004: A revised approach to ice microphysical processes for the bulk parameterization of clouds and precipitation. *Mon. Weather Rev.*, **132**, 103–120.

Hong, S.-H. and J.-W. Lee, 2009: Assesment of the WRF model in reproducing a flash–flood heavy rainfall event over Korea. *Atmos. Res.*, **93**, 818–831.

Hong, S.-Y. and J. O. J. Lim, 2006: The WRF single–moment 6–class microphysical scheme (WSM6). *J. Korean Meteorol. Soc.*, **42(2)**, 129–151.

Hong, S.-Y. and H.-L. Pan, 1996: Nonlocal boundary layer vertical diffusion in a medium-range forecast model. *Mon. Weather Rev.*, **124**, 2322–2339.

Houze, R. A., S. G. Geostis, F. D. Marks, and A. K. West, 1981: Winter monsoon convection in the vicinity of north Borneo. Part I: structure and time variation of the clouds and precipitation. *Mon. Weather Rev.*, **109**, 1595–1614.

Huffman, G. J., R. F. Adler, S. Curtis, D. Bolvin, and E. J. Nelkin, 2007a: *Global rainfall analyses at monthly and 3-hr time scales*, chap. Measuring precipitation from Space: EURAINSAT and the Future, 291–306. Kluwer Academic Pub. B.V., Dordrecht (The Netherlands).

Huffman, G. J., et al., 2007b: The TRMM multi-satellite precipitation analysis: Quasi–global, multi–year, combined–sensor precipitation estimates at fine scale. *J. Hydrometeor.*, **8**, 38–55.

Jansà, A., 1987: Distribution of the mistral: a satellite observation. *Meteorol. Atmos. Phys.*, **36**, 201–214.

Jansà, J. M., 1959: La masa de aire mediterraneo. *Rev. Geofísica*, **18**, 35–50.

Jiang, Q., R. B. Smith, and J. Doyle, 2003: The nature of the mistral: Observations and modelling of two map events. *Q.J.R. Meteorol. Soc.*, **129**, 857–875.

Kármán, V. T., 1940: The engineer grapples with nonlinear problems. *B. Am. Math. Soc.*, **46**, 615.

Keulegan, G., 1958: The motion of saline fronts in still water. *Nat. Bur. Stand. Rept.*, –, 5831.

Khain, A. P., D. Rosenfeld, and I. L. Sednev, 1993: Coastal effects in the Eastern Mediterranean as seen from experiments using a cloud ensemble model with a detailed description of warm and ice microphysical processes. *Atmos. Res.*, **30**, 295–319.

Kousky, R. and E. Vemon, 1980: Diurnal rainfall variations in northeast Brazil. *Mon. Weather Rev.*, **108**, 488–498.

LaCasse, K. M., M. E. Splitt, S. M. Lazarus, and W. M. Lapenta, 2008: The impact of high–resolution sea surface temperatures on the simulated nocturnal Florida marine boundary layer. *Mon. Weather Rev.*, **136**, 1349–1372.

Lau, J. and C. Yi-Leng, 1999: A case study of nocturnal rain showers over windward coastal region of the island of Hawaii. *Mon. Weather Rev.*, **127**, 2674–2692.

Lin, Y.-L., S. Chiao, T.-A. Wang, M. Kaplan, and R. Weglarz, 2001: Some common ingredients for heavy orographic rainfall. *Weather Forecast.*, **16**, 633–660.

Malda, D., J. Vilà-Guerau de Arellano, W. D. Van der Berg, and I. W. Zuurendonk, 2007: The role of atmospheric boundary layer-surface interactions on the development of coastal fronts. *Ann. Geophys.*, **25**, 341–360.

Mapes, B., T. Warner, M. Xu, and A. Negri, 2003a: Diurnal patterns of rainfall in northwestern South America. Part I: Observations and context. *Mon. Weather Rev.*, **131**, 799–812.

Mapes, B., T. Warner, M. Xu, and A. Negri, 2003b: Diurnal patterns of rainfall in northwestern South America. Part III: Diurnal gravity waves and nocturnal convection offshore. *Mon. Weather Rev.*, **131**, 830–884.

Markowski, P. and Y. Richardson, 2010: *Mesoscale Meteorology in Midlatitudes.* Wiley, Chichester (UK).

McGinley, J., 1982: A diagnosis of Alpine lee cyclogenesis. *Mon. Weather Rev.*, **110**, 1271–1287.

Meyer, J. H., 1971: Radar observations of land breeze fronts. *J. Appl. Meteorol.*, **10**, 1224–1232.

Michelson, S. and J.-W. Bao, 2008: Sensitivity of low–level winds simulated by the WRF model in California's central valley to uncertainties in the large–scale forcing and soil initialization. *J. Appl. Meteorol. Clim.*, **47**, 3131–3149.

Miglietta, M. and A. Buzzi, 2001: A numerical study of moist stratified flows over isolated topography. *Tellus*, **53A**, 481–499.

Miglietta, M., S. Laviola, A. Malvaldi, D. Conte, V. Levizzani, and C. Price, 2013: Analysis of tropical–like cyclones over the Mediterranean sea though a combined modeling and satellite approach. *Geophys. Res. Lett.*, **40**, 2400–2405.

Miglietta, M. and R. Rotunno, 2010: Numerical simulations of low–CAPE flows over a mountain ridge. *J. Atmos. Sci.*, **67**, 2391–2401.

Millot, C., 1979: Wind induced upwellings in the Gulf of Lions. *Oceanol. Acta*, **2**, 261–274.

Mlawer, E. J., S.-J. Taubman, P.-D. Brown, M. J. Iacono, and S. A. Clough, 1997: Radiative transfer for inhomogeneous atmospheres: RRTM, a validated correlated–k model for the longwave. *J. Geophys. Res.*, **102**, 663–682.

Mori, S., J. I. Hamada, M. D. Yamanaka, N. Okamoto, F. Murata, N. Sakurai, H. Hashiguchi, and T. Sribimawati, 2004: Diurnal land–sea rainfall peak and migration over Sumatra island, Indonesian maritime continent observed by TRMM satellite and intensive rawinsonde soundings. *Mon. Weather Rev.*, **132**, 2021–2039.

Moscatello, A., M. Miglietta, and R. Rotunno, 2008: Numerical analysis of a Mediterranean (hurricane) over Southeastern Italy. *Mon. Weather Rev.*, **136**, 4373–4397.

Murakami, M., 1983: Analysis of the deep convective activity over the western Pacific and southeast Asia. *J. Meteorol. Soc. Jpn.*, **61**, 60–75.

Neumann, J., 1951: Land breezes and nocturnal thunderstorms. *J. Meteorol.*, **8**, 60–67.

Ohsawa, T., H. Ueda, T. Hayashi, A. Watanabe, and J. Masumoto, 2003: Diurnal variations of convective activity and rainfall in tropical Asia. *J. Meteorol. Soc. Jpn.*, **79**, 333–352.

Orlanski, I., 1975: A rational subdivision of scales for atmospheric processes. *B. Am. Meteorol. Soc.*, **56**, 527–530.

Pérez, C., M. Sicard, O. Jorba, A. Comerón, and J. M. Baldasano, 2004: Summertime re–circulations of air pollutants over the north–eastern Iberian coast observed from systematic EARLINET lidar measurements in Barcelona. *Atmos. Environ.*, **38**, 3983–4000.

Prandtl, L., 1952: *Essentials of Fluids Dynamics.* Hafner, New York (USA).

Radinovic, D., 1986: On the development of orographic cyclones. *Q. J. Roy. Meteor. Soc.*, **112**, 927–951.

Reale, O. and R. Atlas, 2001: Tropical cyclone–like vortices in the extratropics: Observational evidence and synoptic analysis. *Weather Forecast.*, **16**, 7–34.

Reeves, H. and R. Rotunno, 2008: Orographic flow response to variations in upstream humidity. *J. Atmos. Sci.*, **66**, 3557–3570.

Rixen, M., et al., 2005: The Western Mediterranean deep water: A proxy for climate change. *Geophys. Res. Lett.*, **32**, doi:10.1029/2005GL022702.

Rotunno, R. and R. Ferretti, 2001: Mechanism of intense alpine rainfall. *J. Atmos. Sci.*, **58**, 1732–1749.

Salat, J. and J. Pascual, 2002: The oceanographic and meteorological station at l'Estartit (NW Mediterranean). *Tracking long-term hydrographical change in the Mediterranean sea. CIESM Workshop Ser.*, CIESM, 29–32, URL `http://www.ciesm.org/online/monographs/Monaco.pdf`.

Salat, J. and J. Pascual, 2006: Principales tendencias climatológicas en el Mediterráneo Noroccidental, a partir de más de 30 años de observaciones oceanográficas en la costa catalana. *Clima, Sociedad y Medio Ambiente*, Asociación Española de Climatología, Vol. Serie A, No. 5., 284–290, URL `{http://www.aeclim.org/images/stories/articulos_pdf/Vcongreso/ponencia_cambio_climatico/salat.pdf}`.

Sarrand, B., et al., 2012: Precipitation in the Mediterranean basin as seen from the 2000-2010 TRMM-3B42-v6 database. *EGU General Assembly*, Vienna (Austria), URL `http://presentations.copernicus.org/EGU2012-11965_presentation.pdf`.

Schoenberg, L., 1984a: Doppler observation of land–breeze cold front. *Mon. Weather Rev.*, **112**, 2455–2464.

Schoenberg, L. M., 1984b: Doppler radar observation of land–breeze cold front. *Geophys. Res. Lett.*, **112**, 2455–2464.

Segele, Z., L. Leslie, and P. Lamb, 2008: Weather Research and Forecasting model simulations of extended warm–season heavy precipitation episode over the US southern Great Plains: Data assimilation and microphysics sensitivity experiments. *Tellus A*, **65**, 3131–3149.

Simpson, J. E. and R. E. Britter, 1980: A laboratory model of atmospheric mesofront. *Q. J. Roy. Meteor. Soc.*, **106**, 485–500.

Skamarock, W. C., et al., 2008: A Description of the Advanced Research WRF Version 3. Tech. Rep. TN–475+STR, NCAR.

Somot, S., F. Sevault, M. Déqué, and M. Crépon, 2008: 21st century climate change scenario for the Mediterranean using a coupled atmosphere–ocean regional climate model. *Global Planet. Change*, **63**, 112–126.

Storm, B., J. Dudhia, S. Basu, A. Swift, and I. Giammanco, 2008: Evaluation of the Weather Research and Forecasting model on forecasting low–level jets: implications for wind energy. *Wind Energy*, **12**, 81–90.

Trenberth, K. E., et al., 2007: *Climate Change 2007: The Physical Science Basis. Contribution of Working Group I to the Fourth Assessment Report of the Intergovernmental Panel on Climate Change*, chap. 3. Observations: surface and atmospheric climate change. Cambridge University Press, Cambridge (United Kingdom), [Solomon, S., D. Qin, M. Manning, Z. Chen, M. Marquis, K.B. Averyt, M. Tignor and H.L. Miller (eds.)].

Trigo, I. F., T. D. Davis, and G. R. Bigg, 1999: Objective climatology of cyclones in the Mediterranean region. *J. Geophys. Res.*, **12**, 1685–1696.

Ulbrich, U., G. C. Leckebusch, and J. G. Pinto, 2009: Extra–tropical cyclones in the present and future climate: a review. *Theor. Appl. Climatol.*, **54**, 139–146.

Vargas-Yáñez, M., M. J. García, J. Salat, M. C. García-Martínez, J. Pascual, and F. Moya, 2008: Warming trends and decadal variability in the Western Mediterranean shelf. *Global Planet. Change*, **63**, 177–184, doi:10.1016/j.gloplacha.2007.09.001.

Wakimoto, R. M. and N. T. Atkins, 1994: Observations of the sea–breeze front during CAPE. Part I: single–Doppler, satellite, and cloud photogrammetry analysis. *Mon. Weather Rev.*, **122**, 1092–1114.

Wang, J. J., R. Rauber, H. T. I. Ochs, and R. E. Carbone, 2000: The effects of the island of Hawaii on offshore rainband evolution. *Mon. Weather Rev.*, **128**, 1052–1069.

Wapler, K. and T. P. Lane, 2012: A case of offshore convective initiation by interacting land breezes near Darwin, Australia. *Meteorol. Atmos. Phys.*, **5**, 123–137.

Warner, T., B. Mapes, M. Xu, and A. Negri, 2003: Diurnal patterns of rainfall in northwestern South America. Part II: model simulations. *Mon. Weather Rev.*, **131**, 813–829.

Williams, E., 1994: Global circuit response to seasonal variations in global surface air temperature. *Mon. Weather Rev.*, **117**, 1917–1929.

Wu, P., M. Yamanaka, and J. Matsumoto, 2008: The formation of nocturnal rainfall offshore from convection over western Kalimantan (Borneo) island. *J. Meteorol. Soc. Jpn.*, **86A**, 187–203.

Yang, G. Y. and J. M. Slingo, 2001: The diurnal cycle in the tropics. *Mon. Weather Rev.*, **129**, 784–801.

Ye, B., A. Del Genio, and K. K.-W. Lo, 1998: CAPE variations in the current climate and in a climate change. *J. Climate*, **11**, 2985–3002.

Yu, C. K. and B. J. Jou, 2004: Radar observations of the diurnal forced offshore convection lines among the southeastern coast of Taiwan. *Mon. Weather Rev.*, **133**, 1613–1636.

Zuidema, P., 2003: Convective clouds over the Bay of Bengal. *Mon. Weather. Rev.*, **131**, 780–798.

Summary of the thesis

The main goal of this thesis is to investigate the formation of nocturnal coastal fronts in the Mediterranean basin responsible for the nocturnal offshore precipitation near the coastline. The hypothesis to explain the formation of these coastal fronts is as follows. After sunset the cooled inland air moves to the coastline, drive by drainage winds as a density current, which form a coastal front when reach the sea. Then the warm and wet sea–air is lifted by the cold drained air as it moves offshore. When ascending it may form clouds if it reaches the lifting condensation level (LCL), and convective clouds that may cause precipitation if it reaches the level of free convection (LFC).

The influence in the coastal front formation of the land–sea thermal difference, the shape of the coastline, the sea surface temperature (SST) and the depth of the cold air mass associated to the coastal front is investigated in this Thesis.

The methodology used consists in three steps. The first one is to search events of nocturnal precipitation associated to the coastal fronts. Tropical Rain Measurement Mission (TRMM) Satellite, reflectivity radar network images, and satellite images are used. Those events detected during nighttime, presenting precipitation areas offshore but near the coastline, lasting no more than 6 consecutive hours, slightly moving offshore and with extension is lower than 500 km have been considered as possible coastal front events. The second step consists in analyzing the synoptic situation associated to these possible coastal–front events, in order to discard those in which the precipitation is related to synoptic features such as convection associated to dynamic low–pressure areas, large–scale warm or cold fronts, or to a trough affecting the region in where precipitation is detected. Finally, the WRF–ARW model is used for the simulation of these possible coastal–front events. Ten coastal–fronts are analyzed in this Thesis.

Chapter 2 is devoted to study the role of the land–sea air temperature difference. Three coastal fronts characterized by a relatively large sea–land thermal difference are simulated and analyzed in this chapter: the coastal fronts occurred on the night on 6 January 2011 in front of the Israel coastline (CF5), on 3 March 2011 on the South of the Iberian Peninsula (CF8), and on 13 October 2010 in the northeast of the Iberian Peninsula (CF10), characterized by around 8, 9 and 6 K of simulated sea–land air thermal difference. Due to this relatively large thermal gradient, the simulations show that drainage winds reach velocities comparable to the prevailing wind, around 7 m s^{-1} in CF5 and CF8. A line of convergence is simulated offshore in CF5 and CF8, and around several precipitation cells occur forming a quasi–stationary line of precipitation. Relatively strong vertical motions are simulated

at these coastal fronts, specially CF5 and CF8, providing upward moisture and heat that produce convective clouds and precipitation.

Chapter 3 focusses on the shape of the coastline. Concave coastlines favor the offshore convergence of nocturnal flows, while convex coastlines favor convergence onshore of sea breeze. Focussing on nocturnal breezes, high rainfall rates offshore during the night hours have been observed and analyzed in concave coastal areas. In the Mediterranean basin, two CFs are analyzed: the coastal front occurred over the gulf of Sidra (Libya), in the middlesouth of the Mediterranean basin on 30 January 2008 (CF6), and the coastal front occurred in the gulf of Genoa, in the northwest Mediterranean basin on 30 January 2008 (CF1). In both events, drainage winds drive cold inland air offshore from many areas along the concave coastline. The cold inland air collides offshore with the opposite inland cold drained air from the oppoaite coastline areas, converging offshore. As a result, over the line of convergence heat and moisture move upwards from the sea, at velocities that reach 1.2 m s^{-1} and 0.9 m s^{-1} in CF6 and CF1, respectively. Clouds and precipitation are simulated following the concave coastline.

In Chapter 4, the influence of the SST on the coastal fronts is analyzed. The SST is the main source providing moisture and heat to the air. A couple of CFs occurred at the end of the summer and early autumn, when the SST presents the larger values, are analyzed. These fronts are CF9, occurred at the western Mediterranean basin during the night on 6 September 2011, and the CF2, occurred on the middle of the Mediterranean basin on 28 September 2008. The simulation of the CF9 shows the heaviest rainband within the 10 coastal front, associated to the largest value of the SST. Moreover, CF2 is one of the several coastal fronts formed around the Italian Peninsula associated to a large SST.

The second analysis consist in performing numerical experiments with the WRF–ARW model to investigate the sensibility of two relatively heavy nocturnal offshore rainbands to the SST: the CF5 (occurred in the eastern Mediterranean basin) and the CF9 (in the western part of the basin). In these numerical experiments SST is increased by 2.2 and 2.5 K (SSTR simulation) for each season at the end of the 21st century in the east (CF5) and west (CF9) Mediterranean basin, respectively, and compared with the control run (CR), where SST is not modified. In the SSTR the precipitation field shifted offshore when comparing with the CR simulations. Additionally, wider precipitation areas, with higher amount of accumulated precipitation, are simulated within the rainbands in SSTR. Concerning to the wind, SSTR show that drainage wind speed increases close to the coastline. In SSTR cases, the warmer sea–air induced by higher SST enhances the speed of the drainage winds, which is consistent with the fact that the rainband is simulated further offshore than in the CR. Simulated values of CAPE over the coastal front head are also increased for SSTR. The modification of some of the parameters defined in Chapter 4, such as he triggering, the blockage and the deceleration that the cold air offers to the prevailing maritime sea–air has been also analyzed.

The role of the coastal–front depth (H) is analyzed in chapter 5. In this chapter H of the ten detected and simulated coastal fronts has been evaluated by using two methodologies. The first methodology is based in evaluating H by plotting the vertical cross section of the simulated potential temperature. The second methodology uses the equation proposed by Simpson and Britter (1980) for the ten simulated coastal fronts. Both methods show quite similar results. By analyzing the time evolution of H for each CF, the maximum depth of the cold air mass, which occur for all the cases during the early morning, is related to the module of the relative wind speed between the cold and the warm air masses at the coastal front head, and to the 2–m potential temperature difference between the two air masses. Additionally, it is assumed that cold air mass acts as a moving orographic barrier to the warmer prevailing flow. For this reason some parameters proposed by Miglietta and Rotunno (2010), Wang et al. (2000) and Durran and Klemp (1987) in their idealized studies have been adapted in order to analyze the dynamic of the events: the blockage parameter, the triggering convection parameter, and the deceleration parameter, which parameters are estimated hourly and averaged over the nighttime. From the averaged values of sea–air and land–air temperatures, a cloud band forecasting index is proposed by using the classical Espys equation and the relationship found between the average coastal–front depth and the sea–land thermal difference for the ten simulated coastal–fronts.

The scale in which the coastal fronts develop in the Mediterranean basin is studied in Appendix A. The meso–β and meso–γ are the scales in which the studied coastal fronts presented in the previous chapters developed in the whole Mediterranean basin. Focusing in the West Mediterranean basin, the coastal front at the meso–α scale formed from a cold outbreak over the Gulf of Lion on 25–26 August 2012 is simulated and described in Appendix A. Here we propose that the western Mediterranean basin can be considered as a frontogenesis region in which fronts occur at the whole mesoscale. Meso–β and meso–γ scales, fronts are formed during the night caused by the inland drainage air drive by drainage winds, while at meso–α scale fronts formed by synoptic cold outbreaks from the gulf of Lion.

Agraïments / acknowledgements

El punt de partida

Mai hagués imaginat que quan l'any 2005 se'm va encarregar per part de la direcció del Parc Natural del Garraf un estudi que caracteritzés el clima d'aquest massís, un dels resultats més destacables d'aquell estudi seria el punt de partida d'aquesta tesi. El fet que dins d'aquest sistema muntanyós no es disposés d'estacions meteorològiques a partir de les quals pogués fer un estudi quantitatiu de les principals variables meteorològiques, em va obligar a enfocar l'estudi analitzant les dades meteorològiques d'observatoris que envolten aquest massís, per així veure si el massís tenia alguna influència remarcable en la modificació d'aquestes. Entre aquestes variables, la precipitació era la que mostrava una gran heteorogeneïtat al voltant del massís, essent sobre el Delta del Llobregat (al nord–nordest del massís molt superior que en la resta de zones perifèques al massís. La causa d'aquest modificació, en aquell moment, em va ser desconeguda. El màxim de precipitació al Delta del Llobregat respecte zones properes que envolten el massís del Garraf em va cridar l'atenció des del primer moment; de tant en tant recodava algun comentari del meu avi patern segons del qual algun cop havia sentit dir-li que a la tardor hi plou sovint de nit en aquesta zona. La informació que em faltava per poder relacionar la visió subjectiva sobre la pluja nocturna durant la tardor i el màxim de precipitació sobre el delta em va venir en una conversa informal amb el meteoròleg i amic Ramon Pascual, de l'Agència Estatal de Meteorologia (AEMET). En aquells dies del 2006, en Ramon investigava les causes de l'inici de la convecció a Catalunya, i un dels casos que considerava com a inici d'aquest procés era la interacció entre l'aire fred que drena a través de rius com el Llobregat o el Besòs, amb l'aire més càlid situat sobre el mar. Podia ser aquella l'explicació del màxim de precipitació al Delta del Llobregat?

A partir de les dades de precipitació horària de l'estació meteorològica automàtica que el Servei Meteorològic de Catalunya (METEOCAT) té ubicada al terme de Viladecans, a la zona agrícola del Delta del Llobregat, vaig analitzar les dades de precipitació horària des del 1993. Durant la tardor, sobretot al setembre i l'octubre un percentatge elevat de la precipitació es produïa en hores nocturnes. Per tant, la hipòtesi de la formació d'un front costaner superficial semblava confirmar-se. Amb aquest estudi vam guanyar el V Premi Castelldefels Àmbit Sostenible del 2007.

Calia ara, confirmar l'existència d'aquest front costaner nocturn, i caracteritzar-lo. El

Dr. David Pino, director d'aquesta tesi, fou qui em proposà utilitzar la simulació numèrica per poder analitzar aquest tipus de fenòmens. Utilitzant el model MM5, antecessor del model WRF usat en aquesta tesi, vam caracteritzar un parell de casos de fronts costaners al delta del Llobregat, confirmant-se així l'existència d'aquest fenomen com a precursor de la precipitació nocturna. Aquesta hipòtesi va ser reconeguda rebent el primer premi Local Eduard Fontserè de Meteorologia, sota el títol L'anomalia Pluviomètrica del Delta del Llobregat, l'any 2007.

Després d'un parell d'anys de pausa, a finals del 2010 sorgeix la possibilitat d'estendre la recerca sobre fronts costaners a la Mediterrània, realitzant una tesis doctoral sobre aquesta temàtica.... El resultat és el mostrat en aquestes págines.

Agraïments

En aquest camí iniciat amb l'estudi del clima del massís del Garraf fins a aquesta tesis, hi ha persones i institucions que han estat implicades d'una o altra forma, a les quals vull d'agraïr el seu suport, ajuda i contribució a que aquesta tesis hagi estat possible.

Primerament al Dr. David Pino, per la seva excellent direcció, la seva dedicació, la paciència i la comprensió mostrada en tota la tesi, i per tot allò que he après d'ell. Al Dr. Daniel Crespo, director del Departament de Física Aplicada pels seus consells i suggeriments sempre interessants; a la companya de despatx Dra. Cesca Ribas pel seu ajut amb els alguns dubtes de Matlab i LaTex, així com a la resta de companys de la secció del Departament de Física Aplicada de Castelldefels, i en especial al Dr. Pere Bruna, Dr. Jordi Gutièrrez, Dr. Francesc Sunyol, i Dra. Pilar Gil.

Als informatics del departament, en Jordi Lino i en Toni Castillo, sempre eficients en resoldre aquelles qüestions informàtiques que per mi segueixen sent un misteri. Especialment a l'Alfred Gil, qui sempre ha estat allà davant dels meus dubtes i problemes amb el model WRF instal·lat en les màquines del Consorci de Serveis Universitaris de Catalunya (CSUC).

La paciència no només ha estat una virtud del director d'aquesta tesis, sinó tambè de l'Ester, el Nil i el petit Biel, els quals mai han posat mala cara quan no he pogut estar per ells alguns cops, així com als meus pares, Vicens i Adela.

I would like to acknowledge several institutions for their contribution in this Thesis. The reanalysis charts used for describing the synoptic situation of some of the events shown in some chapters were obtained from the NCEP reanalysis charts, uploaded to the Wetterzentrale. The Meteosat images were downloaded from the www.sat24.com and from NERC Satellite Receiving Station, Dundee University, Scotland (http://www.sat.dundee.ac.uk/).

Concerning to the images and data from TRMM were acquired using the GES-DISC Interactive Online Visualization ANd aNalysis Infrastructure (Giovanni) as part of the NASA's Goddard Earth Sciences (GES) Data and Information Services Center (DISC).

I would like also to acknowledge Dr. Hannu Sävijärvi, from the University of Helsinki, and Dr. Timo Vihma, from the Finnish Meteorological Institute, for my stage in the Finnish

Meteorological Institute during May and June 2013. There we investigated the coastal fronts that develop in the coldest Baltic Sea and particularly over the Gulf of Finland, in order to compare with those developed in the warmer Mediterranean Sea.

Les simulacions numèriques han estat portades a terme amb els recursos del CSUC, sota els projectes MICINN CGL2009–08609, CGL2012–37416–C0403 i INTERREG EU FLUX-PYR EFA 34/08.

Les imatges de radar han estat obtingudes del METEOCAT, i de l'AEMET.

Finally, this Thesis is based in four papers published in journals included in the Journal Citation Report index. Many anonimous referees contributed with their comments and suggestions to improve the quality of the publications. I would like also to acknowledge their contribution.

Castelldefels, Febrer del 2015